University of Strathclyde

Department of Naval Architecture, Ocean and Marine Engineering

Numerical investigation of the performance of WEC integrated with vertical wall using CFD

Injun Yang

A thesis presented in fulfilment of the requirements for the degree of Doctor of Philosophy

2024

This thesis is the result of the author's original research. It has been composed by the author and has not been previously submitted for examination which has led to the award of a degree.

The copyright belongs to the author under the terms of the United Kingdom Copyright Acts as qualified by University of Strathclyde Regulation 3.50. Due acknowledgement must always be made of the use of any material contained in, or derived from, this thesis.

Signed: 하범인조 Date: 03.06.2024

Acknowledgements

It is not a fair I shall begin with God the Almighty: without His will I would have supported me throughout my Ph.D.

I would like to express my sincere gratitude to all those who have contributed to this thesis, directly or indirectly. Your support, guidance, and encouragement have been invaluable throughout this Ph.D. journey.

First and foremost, I extend my deepest appreciation to my supervisor Professor Atilla Incecik and Dr Tahsin Tezdogan, whose expertise and insight have shaped this work significantly. Your guidance has been instrumental in navigating through the complexities of this research, and I am truly grateful for your teaching.

I would also like to thank my colleagues and peers for their collaboration and constructive feedback. Your diverse perspectives have enriched the discussion and have helped refine the ideas presented in this work.

I am also grateful to my family for their unwavering love and encouragement throughout this endeavour. Your patience, understanding, and belief in me have provided the strength to persevere during challenging times.

Thank you,

Injun

Contents

Contents 1

List of Figures 4

List of Tables 9

Nomenclature 11

Abbreviations 13

Abstract 14

1 Introduction 15

1.1 Background 15

1.2 Operating principles of WECs 16

1.3 Research objectives and scope 19

1.3.1 Investigating the integration of a WEC with vertical walls 19

1.3.2 Assessing the influence of a latching control strategy 19

1.3.3 Understanding WEC performance by computational fluid dynamics (CFD) simulations 19

1.3.4 Addressing the limitations and defining the research scope 20

1.4 Thesis structure 20

2 Literature review 22

2.1 Integration of vertical wall with WEC 22

2.1.1 Overview 22

2.1.2 Previous research of integrating WEC and breakwaters 23

2.2 Implementation of numerical PTO model 24

2.3 Implementation of latching control for WEC 25

2.4 Evaluation criteria for WEC performance 26

2.5 Significance of integrating WEC with coastal structures 27

3 Methodology 29

3.1 Research Methodology 29

3.2 Numerical modelling 30

3.2.1 Target geometry 30

3.2.2 Governing equations 31

3.2.3 Computational domain and boundary conditions 33

3.2.4 Numerical PTO model 36

3.2.5 Implementation of Latching control 40

4 CFD simulation for WEC integrated with a vertical wall 43

4.1 Goal and scope 43

4.2 Numerical modelling 44

4.3 Stationary wave 45

4.4 Results 47

4.4.1 Verification and comparison with experimental data 47

4.4.2 Cases without vertical wall 51

4.4.3 Cases with vertical wall 54

4.5 Concluding Remarks 64

5 CFD simulation for WEC integrated with a vertical wall and latching control 65

5.1 Goal and scope 65

5.2 Results 66

5.2.1 Verification 66

5.2.2 Simulation without the vertical wall 68

5.2.3 Simulation with the vertical wall 74

5.2.4 Simulation without vertical wall and under latching control 77

5.2.5 Simulation with vertical wall and under latching control 80

5.3 Concluding remarks 83

6 Summary and Discussions 85

6.1 Recommendations for future research 86

Reference 88

List of Figures

Figure 1.1 Generic view of oscillating water columns (EMEC) 16

Figure 1.2 Generic view of point absorber type WEC (EMEC).....17

Figure 1.3 Generic view of attenuator (EMEC).....17

Figure 1.4 generic view of overtopping devices (EMEC) 18

Figure 3.1 Schematic of the WEC (not at scale) including the centre of rotation (Point A) and the position of the hydraulic PTO cylinder (Point B and C).....31

Figure 3.2 Present computational domain and boundary conditions for a simulation case without the vertical wall.....34

Figure 3.3 Cells around the free surface and the distribution of cells along the z-direction. ..35

Figure 3.4 Distribution of forcing strength for wave forcing scheme in the computational domain for T=2.5s.....36

Figure 3.5 Distribution of forcing strength for wave forcing scheme in the simulation case with the vertical wall for T=1.6s.....36

Figure 3.6 Definition of variables for the numerical PTO model.....40

Figure 3.7 Operation of latching control in present numerical simulation. Latching instants when the velocity is zero: $t1$, $t3$ and $t5$; latching duration: TL; unlatching instants: $t2$ and $t4$.....41

Figure 3.8 Latching control strategy. Simulation time: $tsim$; transition time: $ttransition$; latched duration: TL; released instant: $treleased$.....42

Figure 4.1 Validity fields of wave theories according to Le Méhauté (2013). Red dots represent the wave conditions in this study.....44

Figure 4.2 The computational domain with imposed boundary conditions for numerical

simulation cases without a vertical wall (The units in the figure are metres).....45

Figure 4.3 Initialised computational domain before a numerical simulation starts. 45

Figure 4.4 The computational domain with imposed boundary conditions for vertical wall cases (The units on the figure are metres). 45

Figure 4.5 Schematic view of a buoy and a vertical wall. 46

Figure 4.6 Comparison of the displacement of the cylinder between the simulated and experimental data (Ransley et al., 2017), T=2.8s, H=0.25m. 50

Figure 4.7 Comparison of the displacement of the cylinder between numerical simulation and experimental data (Ransley et al., 2017), T=1.4s, H=0.15m. 51

Figure 4.8 Numerical results of FFT analysis of displacement of cylinder normalised by amplitude of the incident wave and comparison result with experimental data. 52

Figure 4.9 Numerical displacement of cylinder data for wave case 4 without the vertical wall. 52

Figure 4.10 Variation of the free surface around the buoy at 4 instants along a period, top view. (Wave case 4: T=2.0s, H=0.25m) 53

Figure 4.11 Variation of the free surface around the buoy at 4 instants along a period, side view. (Wave case 4: T=2.0s, H=0.25m) 53

Figure 4.12 Variation of the free surface near the buoy and on the wall of the buoy at 4 instants along a period, side view. (Wave case 4: T=2.0s, H=0.25m) 54

Figure 4.13 Numerical data and analytical solution for wave case 8 at three different wave probes. 55

Figure 4.14 Comparison between stationary wave amplitude and normalised spectral value of displacement of the cylinder according to distance to the vertical wall ($dwall$). 57

Figure 4.15 Variation of the free surface around the buoy with vertical wall, top view. And the

location of wave probes (Wave case 4: T=2.0s, H=0.25m and $dwall$= 3.0m).....58

Figure 4.16 Variation of the free surface around the buoy with vertical wall, side view. (Wave case 4: T=2.0s, H=0.25m and $dwall$= 3.0m) 58

Figure 4.17 Variation of the free surface near the buoy and on the wall of the buoy with vertical wall, side view. (Wave case 4: T=2.0s, H=0.25m and $dwall$= 3.0m) 59

Figure 4.18 Comparison of wave elevations for Wave case 4. Black solid line means the result of cases without the vertical wall, Red dashed line means the result of cases with vertical wall ($dwall$=2.0m) and Green dashed dot line represents the result of cases with vertical wall ($dwall$=3.0m). 60

Figure 4.19 Comparison of FFT results for Wave case 4 by wave probe. Black solid line means the result of cases without vertical wall, Red dashed line means the result of cases with vertical wall ($dwall$=2.0m) and Green dashed dot line represents the result of cases with vertical wall ($dwall$=3.0m). 61

Figure 4.20 Comparison of motion of WEC according to the presence of vertical wall. (a): Displacement of cylinder, (b): pitch. Black solid line means the result of cases without vertical wall, Red dashed line means the result of cases with vertical wall ($dwall$=2.0m) and Green dashed dot line represents the result of cases with vertical wall ($dwall$=3.0m).....62

Figure 4.21 Comparison of horizontal and vertical forces. (a): horizontal force, (b): vertical force. Black solid line means the result of cases without vertical wall, Red dashed line means the result of cases with vertical wall ($dwall$=2.0m) and green dashed dot line represents the result of cases with vertical wall ($dwall$=3.0m).....62

Figure 4.22 Pressure distribution of the WEC buoy for Wave case 4 (T=2.0s and H=0.25m). Case without vertical wall (the first column), case when $dwall$=2.0m (the second column) and case when $dwall$=3.0m (the third column). (a): zero-up crossing, (b): maximum lift, (c): zero-down crossing, (d): minimum lift. 63

Figure 5.1 Comparison of cylinder displacements ($BPTO = 50Nms$). 67

Figure 5.2 Comparison of cylinder displacements ($BPTO = 100Nms$). 67

Figure 5.3 Comparison of cylinder displacements ($BPTO = 200Nms$). 67

Figure 5.4 Displacement variation for increasing mesh refinement. 68

Figure 5.5 Results of numerical simulations without vertical wall for PTO data (displacement, PTO velocity and force) and absorbed power according to damping coefficient, wave case 2 (T=1.4s).....69

Figure 5.6 Results of numerical simulations without vertical wall for PTO data (displacement, PTO velocity and force) and absorbed power according to damping coefficient, wave case 4 (T=1.8s).....70

Figure 5.7 Results of numerical simulations without vertical wall for PTO data (displacement, PTO velocity and force) and absorbed power according to damping coefficient, wave case 9 (T=2.8s).....70

Figure 5.8 Comparison of numerical results for Case study 1: Simulation without a vertical wall according to different wave periods and PTO damping coefficients ((a): mean height of cylinder displacement, (b): mean height of PTO velocity, (c): mean height of PTO force, (d): averaged absorbed power, (e): CWR). 72

Figure 5.9 Results of numerical simulations with vertical wall for PTO data (displacement, PTO velocity and force) and absorbed power according to damping coefficient, wave case 6 (T=2.0s). $dwall$ denotes the distance between a vertical wall and a buoy. 74

Figure 5.10 Comparison of numerical results for Case study 2: Simulation with vertical wall according to wave period and PTO damping coefficient ((a): mean height of cylinder displacement, (b): mean height of PTO velocity, (c): mean height of PTO force, (d): averaged absorbed power, (e): CWR). $dwall$ denotes the distance between a vertical wall and a buoy. 75

Figure 5.11 Comparison of CWR based on the presence of absence of the vertical wall ((a) : $BPTO = 25\ Nms$, (b) : $BPTO = 50\ Nms$, (c) : $BPTO = 100\ Nms$, (d) : $BPTO = 200\ Nm$). $dwall$ denotes the distance between a vertical wall and a buoy. 77

Figure 5.12 Results of numerical simulations without vertical wall under latching control for

PTO data (displacement, PTO velocity and force) and absorbed power according to damping coefficient, wave case 9 (T=2.8s). 78

Figure 5.13 Comparison of numerical results for Case study 3: Simulation without vertical wall and latching control according to wave period and PTO damping coefficient ((a): mean height of cylinder displacement, (b): mean height of PTO velocity, (c): mean height of PTO force, (d): averaged absorbed power, (e): CWR). 79

Figure 5.14 Results of numerical simulations with vertical wall under latching control for PTO data (displacement, PTO velocity and force) and absorbed power according to damping coefficient, wave case 7 (T=2.2s). $dwall$ denotes the distance between a vertical wall and a buoy. 81

Figure 5.15 Comparison of numerical results for Case study 4: Simulation with vertical wall and under latching control according to wave period and PTO damping coefficient ((a): mean height of cylinder displacement, (b): mean height of PTO velocity, (c): mean height of PTO force, (d): averaged absorbed power, (e): CWR). $dwall$ denotes the distance between a vertical wall and a buoy. 82

Figure 5.16 Comparison of CWR based on the presence of absence of the vertical wall for $BPTO = 25\ Nms$, and $50\ Nms$. $dwall$ denotes the distance between a vertical wall and a buoy. 83

List of Tables

Table 3.1 Physical properties of the target wave energy converter (Ransley et al., 2017). 31

Table 4.1 Wave cases to which the simulation for WEC integrated with a vertical wall is applied. 43

Table 4.2 Calculation of the discretization error for the grid-spacing convergence study 49

Table 4.3 Calculation of the discretization error for time-step convergence study.....49

Table 4.4 Numerical result of the first harmonic component of cylinder displacement according to distance to vertical wall ($dwall$).....57

Table 4.5 Location of wave probes (WP) 58

Table 5.1 Wave conditions, the wave condition used for the comparison with experimental data (Windt et al., 2020a) was marked in bold. 65

Table 5.2 Comparison of amplitude values for cylinder displacement, PTO velocity and PTO force between reference and present simulation. 67

Table 5.3 Comparison of displacement of cylinder according to time-step 68

Table 5.4 Results of PTO data, Power and CWR according to the wave cases and PTO damping coefficients without a vertical wall. The case shown the highest CWR has been highlighted in bold. 71

Table 5.5 Result of PTO data, Power and CWR according to wave case and damping coefficients for the cases with the vertical wall. The case shown the highest CWR has been highlighted in bold. 76

Table 5.6 Result of PTO data, Power and CWR according to wave case and damping coefficients for the cases without the vertical wall and latching control. The case shown the highest CWR has been highlighted in bold.....80

Table 5.7 Result of PTO data, Power and CWR according to wave case and damping

coefficients for the cases with the vertical wall and under latching control. The case shown the highest CWR has been highlighted in bold.....83

Nomenclature

A_0	Amplitude of undisturbed incident wave
B_{PTO}	Damping coefficient for PTO
B_{num}	Numerical damping coefficient for PTO
c_g	Wave group velocity
$C_{\varepsilon 1}$	Model coefficient for turbulence model
$C_{\varepsilon 2}$	Model coefficient for turbulence model
d_{wall}	Distance between a wall and a buoy
f_1	Forcing coefficient
f_2	Damping function
F_{PTO}	PTO force
$\bar{F}_{PTO}$	Mean height of PTO force
g	Acceleration of gravity
H	Wave height
h	Representative grid size
k	Wave number
K_{PTO}	Rotational spring stiffness
K_{num}	Numerical stiffness coefficient for PTO
P_{abs}	Absorbed power
P_{wave}	Available power of a wave
S_c	Displacement of the PTO cylinder
S_ε	User-specified source term
S_{k_e}	User-specified source term
T_L	Latched duration
T_n	Natural period of a device
$V_\perp$	Cross-radial speed
V_B	Cross-radial speed at point B
$V_{PTO}(t)$	Velocity of PTO
V_i	Volume of phase i
N	Total number of grids
P_ε	Production terms for turbulence model
P_k	Production terms for turbulence model
$\bar{p}$	Mean pressure
p	Apparent order of the method
r	Grid refinement factor
$\bar{S}_c$	Mean height of cylinder displacement
$t_{release}$	Release time for WEC
t_{sim}	Simulation time
$t_{transition}$	Duration for transition
Δt	Time step for a simulation
T	Wave period
T_e	Large-eddy time scale
$\bar{u}_i$	Averaged Cartesian components of the velocity vector
$\bar{V}_{PTO}$	Mean height of PTO velocity
V	Volume of cell
$\bar{v}$	mean velocity

ΔV_i	Volume of the ith cell for a simulation
$width_{active}$	Active width of a device
y^+	Non-dimensional wall-adjacent grid height
z_I	Elevation of an incident wave
z_R	Elevation of a reflected wave
z_{max}	Amplitude of an incident wave
α_i	Volume fraction of phase i
β	Angle between the WEC's arm and the PTO
Θ_{WEC}	Rotational angle around a pivot point
λ	Wavelength
μ	Dynamic viscosity
ρ	Fluid density
$\rho\overline{u_i'}\overline{u_i'}$	Reynolds stresses
σ_ε	Model coefficient for turbulence model
σ_k	Model coefficient for turbulence model
$\bar{\tau}_{ij}$	Mean viscous stress tensor components
τ_{PTO}	PTO torque
ϕ_k	Solution on the kth grid
ω	Wave frequency
ω_{WEC}	Angular velocity of WEC

Abbreviations

AEP	Annual Energy Production
CAPEX	Capital Expenditure
CFD	Computational Fluid Dynamics
CPH	The number of cells per wave height
CPL	The number of cells per wave length
CWR	Capture Width Ratio
DFBI	Dynamic Fluid Body Interaction
DOF	Degree-of-Freedom
FFT	Fast Fourier Transform
LCOE	Levelized Cost of Energy
MATLAB	MATrix LABoratory
OpenFOAM	Open Field Operation and Manipulation
OWC	Oscillating Water Columns
PTO	Power Take-Off
SIMPLE	Semi-Implicit Method for Pressure Linked Equations
SWL	Still Water Level
UDF	User-Defined Function
URANS	Reynolds-Averaged Navier-Stokes
VOF	Volume of Fluid
WEC	Wave Energy Converter
WP	Wave Probes

Abstract

As the global demand for sustainable and clean energy continues to rise in the face of a rapidly changing climate, the imperative to harness power from the ocean becomes increasingly apparent. In this thesis, Wave Energy Converters (WECs) assume a pivotal role, and researchers have undertaken extensive investigations into various methodologies aimed at optimizing their efficiency. The thesis presents a comprehensive exploration of the synergistic impact that arises from the integration of latching control and coastal structures, specifically focusing on a vertical wall, to enhance the performance of a Wavestar-like WEC.

Drawing upon an extensive literature review, this study endeavours to elucidate how the coupling of WECs with coastal structures can yield substantial cost savings while simultaneously offering the dual benefits of energy production and coastal protection. To systematically analyse the influence of vertical walls, variations in Power Take-Off (PTO) damping coefficients, and the implementation of latching control on WEC performance across different wave conditions, the research employs Computational Fluid Dynamics (CFD) simulations.

Furthermore, the proposed CFD model is subjected to a comparison with other published data, undergoing processes to ensure the reliability and validity of the numerical simulation. The results showed that the presence of a vertical wall contributes a significant improvement in the Capture Width Ratio (CWR) of the WEC, particularly when it is considered within the natural period of the WEC. Furthermore, the application of latching control showed significant improvements in the WEC's performance, particularly in longer wave periods. However, it is important to note that the impact of the vertical wall becomes less pronounced as wave periods increase.

This research significantly enhances the understanding of WEC dynamics and offers insights for maximising power extraction efficiency under various wave conditions. Consequently, these findings serve as a robust foundation for a numerical simulation model of WEC systems, including numerical PTO model and latching control.

1 Introduction

1.1 Background

The exploration of renewable energy sources has become increasingly paramount in addressing the growing global demand for sustainable and environmentally friendly energy solutions. Among these sources, wave energy stands out as a promising avenue due to its abundance and the vast untapped potential it holds (Jin and Greaves, 2021). As the world seeks alternatives to conventional fossil fuels, the development of efficient Wave Energy Converters (WECs) emerges as a critical focus for researchers and engineers (Drew et al., 2009, Falcão, 2010, Day et al., 2015, Terrero González et al., 2021).

Despite significant advancements in WEC technologies, there exists a persistent challenge related to optimizing their performance and harnessing wave energy effectively. Traditional WEC designs often encounter limitations in capturing varying wave conditions and maximizing energy extraction. Recognizing this, the integration of WECs with existing coastal structures, such as vertical walls, has surfaced as a captivating area of exploration (Mustapa et al., 2017, Zhao et al., 2019b).

The coupling of WECs with vertical walls introduces a novel paradigm where the combined system aims to capitalize on the synergies between the inherent properties of both components. This integration not only leverages the structural benefits of vertical walls but also enhances the adaptability and efficiency of WECs in diverse wave environments. Understanding the intricacies of these integrated structures is crucial for unlocking their full potential and pushing the boundaries of wave energy utilization.

Moreover, Computational Fluid Dynamics (CFD) has emerged as a powerful tool in the study of WECs, providing a detailed understanding of the fluid-structure interactions involved in energy conversion (Windt et al., 2018). CFD simulations enable researchers to analyse and optimise the performance of WECs under various wave conditions, contributing valuable insights to the design and efficiency enhancement process.

Furthermore, the incorporation of latching control mechanisms into WEC systems has gained attention for its potential to optimize energy capture (Babarit and Clément, 2006, Penalba et al., 2017). Latching control offers the capability to improve WEC efficiency by precisely timing the energy absorption and release phases. This introduces a dynamic element to WEC operation, aligning it more closely with the variable nature of ocean waves. The combined study of WECs, vertical walls, and latching control presents a unique opportunity to delve into the intricate dynamics of these systems, ultimately contributing to the advancement of sustainable energy solutions.

Considering these considerations, it appears that the synergistic effects of coupling a WEC with a vertical wall, integrating latching control strategy, and utilizing CFD simulation can be comprehensively investigated to enhance our understanding of how these elements influence

WEC performance. This research will contribute to the broader discourse on harnessing wave energy for a greener and more sustainable future.

1.2 Operating principles of WECs

Wave Energy Converters (WECs) encompass various innovative designs, each employing distinctive mechanisms to capture and convert the energy embedded in ocean waves into usable electrical power. Here are the key operational principles of different WEC types (Day et al., 2015, Babarit, 2017).

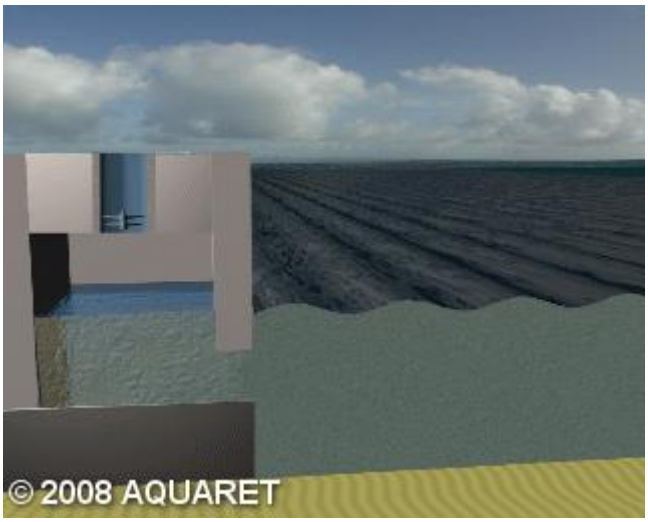

Figure 1.1 Generic view of oscillating water columns (EMEC)

- Oscillating Water Columns (OWCs): OWCs utilize air turbines as crucial components (Figure 1.1). As waves ingress the chamber, they elevate the water column, compelling the air above it through the turbine. Upon the descent of the water column, air is drawn back through the turbine. The turbine is ingeniously designed to rotate consistently, irrespective of the air's movement direction, thus generating electricity (Falcão et al., 2020, Paparella et al., 2015).

Figure 1.2 Generic view of point absorber type WEC (EMEC)

- Point Absorbers: These devices commonly incorporate hydraulic systems or direct drives for power take-off (PTO) (Figure 1.2). The wave-induced motion of the floating structure converts into pressure in a hydraulic fluid. This pressure propels a hydraulic motor, subsequently driving an electrical generator (Ruellan et al., 2010, Kramer et al., 2011).

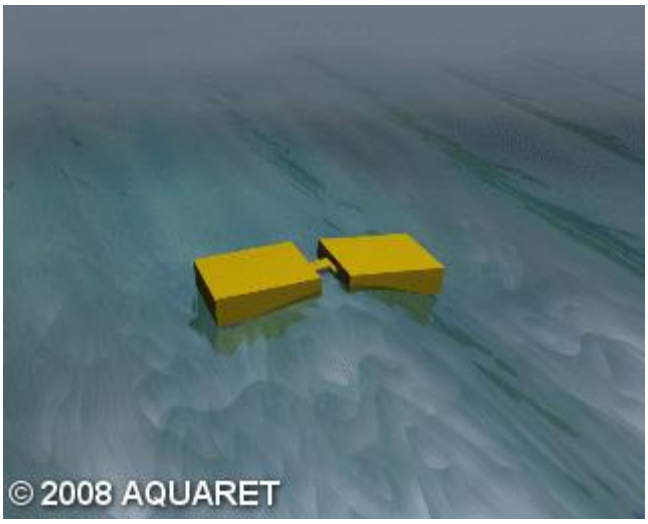

Figure 1.3 Generic view of attenuator (EMEC)

- Attenuators: Typically employing hydraulic systems for PTO, attenuators harness the relative motion between adjacent segments to pump hydraulic fluid through hydraulic motors (Figure 1.3). These motors, in turn, drive electrical generators (Yemm et al., 2012).

- Oscillating Bodies: Oscillating bodies may be submerged or semi-submerged. For instance, the Archimedes Wave Swing, a submerged point absorber with an air-filled chamber, experiences wave-induced pressure variations causing mechanical movement (Prado and Polinder, 2013). This movement is then converted into

electricity by a linear electric generator.

Figure 1.4 generic view of overtopping devices (EMEC)

- Overtopping Devices: These devices capture water propelled by waves into a reservoir above sea level. The potential energy stored in the water is subsequently converted into mechanical energy as the water is released back to the sea through low-head turbines (Kofoed et al., 2006).

It is imperative to note that despite the existence of over 1000 patented wave energy technologies, only a select few have been substantiated through rigorous numerical and experimental studies (Sheng, 2020). Each technology presents its unique advantages and challenges concerning energy capture efficiency, cost, environmental impact, and suitability for diverse wave conditions and locations (Pecher and Kofoed, 2017). As described above, several efforts have been made to deliver the WEC devices to the commercial stage, but developments were often suspended due to insufficient financial support. In order to proceed to the commercial stage, it is essential to produce a prototype and go through its own verification and demonstration steps. In addition, most prototypes are quite large, so the costs of construction and maintenance are also significantly high. To this end, support from government and private enterprises is needed. Although many studies regarding WECs have been conducted, it looks that the proof of technology in terms of acceptable level of cost for producing electricity is fundamental to lead to the commercial stage.

In this study, point absorber type has been focused to investigate interactions between a WEC and a vertical wall. Point absorber type generally does not have a limitation of size, compared to other types of WEC such as OWCs and overtopping devices. This point absorber WEC can be divided into two main types: bottom-fixed and pivoted.

Bottom-fixed point absorbers are anchored to the seabed. They capture energy directly from the vertical motion of the waves as the device moves up and down. Pivoted point absorbers, on the other hand, rotate around a pivot point, which is typically attached to a vertical wall or

another structure. This design also allows the device to capture energy from the vertical motion of the waves. Pivoted Point Absorbers are more suitable for vertical walls for several reasons. First, they offer structural advantages. The pivot point connected to the vertical wall enhances the stability of the structure, with the wall itself providing additional support. Additionally, using a vertical wall reduces the complexity associated with anchoring structures to the seabed, simplifying the installation process, especially in deep waters where seabed anchoring can be costly and technically challenging. Second, pivoted Point Absorbers offer better maintenance and accessibility. Structures attached to vertical walls are easier to access for maintenance, whereas bottom-fixed structures anchored to the seabed can be challenging and expensive to maintain, particularly in deep waters. Therefore, pivoted Point Absorbers are more suitable for deployment near vertical walls due to their structural stability, installation simplicity, and maintenance ease.

1.3 Research objectives and scope

The primary objective of this research is to advance the understanding of WEC performance through a comprehensive exploration of the synergies arising from the integration of a WEC with a vertical wall, coupled with the implementation of a latching control strategy.

1.3.1 Investigating the integration of a WEC with vertical walls

The first major objective is to delve into the intricate dynamics of a WEC when coupled with a vertical wall. By elucidating the interaction between these two components, the aim is to identify and capitalize on the potential benefits that arise from this novel integration. This includes an in-depth analysis of how the characteristic of a vertical wall influences the overall performance of a WEC under varying wave conditions. Experiments and numerical simulations are conducted to quantify the impact of this coupling on energy capture efficiency and power extraction.

1.3.2 Assessing the influence of a latching control strategy

Another key objective is to assess the impact of the latching control strategy on WEC performance. Latching control introduces a dynamic element to the energy absorption process, allowing for timing in response to incoming wave patterns. By systematically implementing and analysing various latching control mechanisms, one of the objectives of this research is to optimise the energy conversion efficiency of a WEC.

1.3.3 Understanding WEC performance by computational fluid dynamics (CFD) simulations

Computational fluid dynamics (CFD) simulation will be employed to model and analyse the fluid-structure interactions within the WEC-vertical wall system. CFD provides a powerful platform for predicting flow patterns and hydrodynamic responses, offering a detailed understanding of the hydrodynamic performance of a Wave Energy Converter (WEC). This

computational approach enables us to explore a broader range of operating conditions, contributing to a more comprehensive assessment of the integrated system's behaviour.

Insights into the complex interplay of forces and pressures exerted by varying wave conditions on the WEC structure can be gained by leveraging CFD. This includes a detailed examination of flow velocities, pressures, and turbulence, providing a holistic understanding of the dynamic responses exhibited by the WEC under different environmental scenarios.

The performance of the WEC-vertical wall system across various parameters, including the distance between a WEC and a vertical wall, wave conditions, and power take-off (PTO) settings, can be investigated through systematic simulations. This not only enhances our ability to predict the system's behaviour under diverse wave conditions but also contributes valuable data for optimising the design and operational parameters of the integrated system.

1.3.4 Addressing the limitations and defining the research scope

Objective of integrating a WEC with a vertical wall and implementing a latching control strategy, it is imperative to recognise and address the inherent limitations in any research endeavour. The specific boundaries within which this investigation unfolds is crucial to ensuring a well-defined and manageable research scope. By explicitly acknowledging these limitations, the research aims to strike a balance between depth and breadth, ultimately providing findings that are both rigorous and applicable to the broader field of wave energy conversion.

While the primary focus is on the integration of a WEC with a vertical wall and the implementation of a latching control strategy, it is essential to highlight certain constraints in this research. The target WEC model for this study is the Wavestar (Zurkinden et al., 2014, Jakobsen, 2015, Jakobsen et al., 2016, Ransley et al., 2017, Windt et al., 2020a, Windt et al., 2020b), and as such, the applicability of the findings may be constrained to geometries and working principles resembling the Wavestar. The outcomes may have limited extrapolation to WECs with substantially different configurations.

1.4 Thesis structure

The thesis is structured into five chapters, each focusing on specific aspects of a wave energy converter (WEC) and its integration with a vertical wall:

- Chapter 2 (Literature review) provides a comprehensive overview of previous publications on WECs, covering operating principles, performance evaluation criteria, and the significance of integrating WECs with coastal structures. Additionally, it reviews previous works on the numerical modelling of Power Take-Off (PTO) and latching control in Computational Fluid Dynamics (CFD).
- Chapter 3 (Methodology) illustrates the general methodology proposed in the thesis and offers a detailed description of the numerical setup for WEC-vertical wall simulations.

- Chapter 4 (CFD simulation for WEC integrated with a vertical wall) conducts a numerical study on the hydrodynamic performance of WEC at different distances from a vertical wall under various wave conditions. This chapter includes comparisons of the numerical WEC simulations with the existing experimental measurements and explores the hydrodynamic performance concerning the distance to the vertical wall.
- Chapter 5 (CFD simulation for WEC integrated with a vertical wall and latching control) analyses the effects of Power Take-Off (PTO) and latching control on WEC integrated with a vertical wall. It includes the implementation of PTO, comparisons with experimental measurements, investigation of the vertical wall's influence on WEC performance with various PTO damping coefficients, and exploration of the impact of latching control under different PTO damping conditions.
- Chapter 6 (Summary and Discussion) provides a discussion of the achievement of the research aims and objectives, contributions to the maritime industry, as well as limitations of this research and recommendations for future work. It also summarises the meaningful contributions drawn from this research work.

2 Literature review

2.1 Integration of vertical wall with WEC

2.1.1 Overview

When incorporated into WEC systems, a vertical wall exhibits distinctive characteristics and advantages that significantly contribute to its efficacy in harnessing wave energy.

- Enhanced Stability: A vertical wall provides structural stability, serving as a robust foundation for WEC installations. Its upright design minimizes lateral movements, ensuring the WEC remains steadfast in the face of varying wave conditions. This stability is fundamental for ensuring consistent and reliable WEC operation (Mustapa et al., 2017).
- Wave Focusing and Standing Wave Formation: The vertical orientation of a wall facilitates the focusing and standing wave formation of incoming waves. This characteristic allows for the concentration of wave energy in specific areas, optimizing the interaction between waves and the WEC. By directing and concentrating wave forces, a vertical wall enhances the efficiency of energy capture. The term “standing wave” refers to a specific type of wave pattern that appears to be stationary. It is formed when incoming waves are reflected upon themselves, creating constructive interference. This phenomenon leads to the formation of nodes and antinodes, where the amplitude of the wave oscillation varies. In the case of a vertical wall, its design encourages the development of standing waves, enabling a more prolonged and concentrated exchange of energy with the WEC. The establishment of standing waves contributes to the enhanced efficiency of energy absorption and, consequently, the improved overall performance of the wave energy converter system (Coiro et al., 2016, Reabroy et al., 2019).
- Increased Wave Interaction Time: A vertical wall extends the interaction time between waves and WEC components. As waves encounter the wall, they induce a prolonged exchange of energy, allowing for more effective energy absorption. This increased interaction time enhances the overall performance and energy conversion efficiency of the WEC (Krishnendu and Ramakrishnan, 2020, Krishnendu and Ramakrishnan, 2021).
- Potential for Resonance: The geometric design of a vertical wall can be tailored to match specific wave frequencies, creating conditions conducive to resonance. Resonance occurs when the natural frequency of the WEC aligns with that of incoming waves, leading to amplified energy absorption. A vertical wall offers the potential to customize resonance conditions for optimized energy capture (Kara, 2021).
- Ease of Integration with WEC Mechanisms: A vertical wall provides a versatile platform for integrating various WEC mechanisms, such as oscillating water columns or point absorbers. Its vertical structure allows for seamless incorporation of WEC components, ensuring a cohesive and efficient system design. This ease of integration

contributes to the adaptability of a vertical wall in diverse wave energy conversion technologies (Krishnendu and Ramakrishnan, 2020).

2.1.2 Previous research of integrating WEC and breakwaters

According to reviews of Mustapa et al. (2017) and Zhao et al. (2019b), the combination of WEC devices with other marine facilities such as breakwaters has become common in coastal areas. The benefits of cost-sharing, space-sharing and multi-functionality by the integration of marine structures lead to reducing the construction cost. Some innovative research about floating breakwaters combined with WECs, which generate electricity using the heave motion, can be found in those studies; a moonpool type floating breakwater-WEC (Cheng et al., 2021, Tay, 2022a, Tay, 2022b), a pontoon type floating breakwater-WEC (Ning et al., 2017, Ning et al., 2018, Guo et al., 2020), a vertical pile-restrained WEC type (Ning et al., 2016, Chen et al., 2020), a Comb-type breakwater-WEC (Zhao et al., 2019a, Zhao et al., 2020, Zhao et al., 2021) and the Berkeley Wedge (TBW) type (Tom et al., 2018, Tom et al., 2019, Zhang et al., 2019). The main objective of those research studies based on a linear potential theory is to enhance the performance of the WEC and the wave attenuation function of the floating breakwaters. Another approach to the integration of breakwaters and WECs is the combination of WECs and a fixed breakwater. McIver and Evans (1988), Mavrakos et al. (2004), and Schay et al. (2013) found that the power obtained by point absorbers in front of a fixed breakwater was much greater than that obtained by the same independent point absorbers. Coiro et al. (2016) mentioned the stationary wave system which was established in front of the vertical wall itself because of the incident wave and the reflected wave from the wall. They expected that the stationary wave system should be very sensitive to the incident wavelength, which would affect the performance of the power output. Reabroy et al. (2019) studied the differences in the WEC motion with the distance between the WEC and the breakwater wall in a certain wave period and found that the breakwater effect indicated that the point absorber type of WEC can improve the hydrodynamic performance of WEC such as the heave motion of the WEC. Konispoliatis and Mavrakos (2020), Konispoliatis and Mavrakos (2021) and Zhao et al. (2019a) have conducted a parametric study of the breakwater-WEC spacing including the gap between WEC devices and the breakwaters and the arrangement study of WECs. Wang et al. (2022) investigated the hydrodynamic performance of the point absorber with Jarlan-type breakwater, which is a conventional breakwater type in coastal areas. The most common consideration regarding the integration of fixed breakwater-WEC is generally how to adjust the gap between the fixed breakwater and WEC device in order to enhance the wave power absorption.

The numerical studies using computational fluid dynamics (CFD) to understand the characteristics of WEC are gradually increasing. A comprehensive review of the WEC research using CFD over the past two decades can be found in Windt et al. (2018). When CFD is used in WEC's research and development, cost savings can be obtained compared to experiments, and numerical studies can be performed under various environmental and physical conditions without significant restrictions. Therefore, it is considered that the

importance of acquiring numerical tools for WEC using CFD is an increasing trend amongst researchers working in this area. Most studies related to the combination of WEC devices with marine facilities have been investigated by a linear potential flow theory and experimental method. To date, the majority of the CFD studies with WECs have focused on the sole WEC such as their heave response to the incident wave. It is expected that the CFD work described in this thesis will help to understand the influence of the gap between a WEC device and a vertical wall at intermediate water depth. As the time the author wrote this thesis, there were no studies on WECs under various wave conditions and distances from a vertical wall using CFD.

2.2 Implementation of numerical PTO model

This section delves into the challenges associated with integrating PTO systems, especially hydraulic PTO systems, into CFD software, addressing conceptual integration issues, computational complexities, and the lack of standardisation. Despite these challenges, researchers are exploring various approaches:

- Modular design: Developing modular software frameworks where dedicated modules handle specific functionalities like PTO dynamic and control strategies. This allows for easier development, maintenance, and customization (Jusoh et al., 2019).
- Reduced-order modelling: Discusses the utilisation of simplified models for PTO systems within CFD frameworks, balancing accuracy, and computational efficiency, with a focus on validation and verification (Davidson et al., 2019, Windt et al., 2020a)
- Co-simulation Framework: Examines the development of communication protocols enabling co-simulation between CFD solvers and dedicated PTO modelling tools, providing advanced CFD capabilities with specialised PTO models (Penalba et al., 2018).

Some open-source CFD software such as OpenFOAM provides functionalities for user-defined functions (UDFs), allowing researchers to implement simplified PTO models within the framework. Several commercial CFD software such as Star-CCM+ by Siemens, Fluent and CFX by Ansys are actively researching and developing integrated functionalities for PTO systems. In the case of the pivoted point absorber type, which is the target device of this study, it differs from the bottom-fixed point absorber. Instead, it rotates around a hinge, meaning the compression direction of PTO is different from the movement of the buoy. In other words, for a bottom-fixed point absorber, the motion axis of the buoy coincides with the motion axis of the PTO. However, for a pivoted point absorber, the cross-radial direction of the buoy motion is normal to the motion axis of the PTO. Therefore, in the numerical simulation, this must be adjected to account for these difference at each time step. As of the time of writing this study, there is limited guidance available for the development of WECs and PTO model based on CFD. In this study, reduced-order modelling of PTO model is employed using the field functions and Dynamic Fluid Body Interaction (DFBI) in Star-CCM+ to act as a numerical PTO model.

2.3 Implementation of latching control for WEC

In the early 80's, Budal and Falnes (1980) highlighted a crucial condition for maximising energy production in point absorber type WECs, specifically, the need to maintain velocity in phase with the excitation force. To meet this condition, they introduced phase control, commonly known as latching control, in their heaving buoy WEC. Latching control involves immobilising the body at the precise moment when its velocity reaches zero at the end of an oscillation, releasing it at the most opportune time. The challenge lies in determining the optimal duration for which the system remains locked. An advantageous feature of latching control is its passive, requiring no energy input during an engagement, as forces do not work when velocity is zero.

Various latching mechanisms have been suggested to facilitate latching or locking actions in WECs, including friction coupling/brake (Salter et al., 2002), friction clutch (Falnes, 2001), magnetic locking mechanism (Korde, 2000), mechanical clamps (Falnes and Kurniawan, 2020), and electromagnets (Bjarte-Larsson and Falnes, 2006). A practical latching method for WECs involves integrating a hydraulic PTO system with a valve (Falcão, 2008). An alternative latching control method using pneumatic cylinders with open/close valves has also been development (Falcão and Henriques, 2016). In these hydraulic and pneumatic systems, achieving latching is straightforward by closing the valve. Subsequently, the introduction of a high speed stop valve (HSSV) in the hydraulic PTO system allows for instant latching (Henriques et al., 2016).

Numerous studies by semi analytical method, primarily focused on single DOF systems like heaving buoy wave energy converters, have explored latching control (Babarit et al., 2004, Babarit and Clément, 2006, Giorgi and Ringwood, 2016, Avalos and Estefen, 2021). In regular waves, particularly when the wave period exceeds the natural period of the device, employing half the difference between the wave period and the natural period as the latching duration provides a reasonable approximation and yields favourable results (Iversen, 1982). Additionally, the study by Ringwood and Butler (2004) proposed an optimised latching duration for regular and monochromatic waves, establishing a foundation for a constant latching duration without prediction of future incoming wave.

It is evident that many studies show the significant improvement of the WEC performance when the latching control is implemented. Hoskin and Nichols (1987) applied the optimal latching duration for an oscillating water column and a heaving buoy device. The study demonstrated an efficiency improvement of approximately 800% in a random sea. Experimental tests have been carried out by researchers such as Bjarte-Larsson and Falnes (2006), who conducted latching tests on an axisymmetric floating body in a wave tank, observing a substantial increase in captured power, up to 4.3 times. Additionally, Durand et al. (2007) performed tank tests implementing a latching control strategy on the SEAREV device. The results showed a substantial increase in energy production, up to ten times with regular

waves and a notable improvement from 50% to 86% with irregular waves, as compared to simulations.

Due to computational cost considerations, linear models such as WEC-Sim based on a MATLAB open-source code (WEC-Sim) and linear potential wave theory, are commonly used to assess the motion of WECs. However, research involving control strategies and power capture evaluations indicates the substantial impact of nonlinear effects on device performance (Penalba et al., 2017, Penalba and Ringwood, 2018, Penalba et al., 2018). In a study by Giorgi and Ringwood (2016), the research delved into latching control strategy using OpenFOAM software based on computational fluid dynamics. The outcome of this study facilitated the analysis of the nonlinear motion of WEC and the interpretation of WEC movements under the influence of latching control. The results revealed a pronounced nonlinear effect, especially at the natural period of the WEC.

If a different program is used, a new algorithm will be needed. In this study, since Star-CCM+ will be used, it was necessary to redesign the algorithm accordingly and reinterpret and complement the existing algorithms. Additionally, several enhancements were made to replicate the same latching control effects in the numerical simulation. In this study, numerical latching control is employed using the field functions and Simulation function in Star-CCM+, which provide logical algorithms and decision gates, to act as a latching control.

2.4 Evaluation criteria for WEC performance

The evaluation of WECs encompasses key performance criteria essential for enhancing efficiency and reliability. These criteria play a crucial role in gauging the effectiveness of WEC systems and guiding optimization efforts (Clément et al., 2002, Coe and Neary, 2014, Day et al., 2015, Pecher and Kofoed, 2017, Ahamed et al., 2020, Falcão, 2010).

- Power efficiency: This metric involves the effectiveness of a WEC in converting the captured wave energy into usable electrical power. A higher power efficiency indicates a more energy conversion process, contributing to increased electricity generation.
- Energy conversion: Energy conversion is the pivotal process by which a WEC transforms the kinetic and potential energy present in ocean waves into electrical energy. The efficiency of this process is a critical performance metric, directly impacting the overall effectiveness of the WEC.
- Capture Width Ratio (CWR): The Capture Width Ratio (CWR) provides a measure of how effectively a WEC captures wave energy. It is defined as the ratio of the power captured by the WEC to the wave power in the sea per unit width. This metric highlights the WEC's efficiency in extracting energy from the waves.
- Capacity factor: The capacity factor is the ratio of the actual energy output over a specific period to the potential energy output if the WEC operated at full capacity for the same duration. It provides insights into the consistent utilization of the WEC's

capacity over time, offering a valuable indicator of its performance.

- Annual Energy Production (AEP): AEP quantifies the total amount of electrical energy a WEC can generate over a year. This metric is pivotal for assessing the overall productivity and output capacity of the WEC on an annual basis.
- Maintenance impact: Consideration of maintenance impact involves assessing how maintenance activities affect the WEC's productivity. Larger WECs, with longer predictive maintenance windows during low seasons, tend to have a lower impact on annual productivity, contributing to enhanced operational efficiency.
- Evaluation of feasibility: Capital Expenditure (CAPEX) refers to the initial investment required to design, build, and deploy a WEC. The rate of CAPEX increase should align with the rate of increase in WEC production with scale. This metric provides insights into the economic efficiency of the WEC in relation to its capital investment. Levelized Cost of Energy (LCOE) is a crucial metric that assesses the cost-effectiveness of energy generation over the entire lifespan of a WEC project. To achieve a competitive LCOE is essential for the renewable energy sector. It can be compared with wind turbine. Multiple smaller converters could be cost-effective due to reduced material costs instead of enlarging a wave absorbing body.

These comprehensive metrics collectively provide a view of the WEC's performance, encompassing not only its operational effectiveness but also its economic viability and maintainability. The continual refinement and optimization of WECs based on these metrics contribute to their sustained advancement as a viable renewable energy technology.

2.5 Significance of integrating WEC with coastal structures

This section delves into an extensive exploration of the importance and implications of combining WECs with marine structures (Mustapa et al., 2017, Zhao et al., 2019b, Cheng et al., 2022).

- Enhances Structural Synergy: The integration of WECs with marine structures creates a synergistic relationship, where the structural elements complement each other. This collaboration enhances the overall stability and resilience of the system, allowing for efficient energy capture in diverse wave conditions.
- Optimised Resource Utilisation: Combining WECs with existing marine structures allows for the optimised utilisation of marine resources. Utilising pre-existing structures, such as offshore platforms or breakwaters, provides a cost-effective and sustainable approach to deploying WECs, minimising the need for additional infrastructure.
- Infrastructure Synergy for Coastal Protection: Certain marine structures, such as breakwaters, not only provide a foundation for WECs but also serve coastal protection functions. The integration thus contributes to a dual-purpose infrastructure that addresses energy needs while enhancing coastal resilience against wave-induced erosion and storm surges.

- Economic Viability and Scalability: Integrating WECs with marine structures enhances economic viability by capitalizing on existing infrastructure. This approach reduces installation costs and accelerates the scalability of wave energy projects, making them more economically feasible for widespread adoption.

In conclusion, the integration of WECs with marine structures offers a myriad of benefits, ranging from improved stability and resource utilization to environmental compatibility and economic viability. This collaborative approach not only advances the field of wave energy conversion but also aligns with sustainable practices, fostering the harmonious coexistence of energy generation and marine ecosystems.

3 Methodology

This chapter will provide the general methodology used in this thesis, with a detailed description of the numerical setup of the current CFD model. A robust methodology is essential to ensure the accuracy and reliability of the simulations conducted in the subsequent sections. The following sections provide an overview of the key components of the methodology.

3.1 Research Methodology

The research methodology utilized in this thesis involves four primary phases for WEC-vertical wall simulations: 1) defining goals and scope, 2) developing numerical models, 3) conducting simulations of WEC-vertical wall interactions, and 4) analysing the results.

The initial phase focuses on establishing the overarching research objective and specifying the boundaries of the analysis. The scope of numerical simulations must be clearly defined to accurately capture the dynamics of a WEC, the interaction between a WEC and a vertical wall, as well as the functioning of a PTO and latching control. The scope encompasses the following elements:

- Utilise a CFD solver and schemes for WEC-vertical wall simulations.
- Clearly define the WEC type, geometry, wave conditions, and details on PTO damping coefficients and a predetermined latching duration.
- Consider environmental conditions, including intermediate water depth, regular waves, and the presence of a vertical wall.
- Implement a user-defined numerical model to simulate the operation of the PTO mechanism and latching control.

Considering the analysis scope, the second phase involves establishing the numerical setup for a CFD model representing WEC-vertical wall interactions. Precision is crucial in numerical modelling, and the following features require careful consideration:

- Governing equations to be solved.
- Establishing coordinate systems for WEC and PTO.
- Determination of Mesh resolution and the time step.
- Computational domain and boundary conditions.
- Wave generation and absorption.
- Mechanism for the PTO and latching control.

In the third phase, the initial step involves conducting a WEC simulation in the absence of a vertical wall, serving as a reference for this research and validating the CFD model. Subsequently, simulations are carried out with the inclusion of a vertical wall to assess and compare its impact. To discern the influence of the vertical wall, additional simulations are conducted, varying the distance between the WEC and the vertical wall. Following this, an examination of the effects of Power Take-Off (PTO) damping coefficients is undertaken. Lastly, an investigation into the impact of latching control is conducted.

In the fourth phase, this research presents and discusses comprehensive results, encompassing crucial hydrodynamic features, the performance of both the Wave Energy Converter (WEC) and Power Take-Off (PTO), as well as pertinent flow fields in intricate detail.

3.2 Numerical modelling

This thesis employed the commercial Computational Fluid Dynamics (CFD) software STAR-CCM+ developed by Siemens (Siemens, 2020) for numerical simulations. Specifically, version 15.04 was used for Chapter 4, while version 17.04 was employed for Chapter 5. The subsequent sub-sections provide a detailed overview of the numerical schemes incorporated in this research.

3.2.1 Target geometry

The target wave energy converter (WEC) in this thesis is a Wavestar-like device which is considered a pivoted point absorber type WEC. The Wavestar WEC consists of a hemisphere-shaped buoy with a single operational degree-of-freedom (DOF) in pitch motion and a hydraulic power take-off (PTO) cylinder (Hansen et al., 2013, Zurkinden et al., 2014, Jakobsen, 2015, Jakobsen et al., 2016, Ransley et al., 2017, Penalba et al., 2018, Windt et al., 2020a). Figure 3.1 shows the schematic view of the buoy and the PTO cylinder, and the physical properties of the target WEC are presented in Table 3.1. The buoy is configured with a pivotal point, denoted as point A, where an arm is connected, allowing for pitch motion along a fixed axis. The PTO cylinder's displacement $S_c(t)$, the distance between the moving point B and fixed-point C, varies based on the WEC device's position. $\beta(t)$ is the angle between the WEC's arm and the PTO, which will be discussed in more detail later when introducing a numerical PTO model. Note that Chapter 4 exclusively focuses on the hydrodynamic performance of the WEC without incorporating the numerical model of the PTO. In contrast, Chapter 5 encompasses both the numerical PTO model and an evaluation of the overall performance of the WEC.

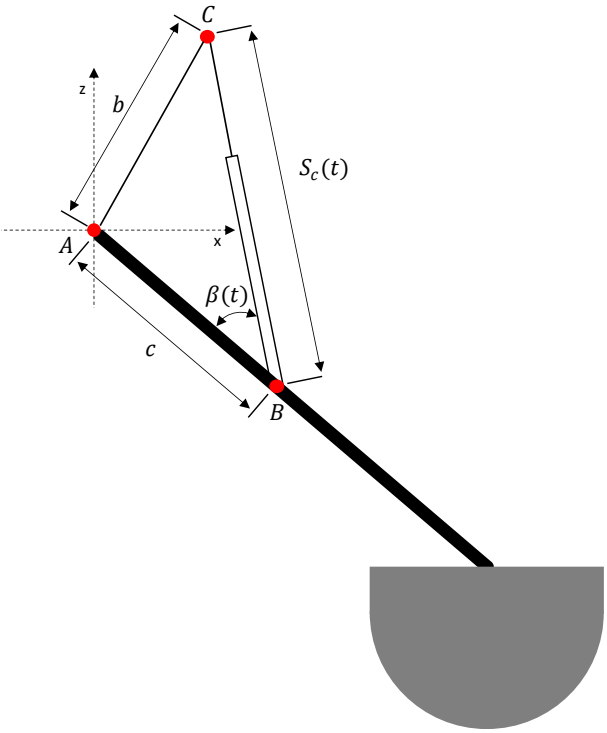

Figure 3.1 Schematic of the WEC (not at scale) including the centre of rotation (Point A) and the position of the hydraulic PTO cylinder (Point B and C).

Table 3.1 Physical properties of the target wave energy converter (Ransley et al., 2017).

	Value	Unit
Mass	220	kg
Centre of Mass:		
X	-0.2886	m
Y	0	m
Z	0.3245	m
Moment of Inertia	124.26	kgm^2
Centre of rotation (Point A)		
X	-1.684	m
Y	0	m
Z	1.655	m
Point B (relative to the centre of mass)		
X	-1.147	m
Y	0	m
Z	3.004	m
Point C		
X	-0.5684	m
Y	0	m
Z	0.8635	m
Submergence (in equilibrium)	0.4	m
Diameter of a buoy (at SWL)	1.0	m
Water depth	3.0	m

3.2.2 Governing equations

An unsteady Reynolds-Averaged Navier-Stokes (URANS) method was used to solve the governing equations, including the mass and momentum of conservation using the commercial CFD software Star-CCM+. The averaged continuity and momentum equations

for unsteady incompressible flows without body forces are expressed in tensor notation and Cartesian coordinates as follows (Ferziger et al., 2002):

$$\frac{\partial(\rho\bar{u}_i)}{\partial x_i} = 0 \tag{3.1}$$

$$\frac{\partial(\rho\bar{u}_i)}{\partial t} + \frac{\partial}{\partial x_j}\left(\rho\bar{u}_i\bar{u}_j + \rho\overline{u_i'u_i'}\right) = -\frac{\partial\bar{p}}{\partial x_i} + \frac{\partial\bar{\tau}_{ij}}{\partial x_j} \tag{3.2}$$

in which $\bar{\tau}_{ij}$ are the mean viscous stress tensor components, as shown in Eq. (3.2)

$$\bar{\tau}_{ij} = \mu\left(\frac{\partial\bar{u}_i}{\partial x_j} + \frac{\partial\bar{u}_j}{\partial x_i}\right) \tag{3.3}$$

and $\bar{p}$ is the mean pressure, $\bar{u}_i$ is the averaged Cartesian components of the velocity vector, $\rho\overline{u_i'u_i'}$ is the Reynolds stresses, ρ is the fluid density and μ is the dynamic viscosity.

In order to compute the fluid flow in the computational domain, the RANS solver uses a finite volume method that discretises the integral formulation of the governing equations. The continuity and momentum equations were solved sequentially with a predictor-corrector approach. For spatial, a second-order upwind scheme was applied to convection and diffusion terms and for temporal, a second-order temporal discretisation was used. A semi-implicit method for pressure linked equations (SIMPLE) algorithm was used to solve the pressure velocity coupling.

A realizable $k-\varepsilon$ turbulence model was chosen in this study, which is generally used in many types of numerical simulations in ocean engineering. The transport equations for the kinetic energy k_e and the turbulent dissipation rate ε are:

$$\frac{\partial}{\partial \mathrm{t}}(\rho k_e) + \nabla\cdot(\rho k_e\bar{\mathrm{v}}) = \nabla\left[\left(\mu + \frac{\mu_t}{\sigma_k}\right)\nabla k_e\right] + P_k - \rho(\varepsilon - \varepsilon_0) + S_{k_e} \tag{3.4}$$

$$\frac{\partial}{\partial \mathrm{t}}(\rho\varepsilon) + \nabla\cdot(\rho\varepsilon\bar{\mathrm{v}}) = \nabla\left[\left(\mu + \frac{\mu_t}{\sigma_\varepsilon}\right)\nabla\varepsilon\right] + \frac{1}{T_e}C_{\varepsilon1}P_\varepsilon - C_{\varepsilon2}f_2\rho\left(\frac{\varepsilon}{T} - \frac{\varepsilon_0}{T_0}\right) + S_\varepsilon \tag{3.5}$$

where, $\bar{\mathrm{v}}$ is the mean velocity, μ is the dynamic viscosity. σ_k, σ_ε, $C_{\varepsilon1}$, and $C_{\varepsilon2}$ are model coefficients and P_k and P_ε are production terms. f_2 and T_e are damping function and large-eddy time scale, respectively. S_{k_e} and S_ε are the user-specified source terms. The two-layer approach, first suggested by (Rodi, 1991), is also included in the turbulence model to consider low Reynolds number type meshes $y^+\sim1$ or wall-function type meshes $y^+ > 30$. The range of the Reynolds number in this study is from 1.5×10^6 to 3.4×10^6 and this flow can be considered in a turbulent regime. In order to numerically model the motion of the WEC in response to external wave forces and moments, the dynamic fluid body interaction (DFBI) scheme was applied to the WEC which allows the pitch motion. The DFBI scheme

can calculate the hydrodynamic forces and moments acting on the rigid body and solve the governing equations of the rigid body motion to determine the next position of the rigid body for the next time step.

The volume of fluid (VOF) technique, proposed by (Hirt and Nichols, 1981) is used to define the free surface (here, air-water interface). The VOF multiphase model is implemented in the current simulation to describe the distribution of phases and the position of the interface. The fields of phase volume fraction α_i are utilised for this purpose, where α_i represents the volume fraction of phase i and is defined as:

$$\alpha_i = \frac{V_i}{V} \tag{3.6}$$

Here, V_i is the volume of phase i in the cell and V is the volume of the cell. The volume fractions of all phases in a cell must sum up to one:

$$\sum_{i=1}^{N} \alpha_i = 1 \tag{3.7}$$

Where N is the total number of phases. The value of the volume fraction allows the identification of different phases or fluids in a cell. The volume fraction (α_i) ranges from ranging from 0 to 1, indicating the relative proportion of fluid in each cell ($\alpha = 0$: non-wetting phase (air), $0 < \alpha < 1$: two-phase interface (free surface), $\alpha = 1$: wetting phase (water)). In the two-phase interface, density and viscosity are expressed as a smooth function of the volume fraction. As the simulation progresses, the volume fraction function, defined across the entire computational domain, is advected by the underlying fluid motion. The VOF approach has been widely applied in various CFD simulations to accurately depict free surface positioning, as demonstrated in studies such as Tezdogan et al. (2016), Kavli et al. (2017), Terziev et al. (2019), and Terziev et al. (2020), Kim et al. (2021), Kim and Tezdogan (2022).

3.2.3 Computational domain and boundary conditions

The computational domain was constructed using STAR-CCM+, a commercial software package employing the Cartesian cut-cell method. In this research, two different computational domains were employed: One computational domain focused on simulating conditions without a vertical wall, while the other considered the presence of a vertical wall. Figure 3.2 shows a present computational domain and selected boundary conditions for the simulation without a vertical wall. For the simulation case without the vertical wall, the WEC is positioned in the centre of the computational domain of 6λ (λ: wavelength) length, 1λ width, 3m water depth, and 3.75m gap between the still water level (SWL) and the top boundary. In order to avoid unnecessary numerical reflection from the boundary, wave forcing scheme has been implemented as suggested and investigated thoroughly by several

authors (Kim et al., 2012, Perić and Abdel-Maksoud, 2016, Peric, 2019, Perić et al., 2022). The length of the relaxation zone, where the wave forcing scheme is applied, is set to 2λ, meeting the minimum requirement for the length of this zone. Notable, this zone is implemented in both the inflow and outflow areas of the simulation, the strength of the forcing coefficient, denoted as f_1, varies smoothly from zero to the maximum value at the boundary. The optimum forcing coefficient f_1, as suggested by Perić and Abdel-Maksoud (2016), is derived from Equation (3.8).

$$f_1 = \pi\omega \tag{3.8}$$

Here, ω represents the wave frequency ($= 2\pi/T$).

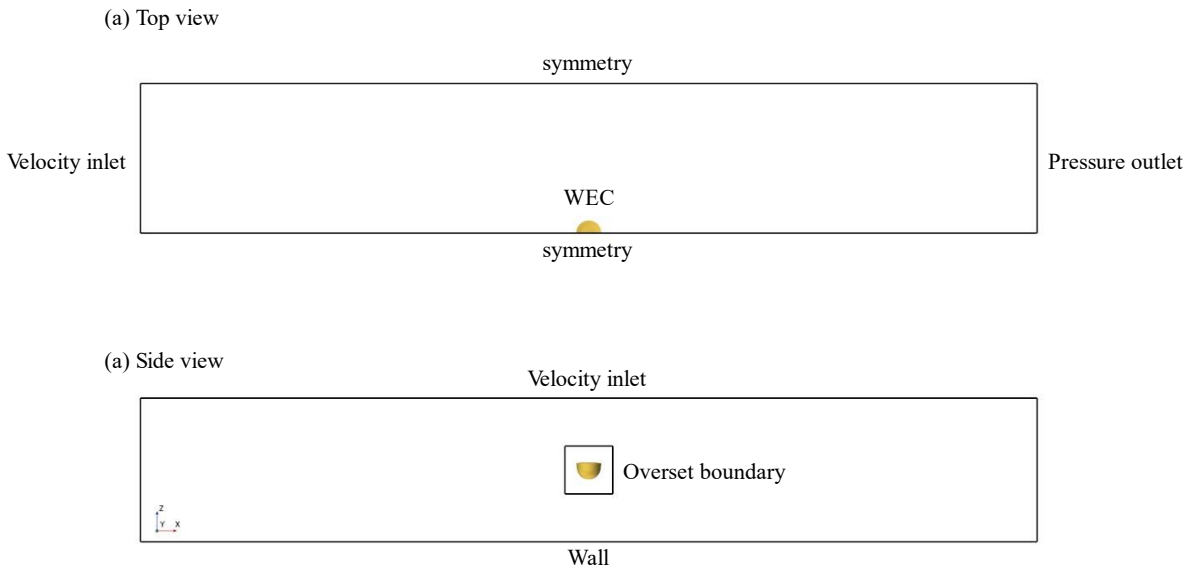

Figure 3.2 Present computational domain and boundary conditions for a simulation case without the vertical wall.

To generate regular waves accurately and consistently throughout a calculation time, three types of refinement zones have been defined (See Figure 3.3). The first refinement zone has the same length as the computational domain and is positioned above and below the SWL by twice the wave height of a wave case, with the reference point for height being the SWL at z=0. The mesh resolution for the first refinement zone is set to 12 cells per wave height and over 100 cells per wavelength. This mesh resolution is based on the guideline for ship CFD application from ITTC (2011). From this guideline, a minimum of 80 cells per wavelength was required on the free surface. The second refinement zone has the same length as the first zone but has a height twice that of the first zone. The mesh resolution for the second zone is 6 cells per wave height. The third refinement zone is centred around the buoy, with a length three times the buoy diameter and a width 1.5 times the diameter. This zone consists of the same grid resolution as the first zone per wave height.

The computational domain consists of a background mesh region and an overset mesh region. For the boundary conditions for the background mesh region, a velocity inlet boundary condition was established at the inflow boundary. This condition specifies the known distribution of velocity and fluid properties. The horizontal and vertical velocities, along with surface elevation for the inflow properties, were calculated using a fifth-order wave model proposed by Fenton (1985). To reduce computational resources, a symmetry plane was placed at the centre of the buoy. At the outflow boundary, a pressure outlet condition was implemented. As for the buoy, a non-slip wall boundary condition was applied.

A overset mesh approach was employed to study the movements of the WEC model, enabling the accurate representation of its interactions with the surrounding fluids. To implement the overset mesh technique, a minimum of two different mesh regions was necessary. In this research, the computational domain included a background mesh region for simulating regular waves and an overset mesh region, which involved cutting a hole from the background mesh to simulate the body-fluid interaction. To ensure smooth interpolation of fluid data between the two mesh regions, it is essential to minimise the difference in mesh sizes for the corresponding meshes in both regions. Therefore, the size of the third refinement zone has been configured to sufficiently cover the overset mesh region, which moves in response to the motion of the WEC.

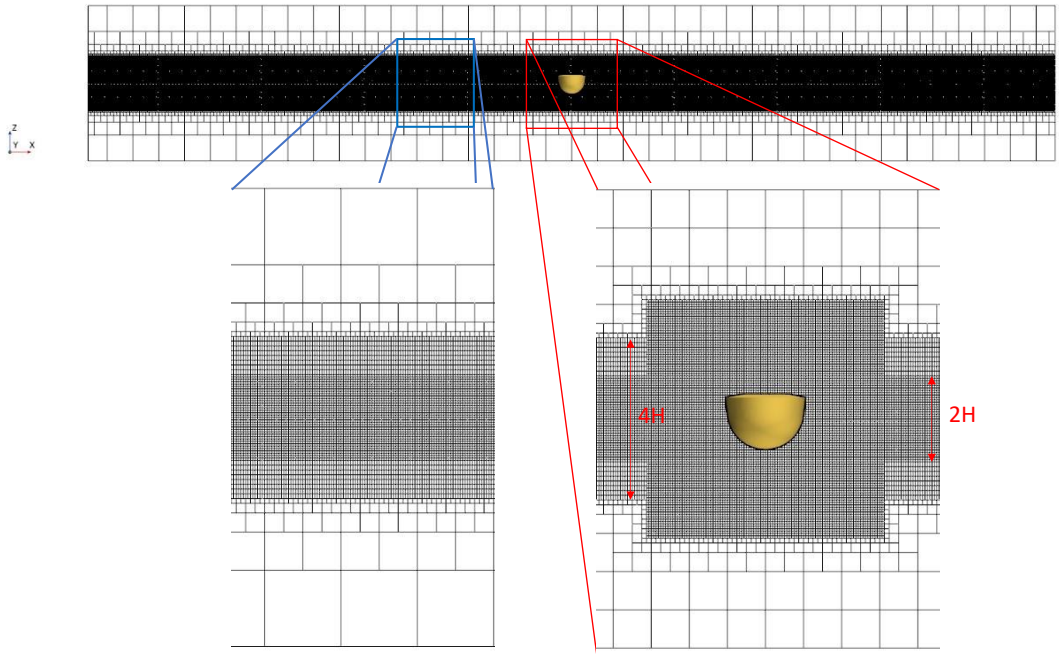

Figure 3.3 Cells around the free surface and the distribution of cells along the z-direction.

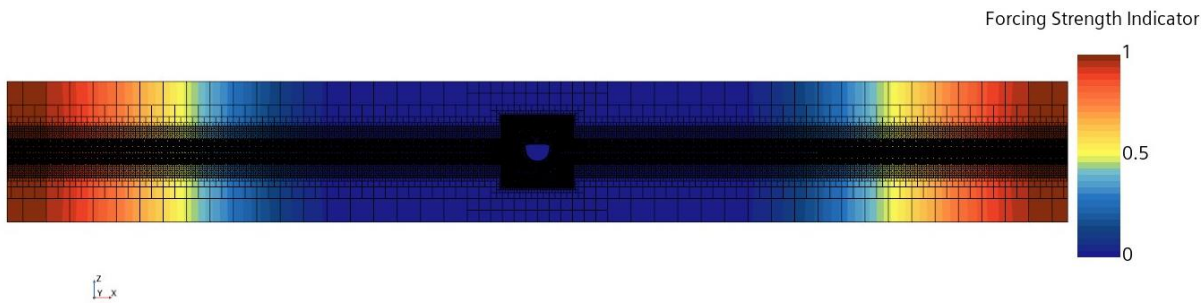

Figure 3.4 Distribution of forcing strength for wave forcing scheme in the computational domain for T=2.5s.

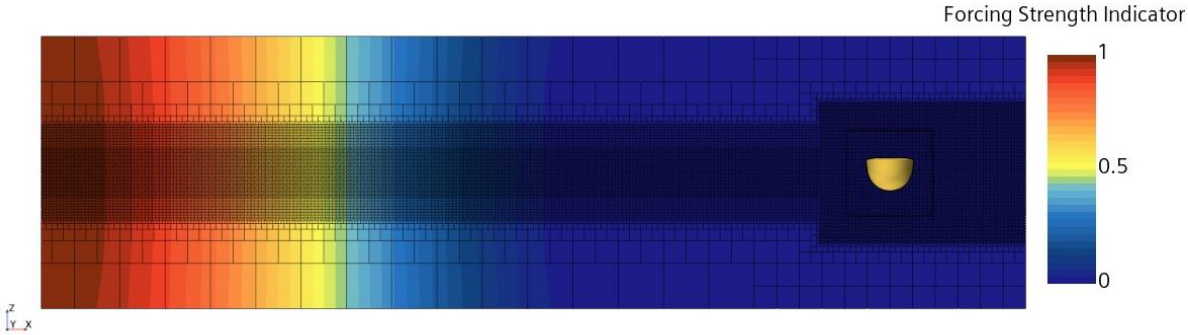

Figure 3.5 Distribution of forcing strength for wave forcing scheme in the simulation case with the vertical wall for T=1.6s.

Figure 3.4 illustrates the distribution of forcing strength for the wave forcing scheme within the computational domain, specifically for a wave period (T) of 2.5 seconds. The color-coded representation in the figure allows for a clear interpretation of the magnitude of forcing strength at different locations within the computational domain.

Figure 3.5 shows the distribution of forcing strength for the wave force scheme when a simulation case with the vertical wall. The boundary located in the x+ direction is subjected to a wall condition, and the WEC is positioned 3 metres away from this boundary. In this simulation case, the wave forcing scheme is applied to the inflow, and the thickness of the relaxation zone remains the same in the simulation case without the vertical wall. The length of the computational domain for the simulation case with the wall is 5λ. Similar to the simulation case without the wall, the same three types of refinement zones have been established. It is highlighted that the size of the third refinement zone has been extended to the vertical wall. This extension is aimed at accurately capturing the wave runup at the vertical wall and the standing waves generated between the wall and the buoy.

3.2.4 Numerical PTO model

In the study of Windt et al. (2020a), the focus is on implementing resistive control in the PTO model in order to match the numerical result against their experimental data. The PTO torque is defined by Equation (3.9),

$$\tau_{PTO} = B_{PTO}\omega_{WEC} + K_{PTO}\Theta_{WEC} \quad (3.9)$$

where B_{PTO} represents the angular damping constant, exerting a force opposite to the body's angular velocity (ω_{WEC}). This damping force is associated with a resistive or dissipative effect, and it is directly linked to the WEC capacity to harness wave energy. Meanwhile, K_{PTO} denotes the rotational spring stiffness, representing a reactive-force proportional to the rotational angle around a pivot point, typically negligible due to resistive control in the PTO system. Initially, an attempt was made to approximate PTO effects using an angular damping constant at the WEC's pivot point, applying the theoretical PTO torque (Zurkinden et al., 2014, Penalba et al., 2018). However, this simplified model fell short of accurately replicating the PTO system in the numerical simulation.

Consequently, as reported in the study by Windt et al. (2020), a more robust approach has been implemented. In this refined approach, the PTO force is now precisely applied to the WEC arm at the location of Point B. This adjustment aims to enhance the simulation's accuracy, ensuring a more accurate representation of the actual physical system dynamics. A linear spring-damper system is implemented for the numerical PTO model (See Equation (3.10)).

$$F_{PTO}(t) = -B_{num} \cdot V_{PTO}(t) - K_{num} \cdot S_c(t) \quad (3.10)$$

The overall strategy of the numerical PTO model in this study followed the model presented by Windt et al. (2020a). The PTO force is modelled as a linear spring-damper system, which is defined in Dynamic fluid body interaction (DFBI) solver via a Point C, fixed throughout the simulation, and a Point B, moving with the buoy of the WEC. The DFBI solver can calculate the hydrodynamic forces and moments acting on the rigid body and solve the governing equations of the rigid body motion to determine the next position of the rigid body for the next time step. It is highlighted that the same calibrated coefficients of damping and stiffness were used in this study, as in Windt et al. (2020a). Since resistive control is employed in the Wavestar device, only damping and no reactive force should be applied by the PTO. However, an equivalent linear damping coefficient cannot lead to the expected results of their numerical simulation during a validation process against their experimental data. Similarly, Coiro et al. (2016) mentioned a mismatch between numerical results based on CFD and experiment results even though an equivalent linear damping coefficient has been applied in their PTO system. From the experiments by Windt et al. (2020a), the inspection of the zero damping case revealed that a PTO force was still being applied. It is concluded that the delays of the controller and hardware between target and actual force, in the physical tank, cause the residual reactive power. Another possible cause can be friction in the mechanical part. To overcome the gap between numerical simulation and experimental measurements, the calibration of the PTO coefficients is required. The numerical PTO coefficients of B_{PTO} and

K_{PTO} can be achieved through a least square regression, with a detailed process available in the study of Windt et al. (2020a). The outcome of this process yields the following equations:

$$K_{num} = 184B_{PTO} - 4700 \tag{3.11}$$

$$B_{num} = 70B_{PTO} \tag{3.12}$$

In order to accurately calculate the PTO force, $V_{PTO}(t)$ and $S_c(t)$ must be determined precisely. Two straightforward methods are available for determining the velocity of PTO. The first method involves transforming the calculated angular velocity of the buoy, while the second method utilizes the rate of $S_c(t)$. In the case of the second method, to calculate the velocity of PTO, a continuous time series of $S_c(t)$ values is required, however, it yields a delay of one time-step. Although this approach may be simpler when the time step is very small, the first method is applied to mitigate potential errors associated with this delay. When the buoy of the WEC moves with a certain velocity, the angular velocity of the WEC can be described as in the following equation:

$$\omega_{WEC} = \frac{V_{\perp}}{r} \tag{3.13}$$

where $V_{\perp}$ is cross-radial speed and r is the length of a lever arm. All relevant parameters are depicted in Figure 3.6. As point B is moving along the WEC motion, the cross-radial speed of V_B at point B can be obtained by multiplying the distance between point A and point B and the angular velocity of the buoy (see Equation (3.14)).

$$V_B = \overline{AB}\omega_{WEC} \tag{3.14}$$

Point B, where the velocity of the PTO is implemented, follows the movement of the WEC. Consequently, the velocity of the PTO device varies in accordance with $\beta(t)$. The value of $\beta(t)$ is determined along with geometrical transformations through the following equation:

$$\beta(t) = \cos^{-1}\left(\frac{S_c^2(t) + c^2 - b^2}{2cS_c(t)}\right) \tag{3.15}$$

$$V_{PTO}(t) = V_B(t)\cos\left(\frac{\pi}{2} - \beta(t)\right) = V_B(t)\sin\beta(t) \tag{3.16}$$

Introducing a new local coordinate system with the x-axis aligned with segment AB and the origin at point B (See Figure 3.6(b)), this coordinate system follows the motion of the WEC. The PTO force acting at point B in this coordinate system is expressed as follows:

$$F_{PTO,x'} = F_{PTO} \cdot \cos\big(-\beta(t)\big) = F_{PTO} \cdot \cos\beta(t) \tag{3.17}$$

$$F_{PTO,z'} = F_{PTO} \cdot \sin\big(-\beta(t)\big) = -F_{PTO} \cdot \sin\beta(t) \tag{3.18}$$

In real-world applications, there are always some losses due to factors such as friction, heat, and other inefficiencies. Therefore, the actual generated power is usually less than the absorbed power. However, in this study, an ideal PTO model is employed, assuming a scenario without losses attributed to any type of friction. Therefore, the absorbed power (P_{abs}) and the generated power are exactly equal to each other and can be expressed as:

$$P_{abs}(t) = -V_{PTO}(t)F_{PTO}(t) \tag{3.19}$$

The available power of a wave may be expressed as follows.

$$P_{wave} = \frac{1}{8}\rho g H^2 c_g \tag{3.20}$$

where H is the wave height, c_g is the wave group velocity, ρ is the water density and g is the acceleration of gravity. The capture width ratio (CWR) is a non-dimensional performance ratio used to express the performance of a wave energy device. It is defined as the ratio of the absorbed power by the device (P_{abs}) to the available wave power to the device (P_{wave}) multiplied by the active width of the device ($width_{active}$) as shown in the following equation:

$$CWR = \frac{P_{abs}}{P_{wave} \cdot width_{active}} \tag{3.21}$$

This non-dimensional parameter allows for consistent comparison of performance across different devices with different scaling ratios, as only the wave parameters need to be adapted correspondingly to the scaling ratio and site. The term of $width_{active}$, as defined by (Pecher, 2012), corresponds to the width of all the components of the device that are actively involved in the primary conversion stage from wave energy to absorbed energy.

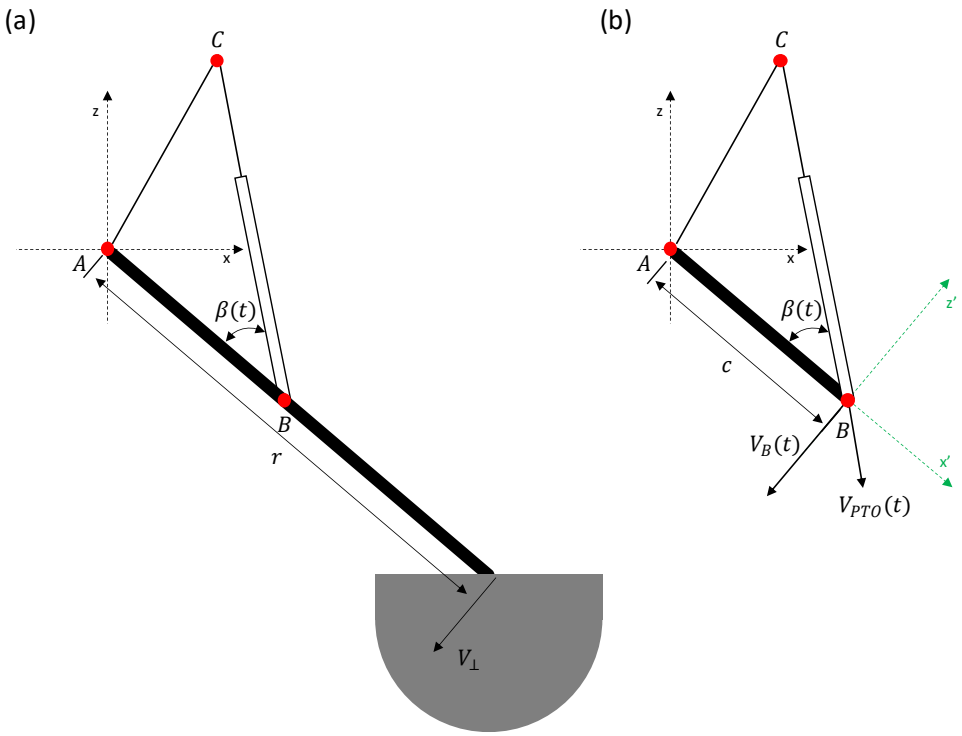

Figure 3.6 Definition of variables for the numerical PTO model.

3.2.5 Implementation of Latching control

The purpose of the latching control strategy is to improve the efficiency of WECs by ensuring that the velocity is in phase with the excitation force.

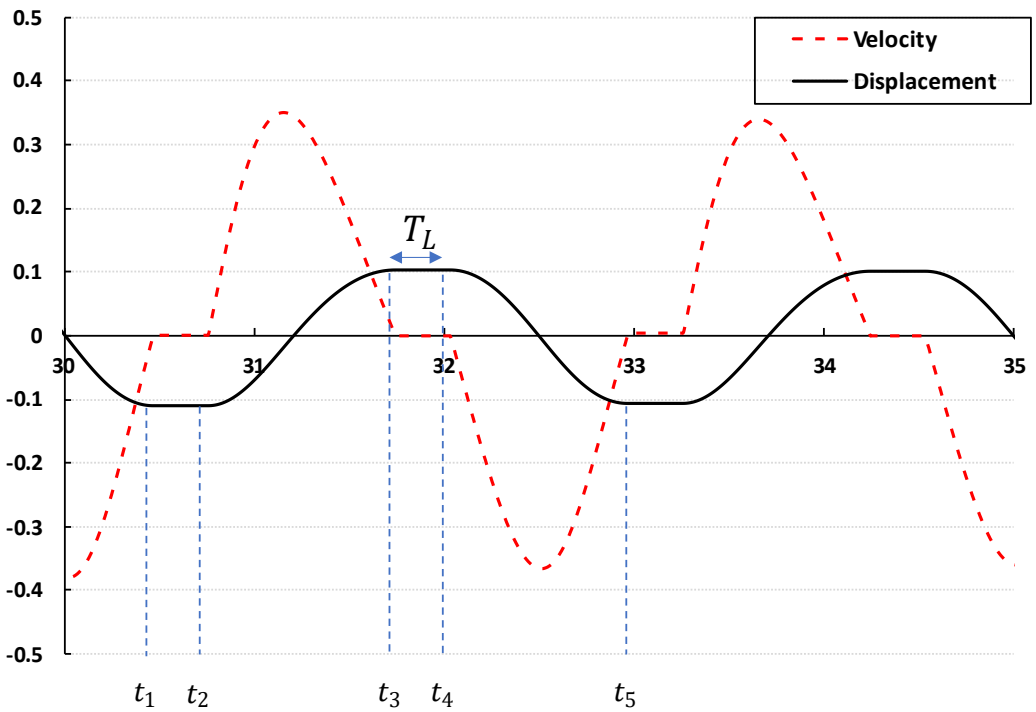

Figure 3.7 Operation of latching control in present numerical simulation. Latching instants when the velocity is zero: t_1, t_3 and t_5; latching duration: T_L; unlatching instants: t_2 and t_4

An example of operating latching control can be seen in Figure 3.7. The device is stalled at time t_1, t_3 and t_5 where the absolute value of displacement is maximised, in other words when its velocity vanishes, and is held for a latched duration $\mathrm{T_L}$. After the latched duration, the device is released at times t_2 and t_4. Ringwood and Butler (2004) have investigated the optimal latched duration for regular and monochromatic wave. When the wave period T_W exceeds the natural period of the device T_n, the optimal calculation for a constant latched duration is as follows:

$$T_L = \frac{t_5 - t_1}{2} - (t_5 - t_4) = \frac{T_W}{2} - \frac{T_n}{2} \tag{3.22}$$

When the wave period is shorter than the natural period of the device, an alternative latching control strategy can be considered to enhance the efficiency of a WEC system. This strategy includes options such as declutching (Babarit et al., 2009, Teillant et al., 2010), ramps with alternated maxima, and equal ending ramps (Babarit et al., 2004, Babarit and Clément, 2006). The natural period of the device T_n in Equation (3.22) does not account for the influence of damping on PTO.

Figure 3.8 illustrates the numerical latching control strategy through a logical flowchart. After the start of a simulation, the latching control does not execute until $t_{transition}$, which is approximately the time it takes for the buoy to reach a steady state. As mentioned earlier, the trigger of latching control occurs when the PTO velocity is zero. While it would be feasible with infinitely small-time steps, for discrete time steps, finding the point where PTO velocity is exactly zero is challenging. Therefore, the time after the measured PTO velocity zero-crossing is defined as the starting point of the latching control. From this time onwards, the latching control becomes active, and $t_{release}$ is established. Afterwards, if the latching control is already active, its continuation or termination is determined by comparing the current simulation time with $t_{release}$.

Various methods exist for implementing a numerical model for the latching control strategy, but from a practical and efficient standpoint, two approaches seem prominent. The first method, often utilized in studies based on potential flow theory, involves the calculation of the damping by utilizing a function known as a damping profile, which represents the variation of the damping over time (Teillant et al., 2010, Babarit et al., 2009). Alternatively, there is a method involving imposing constraints on the motion of the body to achieve effects similar to latching control (Giorgi and Ringwood, 2016). When using a damping profile, employing CFD becomes somewhat challenging as the damping coefficients need to be increased significantly in a short time for latching control to be active. Therefore, in this study, when latching control is active, constraints are applied to the body motion to observe its effects.

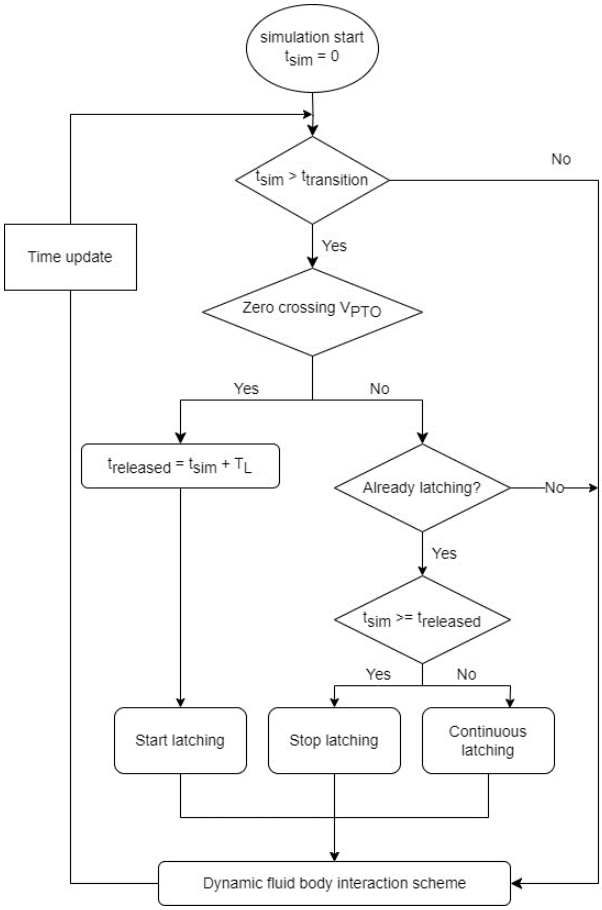

Figure 3.8 Latching control strategy. Simulation time: t_{sim}; transition time: $t_{transition}$; latched duration: T_L; released instant: $t_{released}$

4 CFD simulation for WEC integrated with a vertical wall

This chapter focuses on a numerical study using CFD to explore how hydrodynamic performance of a WEC is influenced at different distances from a vertical wall under various wave conditions.

4.1 Goal and scope

The primary goal of this chapter is to investigate the effects of a vertical wall according to the distance between the wall and the WEC, providing a comprehensive understanding of the hydrodynamic performance of the WEC in various wave conditions.

The numerical simulations were performed at eight different wave conditions, as listed in Table 4.1. The wave period of the investigated wave conditions ranged from 1.4 seconds to 2.8 seconds. The wave height and water depth in the numerical simulations were 0.25m and 3.0m, respectively. Figure 4.1 shows the validity of wave theories (Le Méhauté, 2013) according to wave period, wave height and water depth. The investigated wave conditions which are indicated as red dots in Figure 4.1 ranged from Stokes 2nd order to Stokes 3rd order. The numerical simulations also considered different distances between the wall and the WEC, ranging from 1.0 meters to 3.0 meters.

Experimental results of wave case 1 and 8 are presented in (Ransley et al., 2017). Additionally, a set of relevant experiments is discussed in (Jakobsen et al., 2016).

Table 4.1 Wave cases to which the simulation for WEC integrated with a vertical wall is applied.

Case number C	Wave period [s] T	Wavelength [m] λ	Wave height [m] H	Wave steepness H/λ
1	1.4	3.06	0.25	0.082
2	1.6	4.00	0.25	0.063
3	1.8	5.06	0.25	0.049
4	2.0	6.25	0.25	0.040
5	2.2	7.56	0.25	0.033
6	2.4	8.99	0.25	0.028
7	2.6	10.55	0.25	0.024
8	2.8	12.24	0.25	0.020

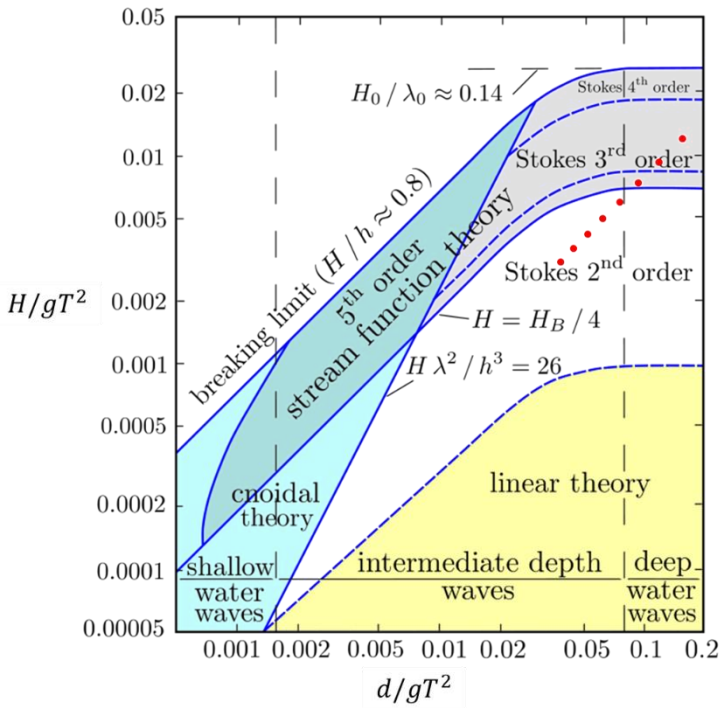

Figure 4.1 Validity fields of wave theories according to Le Méhauté (2013). Red dots represent the wave conditions in this study.

4.2 Numerical modelling

The numerical setup for the current CFD simulations was based on that presented in Section 3.2.

A minimum of 12 cells per wave height and 100 cells per wavelength near the still water line were generated to simulate the regular waves in the background region, in order to prevent numerical dissipation (Figure 4.2). The resolution of cells that provides the finest level of detail covers both one wave height below and one wave height above the still water line. The initialised solution at the beginning of the numerical simulation can be seen in Figure 4.3.

Figure 4.4 illustrates the computational domain utilized in numerical simulations incorporating a vertical wall. To avoid wave reflections caused by the vertical wall and to ensure that waves do not reach the inflow boundary, it is essential to increase the distance between the inflow boundary and the body compared to scenarios without a vertical wall in the computational domain. The most refined meshes are strategically positioned to encompass the region situated between the body and the vertical wall, as this arrangement is expected to yield the desired wave run-up effect encompassing both diffracted and reflected waves.

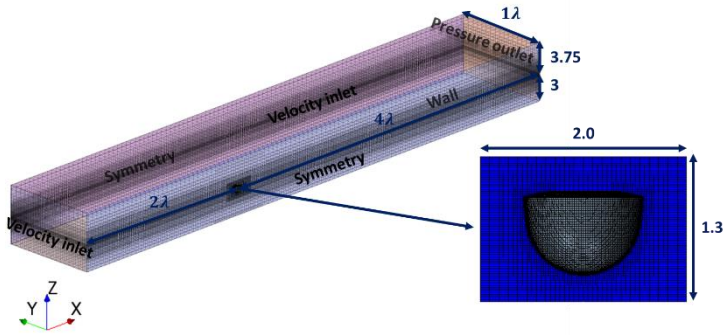

Figure 4.2 The computational domain with imposed boundary conditions for numerical simulation cases without a vertical wall (The units in the figure are metres).

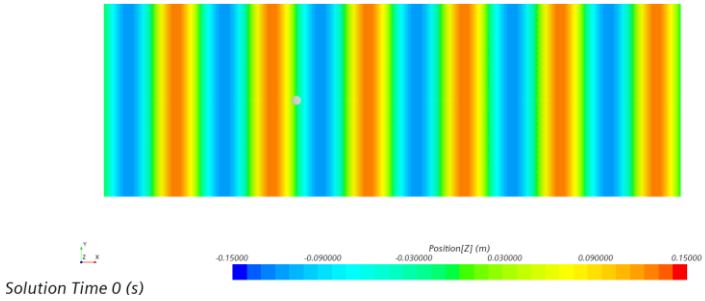

Figure 4.3 Initialised computational domain before a numerical simulation starts.

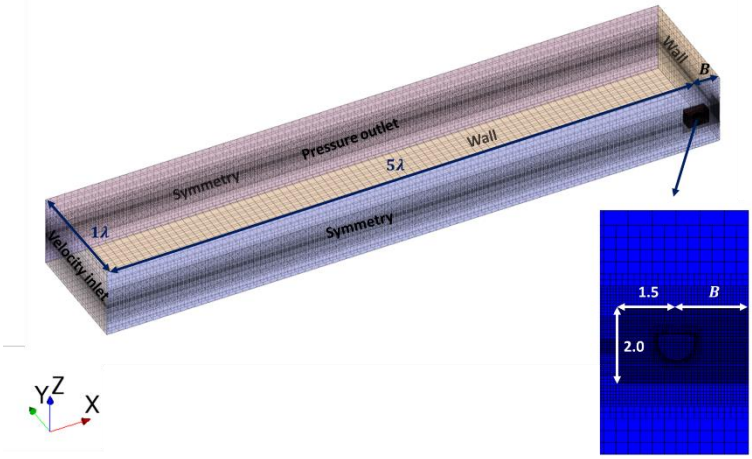

Figure 4.4 The computational domain with imposed boundary conditions for vertical wall cases (The units on the figure are metres).

4.3 Stationary wave

Stationary wave, also known as standing wave, is the combination of two identical waves moving in opposite directions. This phenomenon can be seen as a wave superposition and can

be used to maximise the displacement of a buoy in wave height direction. In a vertical wall simulation case, a reflected wave due to the presence of the vertical wall and an incident wave at the inlet yield a stationary wave around the position of the buoy. Figure 4.5 shows the brief view of the buoy and the vertical wall and the origin of the coordinates is in the centre of the buoy in longitudinal direction at still water level. A wave travelling along the +x direction is reflected at the vertical wall. An incident wave and a reflected wave can be described as a function of position x and t in Equation (4.1) and (4.2), respectively.

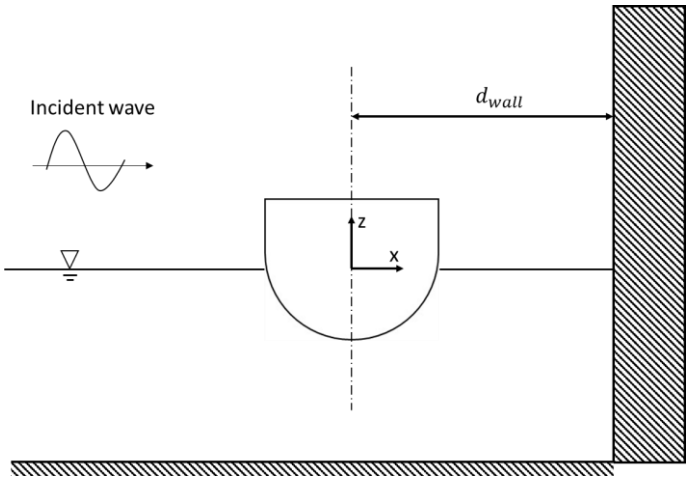

Figure 4.5 Schematic view of a buoy and a vertical wall.

$$z_I(x,t) = z_{max}\sin(kx - \omega t) \tag{4.1}$$

$$z_R(x,t) = z_{max}\sin(kx + \omega t) \tag{4.2}$$

where z_{max} is the amplitude of an incident wave, k is a wave number ($2\pi/\lambda$), and ω is a wave frequency ($2\pi/T$). To consider a distance to the vertical wall, an unknown quantity (C) is added in Equation (4.2) to consider a reflection wave with a different phase due to distance to the vertical wall and a variant reflected equation is derived as Equation (4.3).

$$z_R(x,t) = z_{\max}\sin(kx + \omega t + C) \tag{4.3}$$

$$z(x,t) = z_I(x,t) + z_R(x,t) = z_{\max}\sin(kx - \omega t) + z_{\max}\sin(kx + \omega t + C) \tag{4.4}$$

$$z(x,t) = 2z_{\max}\sin\left(kx + \frac{C}{2}\right)\cos\left(\omega t + \frac{C}{2}\right) \tag{4.5}$$

Using the trigonometric sum-to-product identity, the sum of the incident and reflected wave can be derived as Equation (4.5). At $x = d_{wall}$ where the intersection point between SWL and the vertical wall, since the maximised wave height is captured, the absolute value of sine

term in Equation (4.5) should be maximised. Consequently, the equation (4.9) is derived when $x = 0$ where the buoy is located in a computational domain.

$$kd_{wall} + \frac{\mathrm{C}}{2} = \frac{n\pi}{2} \ (n = 1, 3, 5, \ldots) \ at \ x = d_{wall} \tag{4.6}$$

$$\mathrm{C} = n\pi - 2kd_{wall} \tag{4.7}$$

$$z(x,t) = 2z_{\max} \sin\left(kx + \frac{n\pi}{2} - kd_{wall}\right) \cos\left(\omega t + \frac{n\pi}{2} - kd_{wall}\right) \tag{4.8}$$

$$z(t)_{\mathrm{x=0}} = 2z_{\max} \sin\left(\frac{n\pi}{2} - kd_{wall}\right) \cos\left(\omega t + \frac{n\pi}{2} - kd_{wall}\right) \tag{4.9}$$

$$\mathrm{f(k, d_{wall})} = \left|2z_{\max} \sin\left(\frac{n\pi}{2} - kd_{wall}\right)\right| \tag{4.10}$$

In accordance with Equation (4.9), the analytical solution of the wave height at $x = 0$ depending on the wave period and the distance to the vertical wall (B) can be obtained. The amplitude of Equation (4.9) means the maximum amplitude of the stationary wave equation, consequently, the analytical solution of the stationary waves considering incident and reflected waves due to the vertical wall is obtained (Equation (4.10)).

4.4 Results

4.4.1 Verification and comparison with experimental data

In this verification study, the influence of changing the number of iterations on the numerical simulations was deemed to be negligible since the number of iterations was over 10. A verification study was carried out for the lower frequency wave case (Case 8) for grid-space and time-step uncertainties.

The procedure for estimation of discretisation error followed the Grid Convergent Index (GCI) approach of Celik et al. (2008) based on the Richardson extrapolation method (Richardson, 1911). The definition and symbol of parameters in the verification study are the same as those used in Celik et al. (2008).

Let N and h denote the total number of grids for a numerical simulation and representative grid size, respectively, which gives the following expression:

$$h = \left[\frac{1}{N}\sum_{i=1}^{N}(\Delta V_i)\right]^{1/3} \tag{4.11}$$

$$r_{21} = h_2/h_1 \tag{4.12}$$

$$r_{32} = h_3/h_2 \tag{4.13}$$

where ΔV_i is the volume of the ith cell used for the simulation and r is the grid refinement factor defined by the ratio of the representative grid sizes. For a time-step convergence study, the definition of the time refinement factor can be given by $\gamma_{21} = \Delta t_2/\Delta t_1$ and $\gamma_{32} = \Delta t_3/\Delta t_2$. It is desirable that the refinement factor (r) be greater than 1.3 based on experience and not formal derivation according to Celik et al. (2008).

The apparent order of the method, p, can be solved using fixed-point iteration:

$$p = \frac{1}{\ln r_{21}} |\ln|\varepsilon_{32}/\varepsilon_{21}| + q(p)| \tag{4.14}$$

$$q(p) = \ln\left(\frac{r_{21}^p - s}{r_{32}^p - s}\right) \tag{4.15}$$

$$s = 1 \cdot sgn(\frac{\varepsilon_{32}}{\varepsilon_{21}}) \tag{4.16}$$

where $\varepsilon_{32} = \phi_3 - \phi_2$, $\varepsilon_{21} = \phi_2 - \phi_1$, and ϕ_k denotes the solution on the kth grid. Note that $q(p) = 0$ for $r = const$. The extrapolated values are calculated from

$$\phi_{ext}^{21} = (r_{21}^p \phi_1 - \phi_2)/(r_{21}^p - 1) \tag{4.17}$$

The approximate relative error and extrapolated relative error, respectively, are described:

$$e_a^{21} = \left|\frac{\phi_1 - \phi_2}{\phi_1}\right| \tag{4.18}$$

$$e_{ext}^{21} = \left|\frac{\phi_{ext}^{21} - \phi_1}{\phi_{ext}^{21}}\right| \tag{4.19}$$

Finally, the fine-grid convergence index is calculated:

$$GCI_{\text{fine}}^{21} = \frac{1.25 e_a^{21}}{r_{21}^p - 1} \tag{4.20}$$

4.4.1.1 Grid-spacing convergence study

Case 8 (T=2.8s, H=0.25m) was selected for the grid-spacing convergence study. The grid-spacing convergence study was performed with three different grids, which are regarded as fine, medium, and coarse grids corresponding to grid numbers of 2,266,456 cells, 824,604 cells, and 297,978 cells, respectively. Table 4.2 shows the calculation procedure for the three different grids. As can be seen from the results of Table 4.2, the numerical uncertainty of 0.6% was estimated for the displacement of the cylinder.

Table 4.2 Calculation of the discretization error for the grid-spacing convergence study

	Value
N_1	2,266,456
N_2	824,604
N_3	297,978
r_{21}	1.401
r_{32}	1.404
ϕ_1	0.0715
ϕ_2	0.0717
ϕ_3	0.0720
p	1.21
ϕ_{ext}^{21}	0.0712
e_a^{21}	0.2%
e_{ext}^{21}	0.5%
GCI_{fine}^{21}	0.6%

4.4.1.2 Time-step convergence study

The same wave case (Case 8) of the grid-spacing convergence study was selected for the time-step convergence study. Three different time-steps were employed with a uniform refinement ratio (r) of $\sqrt{2}$, starting from $\Delta t = T/512$. Table 4.3 shows the result of the calculation of the temporal discretization error. As can be seen from the result listed in Table 4.3, similar to the grid-spacing convergence study, small levels of uncertainty were estimated for the displacement of the cylinder.

Table 4.3 Calculation of the discretization error for time-step convergence study.

	Value
Δt_1	0.0055
Δt_2	0.0077
Δt_3	0.0109
r_{21}	1.4142
r_{32}	1.4142
ϕ_1	0.0715
ϕ_2	0.0717
ϕ_3	0.0719
p	1.72
ϕ_{ext}^{21}	0.0714

e_a^{21}	0.2%
e_{ext}^{21}	0.2%
GCI_{fine}^{21}	0.3%

4.4.1.3 Comparisons with experimental data

The experimental data of the displacement of the cylinder from Ransley et al. (2017) were compared with the result of the present numerical simulations. All of the experimental data from Ransley et al. (2017) have been performed in the Ocean Basin at Plymouth University's Coastal, Ocean And Sediment Transport (COAST) laboratory. Unidirectional NewWaves are physically generated by 24 flap-type wave paddles at one end of wave tank (32m long and 15.5 wide, 3m depth).

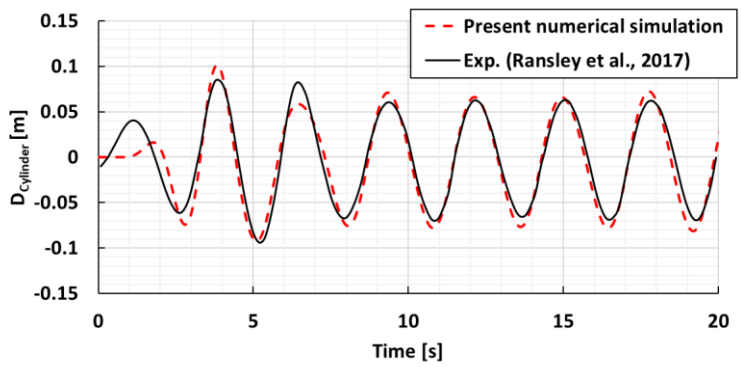

Figure 4.6 Comparison of the displacement of the cylinder between the simulated and experimental data (Ransley et al., 2017), T=2.8s, H=0.25m.

Figure 4.6 shows the comparison of the displacement of the cylinder between the present numerical simulation and experimental data from Ransley et al. (2017). The target wave is the same as Wave Case 8 (wave period of 2.8 seconds and wave height of 0.25m). It should be noted that a positive displacement corresponds to a lifting of the buoy. The solid black line indicates the experimental data of the displacement of the cylinder (Ransley et al., 2017) and the red dotted line indicates the present numerical simulation. Relatively large fluctuations with slightly different phase at the beginning of the numerical simulation are shown in Figure 4.6. It is likely that the initial conditions with a fully developed wave field in the numerical model shown in Figure 4.3 would affect the large amplitude of motions. However, after around 10 seconds the numerical WEC device begins to oscillate with the same frequency as that found in their experiments and the displacement of the cylinder for the numerical model shows good agreement with that of their experimental data.

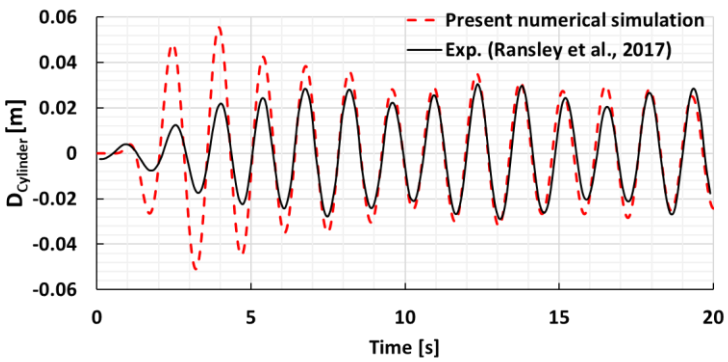

Figure 4.7 Comparison of the displacement of the cylinder between numerical simulation and experimental data (Ransley et al., 2017), T=1.4s, H=0.15m.

Figure 4.7 shows the comparison of the displacement of the cylinder between the numerical simulation and experimental data (Ransley et al., 2017) when the target wave period is 1.4 seconds and the wave height is 0.15m. Before comparing the experimental results with the present CFD results, Ransley et al. (2017) mentioned that the low-frequency beating of the displacement was captured due to the reflected waves in the physical basin at short wavelength. The low-frequency beating of the displacement indicates that the amplitude of the displacement of the cylinder keeps increasing and decreasing. This beating behaviour was not captured at long wavelength. Similarly, the present numerical results show the same pattern of the low-frequency beating but the amount of the beating is relatively lower than that of their experimental data. It can be found that the low-frequency beating would be related to not only the reflected waves due to a wall in the physical basin but also a diffraction wave around the WEC device. Due to the initial conditions of the computational domain the large amplitude motions of the WEC device are at the beginning phase are observed. Overall good agreement between the present numerical and experimental (Ransley et al., 2017) results is observed.

4.4.2 Cases without vertical wall

Numerical simulations without a vertical wall were investigated according to wave period. From the results of the numerical simulations without the vertical wall, the characteristic of the target WEC according to wave period can be obtained such as a natural frequency and a response to an incident wave of the target WEC. For the analysis of the numerical simulations, the displacement of the cylinder, considering eight consecutive wave periods has been recorded and the recorded displacements have been analysed by fast Fourier transform (FFT) method in order to obtain the first harmonic components. The first harmonic components were normalised by the amplitude of the incident waves and presented in Figure 4.8. In addition, for comparison with the results of the experiment data (Ransley et al., 2017), the results were included in Figure 4.8. It can be found that the results of the numerical simulations are slightly overpredicted. Figure 4.9 shows the time history of the displacements of the cylinder for wave case 4 (T=2.0s) for 30 seconds, which showed the largest WEC motions amongst the selected wave cases. After approximately five seconds the

displacements of the cylinder in the numerical simulations begin to oscillate stably, and the data during the eight consecutive wave periods were selected for the FFT analysis. The largest motion is captured in wave case 4 (T=2.0s) and a similar natural period of the WEC was captured in their previous experimental research (Jakobsen et al., 2016).

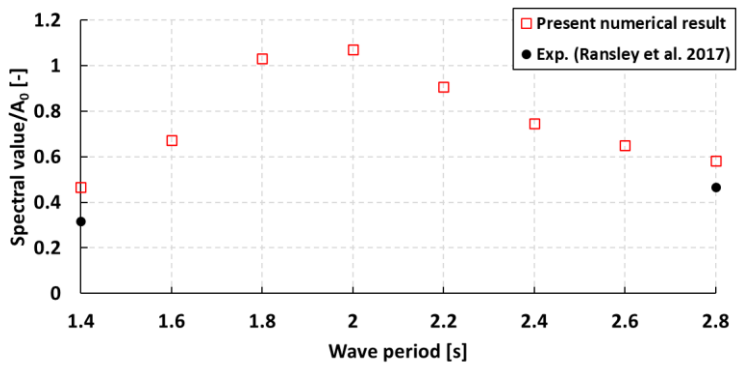

Figure 4.8 Numerical results of FFT analysis of displacement of cylinder normalised by amplitude of the incident wave and comparison result with experimental data.

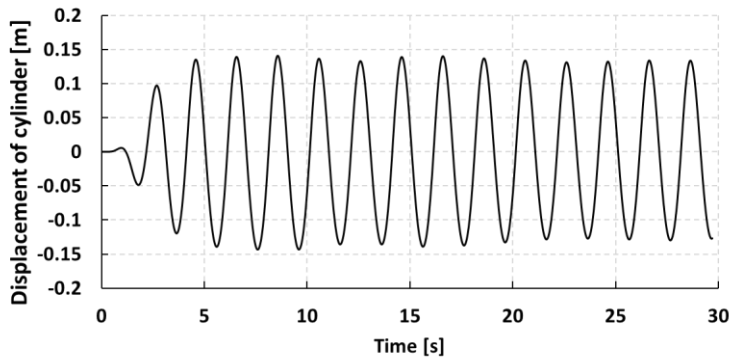

Figure 4.9 Numerical displacement of cylinder data for wave case 4 without the vertical wall.

Figure 4.10 shows the view of the free surface around the buoy in Case 4. It should be noted that the maximum displacement of the cylinder is observed in Case 4 amongst the selected wave cases in Section 4.1.

Figure 4.10 and Figure 4.11 show the free surface variations around the buoy for wave case 4 without vertical wall, respectively, at 4 instants along a period; (a) zero-up crossing of the displacement of the cylinder, (b) the maximum lift of the WEC device, (c) zero-down crossing of the displacement of the cylinder and (d) the minimum lift of the WEC device. The absolute value of the maximum and minimum range in a contour in Figure 4.10 is the wave height of the incident wave. A wave crest propagating toward the WEC device can be seen in Figure 4.10 (a) and this leads to the maximum lift of the WEC device and then the generated and distorted waves due to the motion of the WEC device are observed in Figure 4.10 (c) and (d).

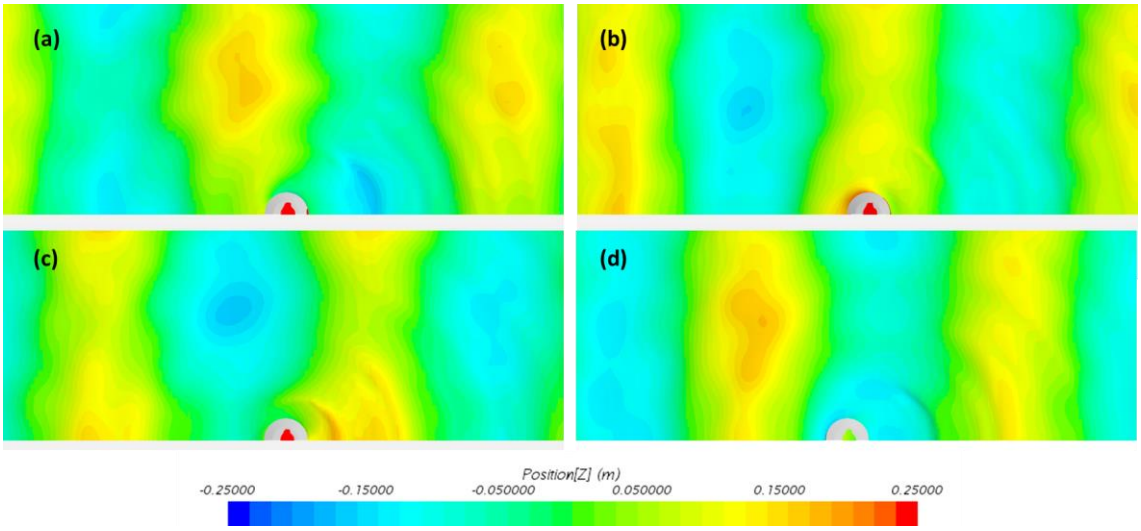

Figure 4.10 Variation of the free surface around the buoy at 4 instants along a period, top view. (Wave case 4: T=2.0s, H=0.25m)

Figure 4.11 shows the variation of the free surface on the symmetry plane in the computational domain. There are only 2 contour colours, which red colour indicates the water and blue indicates the air, to clearly identify the free surface. Figure 4.12 shows the clear views of the free surface near the buoy and on the wall of the buoy. During the propagation of the incident wave, the change in the wetted surface of the WEC device according to the position of the WEC device can be seen.

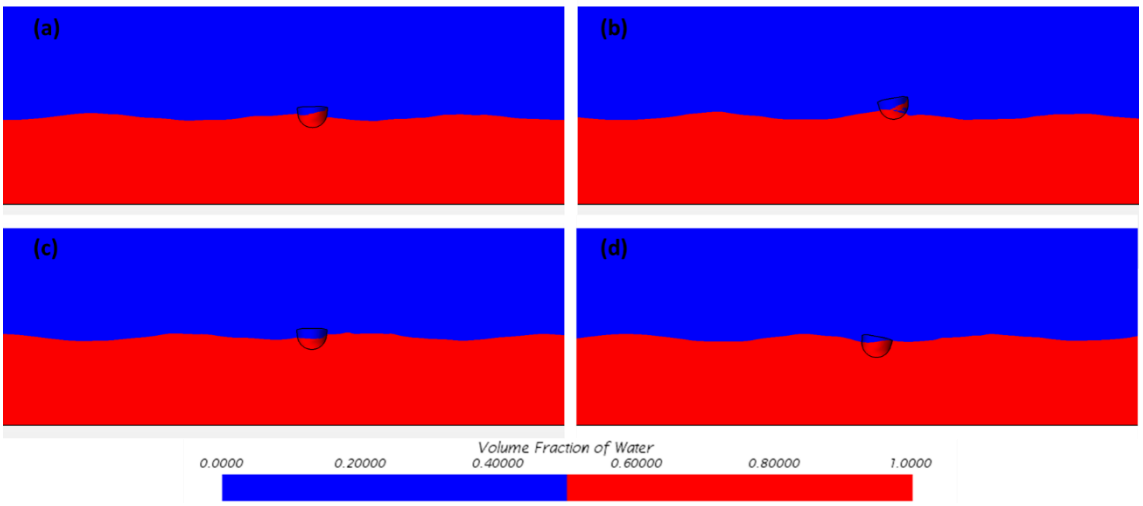

Figure 4.11 Variation of the free surface around the buoy at 4 instants along a period, side view. (Wave case 4: T=2.0s, H=0.25m)

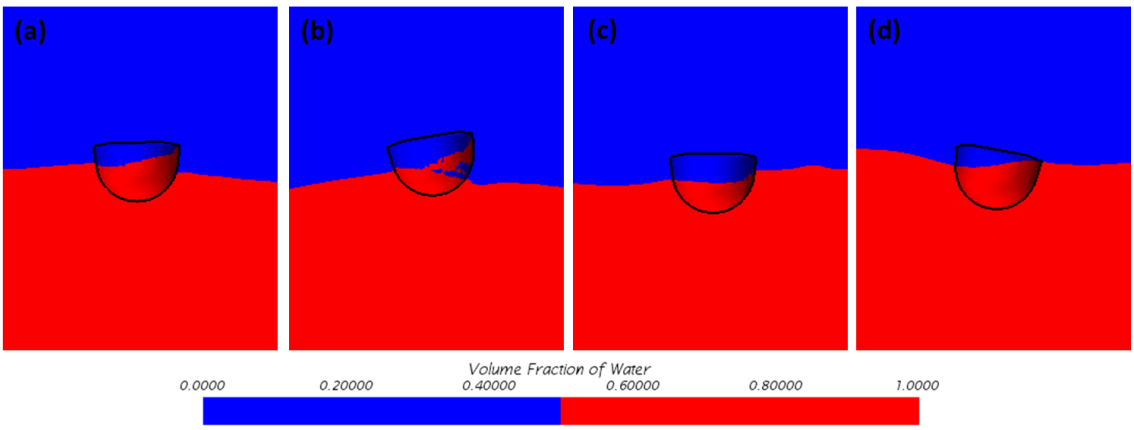

Figure 4.12 Variation of the free surface near the buoy and on the wall of the buoy at 4 instants along a period, side view. (Wave case 4: T=2.0s, H=0.25m)

4.4.3 Cases with vertical wall

A simplified analytical stationary wave equation was derived and compared to this study's CFD results. The free surface elevations from the analytical solution and the present numerical model are compared directly at three different wave probes (x=-1.917m, x=0m, and x=0.75m). The positive x-direction is towards the vertical wall in the computational domain and x=0 means the location where the buoy is located. For the comparison between the analytical solution and the present numerical model, the buoy was not installed to capture the stationary waves due to the vertical wall.

Solid lines and dotted lines in Figure 4.13 indicate the analytical solutions derived from Equation (4.8) and the numerical results, respectively. Different colours represent the location of the probe. For the case of d_{wall}=1.0m which is the shortest distance to the vertical wall, overall good agreement between the analytical solution of Equation (4.8) and the numerical data is observed except at x=-1.917m, as shown in Figure 4.13 (a). A possible reason for the mismatch between the analytical and numerical results is that the amplitude of the free surface elevation is relatively too small to capture the superposed wave in the numerical simulation. Another possible reason can be that the analytical solution does not consider the higher-order wave equations.

For the cases of d_{wall}=1.5m and d_{wall}=2.0m (Figure 4.13 (b), (c)), the free surface elevation results obtained from the analytical solution and the numerical data match reasonably well, whereas slightly over- and under-prediction of the wave crests and troughs at x=-1.917m are found, respectively. For the case of d_{wall}=3.0m which is the longest distance to the vertical wall in this study, a similar trend regarding the mismatch is found at x=-0.75m which shows the small amplitude of free surface elevation (Figure 4.13 (d)). As a result of the comparison in Figure 13, it was thought that the analytical solution is reasonably accurate to calculate the amplitude of the free surface elevation around the location where the WEC buoy is located with respect to the vertical wall.

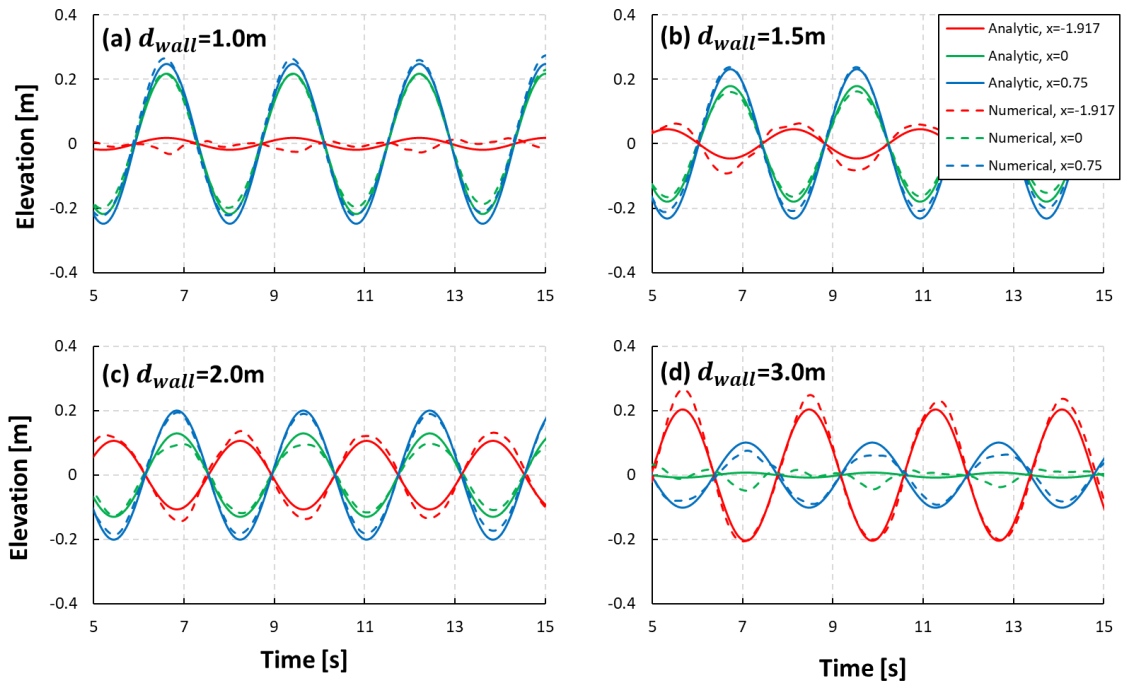

Figure 4.13 Numerical data and analytical solution for wave case 8 at three different wave probes.

In this section, the results obtained by numerical simulations with a vertical wall, and the analytical solutions discussed in Section 4.3 were compared. The first harmonic components by the FFT analysis method were obtained, considering six consecutive wave periods of numerical simulations with the vertical wall. In this case, it is highlighted that a relatively small amount of consecutive wave periods should be considered due to the possibility of a strongly distorted incident waves. Even though the wave forcing scheme works well near the inflow boundary, the possibility of a numerical error occurring cannot be ignored. To find a correlation between the motions of WEC and of stationary waves, the first harmonic components of the motions have been compared with the amplitude of the stationary wave.

Solid lines shown in Figure 4.14 represent the result of the analytical solution based on Equation (4.10) and the circle symbol means the first harmonic component by FFT analysis. Table 4.4 shows the result of numerical solutions and comparisons, where B represents the distance to the vertical wall. For $B = 1.0m$, which is the shortest distance to the vertical wall, the amplitude of the stationary wave by analytical solution decreases rapidly, reaches the lowest point approximately at $T = 1.6s$, and then increases gradually. In the case of numerical results for $B = 1.0m$, the smallest value of the first harmonic component is captured at $T = 2.0s$. As the wave period increased from $T = 2.0s$, the first harmonic component also tended to increase until T=1.8s and then to decrease. In terms of the lowest point, it can be seen that the results of the analytical solution of Equation (4.10) and CFD do not match, and this phenomenon can be seen, in a similar fashion, at different distances to the vertical wall. One possible explanation can be that the analytical solution in this study considered only the reflected waves from the vertical wall and the incident waves towards the vertical wall, in order to simplify the equation, whilst the numerical model included

diffracted, radiated, and reflected waves with all non-linearities. Despite the ignorance of the complicated waves between the WEC buoy and the vertical wall in the analytical solution, the result of the analytical solution appears similar to the trend of the numerical results.

For $B = 1.5m$ and $B = 2.0m$, the amplitude of the analytical solution and the first harmonic component of the numerical result according to wave period can be seen in Figure 4.14 (b) and (c), respectively. As in the case of $B = 1.0m$, the results of analytical solutions and numerical results show a similar trend in terms of the position of the lowest point. At T=1.4s for $B = 1.5m$, the analytical solution shows the maximum stationary wave amplitude, and it is likely that the stationary waves caused the increase of the motion of the WEC device. Even in the short-wave period regime (i.e., T=1.4s), which showed the lowest motion response in the numerical case without the vertical wall, the result of the first harmonic component increased by 41%.

For $B = 3.0m$, which is the longest distance to the vertical wall, the amplitude of the analytical solutions and the first harmonic component of the numerical results as function of the wave period can be seen in Figure 4.14 (d). Except for the short-wave period regime, overall good agreement between the results obtained from the analytical and numerical solutions is observed. In the case of $B = 3.0m$, the maximum stationary wave amplitude is distributed near the natural frequency of the WEC device and was expected to have a significant effect on the motion of the WEC device. As a result, the WEC device showed the highest response at T=2s (near the natural frequency of the WEC device), which is 17% higher than that of the numerical case without the vertical wall.

Generally, when comparing the results obtained from the analytical and numerical solutions it can be seen that a tendency for the solutions is to gradually increase after the lowest point of the motion response, but the biggest difference between the two results is the position where the lowest point is recorded. As the trend of the numerical results is also comparable to those obtained from the analytical solutions, it seems clear that the stationary waves have an effect on the results, but it is considered that accurate estimation is difficult since the analytical solutions are composed of two wave components only. Nevertheless, the correlation between the vertical wall distance and the motion of the WEC device could be estimated even with a simple analytical solution of Equation (4.10). It was confirmed that this can be suggested as a way to amplify the floating body motion as function of the position of the vertical wall.

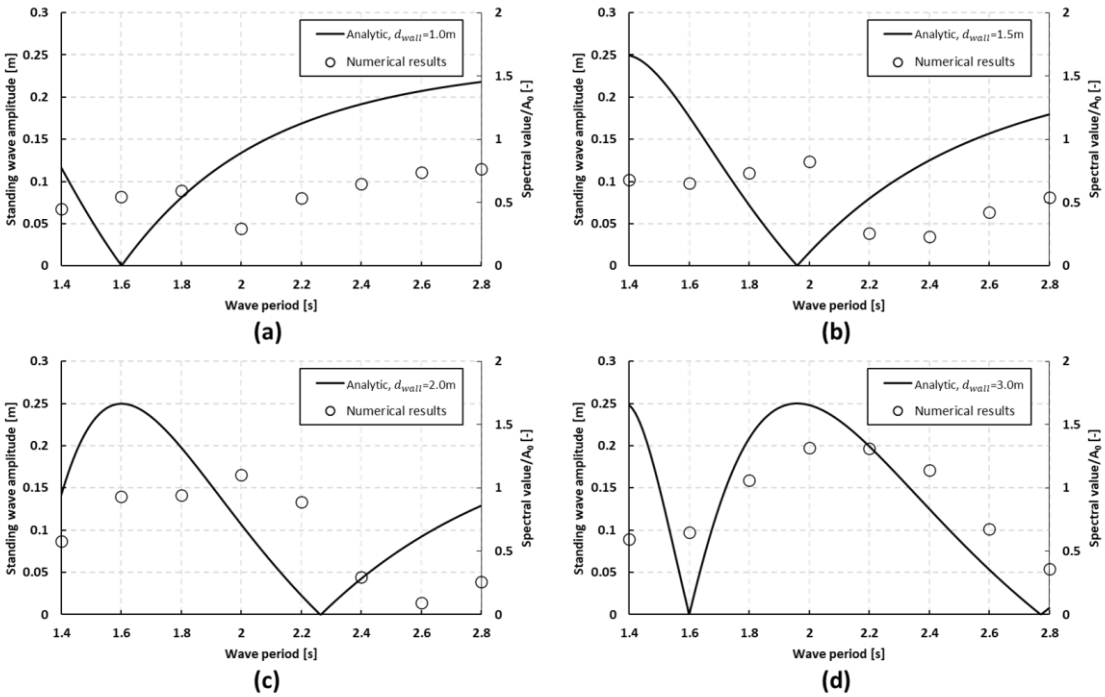

Figure 4.14 Comparison between stationary wave amplitude and normalised spectral value of displacement of the cylinder according to distance to the vertical wall (d_{wall}).

Table 4.4 Numerical result of the first harmonic component of cylinder displacement according to distance to vertical wall (d_{wall})

Wave case, C	First harmonic component			
	d_{wall}=1.0m	d_{wall}=1.5m	d_{wall}=2.0m	d_{wall}=3.0m
1	0.0566	0.0851	0.0723	0.0741
2	0.0683	0.0817	0.1163	0.0814
3	0.0741	0.0920	0.1179	0.1325
4	0.0367	0.1033	0.1377	0.1648
5	0.0667	0.0324	0.1113	0.1641
6	0.0811	0.0290	0.0371	0.1424
7	0.0923	0.0532	0.0119	0.0845
8	0.0956	0.0678	0.0324	0.0449

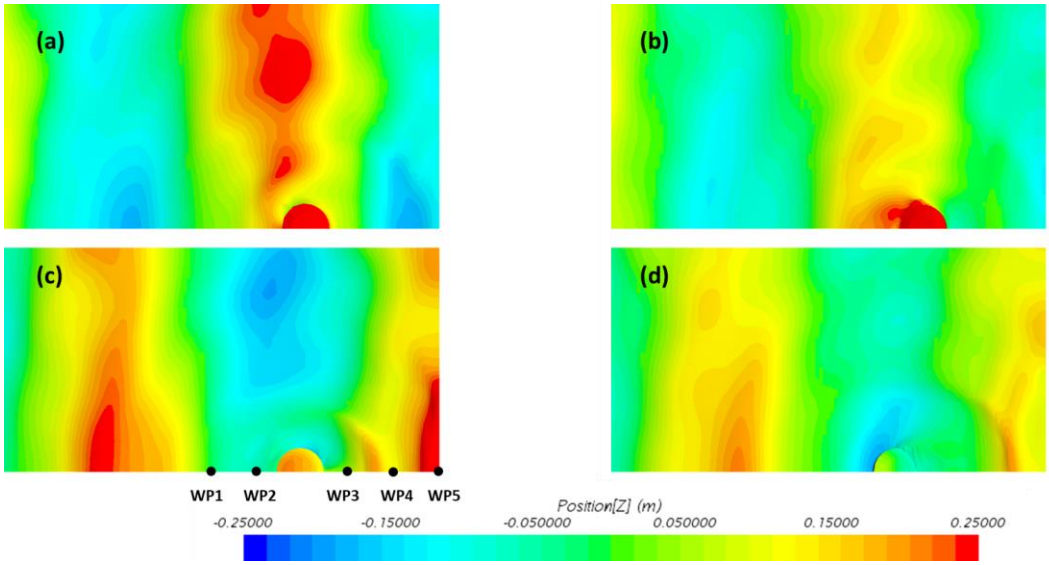

Figure 4.15 Variation of the free surface around the buoy with vertical wall, top view. And the location of wave probes (Wave case 4: T=2.0s, H=0.25m and d_{wall}= 3.0m)

Table 4.5 Location of wave probes (WP)

Probe	WP1	WP2	WP3	WP4	WP5
x-coordinate [m]	-2.0	-1.0	1.0	2.0	3.0

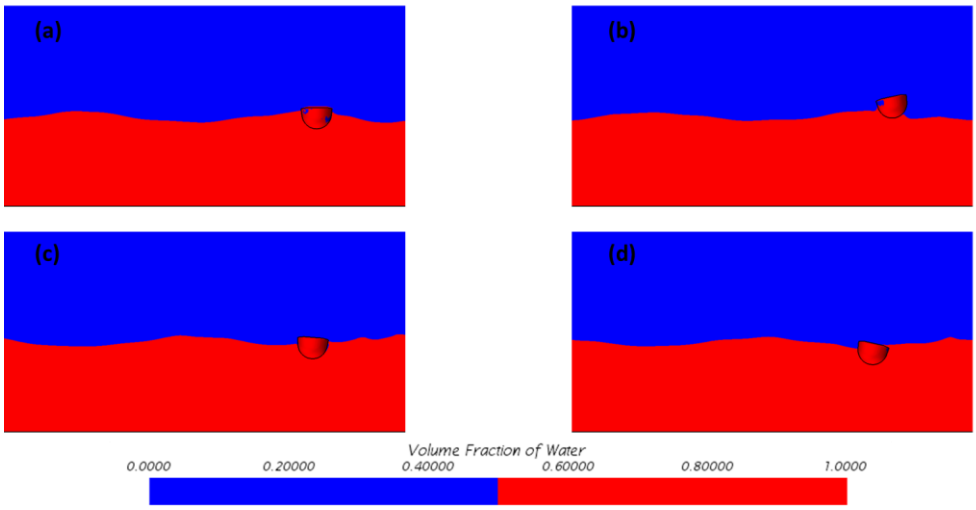

Figure 4.16 Variation of the free surface around the buoy with vertical wall, side view. (Wave case 4: T=2.0s, H=0.25m and d_{wall}= 3.0m)

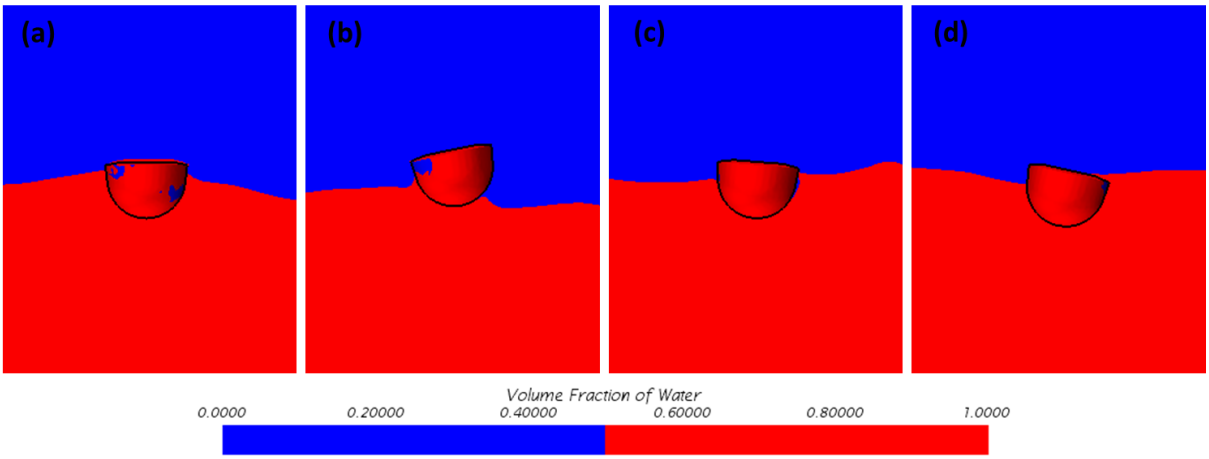

Figure 4.17 Variation of the free surface near the buoy and on the wall of the buoy with vertical wall, side view. (Wave case 4: T=2.0s, H=0.25m and d_{wall}= 3.0m)

Figure 4.15 and Figure 4.16 show the time instants of (a) zero-up crossing of the displacement of the cylinder, (b) the maximum lift of the WEC device, (c) zero-down crossing of the displacement of the cylinder and (d) the minimum lift of the WEC device when the wave period and wave height are 2.0 seconds and 0.25m, respectively, and the distance to the vertical wall (d_{wall}) is 3.0m. Figure 4.17 shows the clear views of the free surface near the buoy and on the wall of the buoy with the vertical wall. The right side of each figure is the location of the vertical wall. More complicated wave distribution and higher wave amplitudes are captured in the numerical case with the vertical wall compared to those without the vertical wall. It is noted that the WEC buoy has been covered with water due to the green water effect, the water elevation on the position of the WEC buoy has also increased and decreased. The wave run-up effect is also observed near the vertical wall, where the free surface elevation reached two times of incident wave height.

Figure 4.18 shows the change in the wave elevation for Wave case 4 (T=2.0s and H=0.25m) as function of each wave probe position. The probes of WP1 and WP2 are located upstream of the WEC buoy, and the rest of the probes (WP3-5) are downstream of the WEC buoy. It should be noted that WP4 and WP5 are installed where the vertical wall is located. The x-coordinate of the wave probe location can be seen in Table 4.5 and Figure 4.15. The records of WP1 and WP2 in Figure 4.18 show the change of the free surface in front of the WEC buoy. It can be seen that the changes of the free surface are more complicated when there is a vertical wall than when there is no vertical wall. This is because the reflected waves generated from the vertical wall make the waves around the WEC buoy more disturbed. The records of WP3 in Figure 4.18 show the change of the free surface in the downstream of the WEC buoy by 1.0m. In this case, in the wake region behind the object, a clearer change in waves can be seen depending on the presence of the vertical wall. When there is the vertical wall, the waves that may occur between the WEC buoy and the vertical wall are as follows. They occur as disturbed incident waves, radiation waves generated by the motion of the WEC buoy, reflected waves of the disturbed incident waves from the vertical wall and reflected waves of the radiation waves. Due to these wave components, it is believed that more

complicated waves are measured in the wave region behind the WEC buoy. The final two records (WP4 and WP5) show the changes of the free surface at the vertical wall when the distance is d_{wall}=2.0m and d_{wall}=3.0m. The biggest difference is that the wave height has increased significantly due to the vertical wall. The wave height of the free surface in the vertical wall is about twice the wave height of the incident wave.

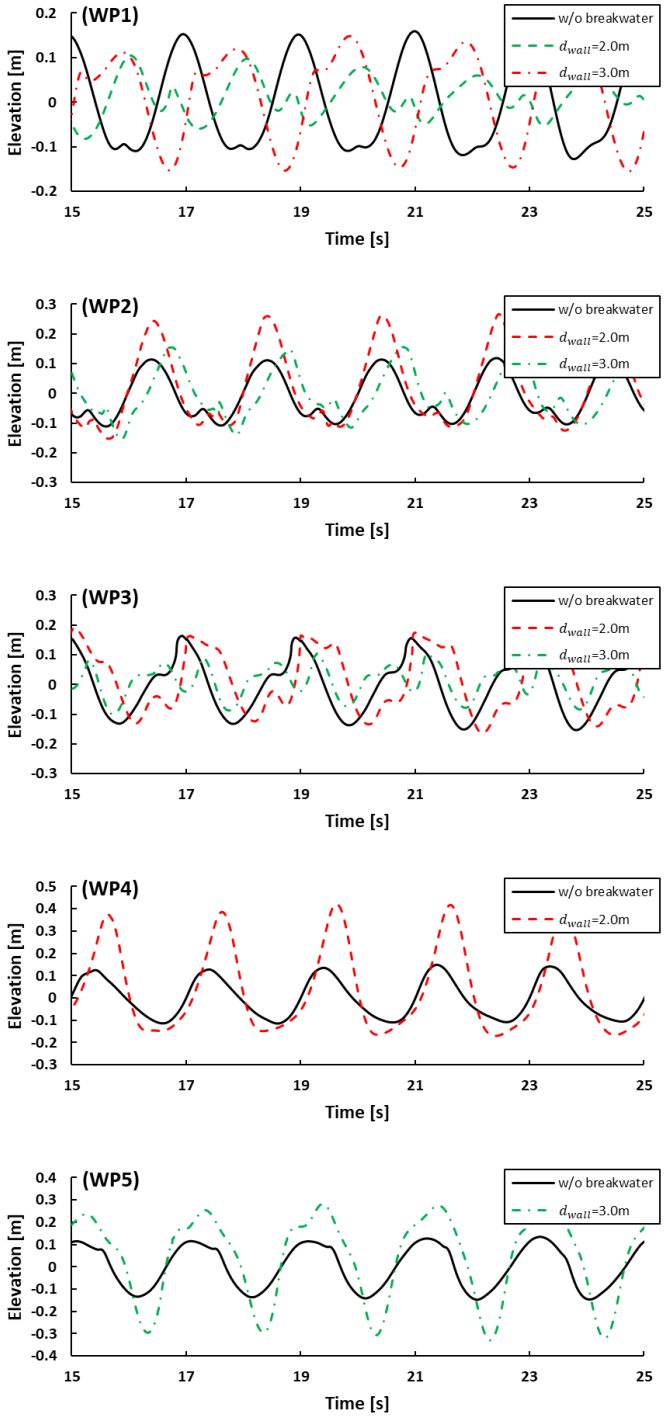

Figure 4.18 Comparison of wave elevations for Wave case 4. Black solid line means the result of cases without the vertical wall, Red dashed line means the result of cases with vertical wall (d_{wall}=2.0m) and Green dashed dot line represents the result of cases with vertical wall (d_{wall}=3.0m).

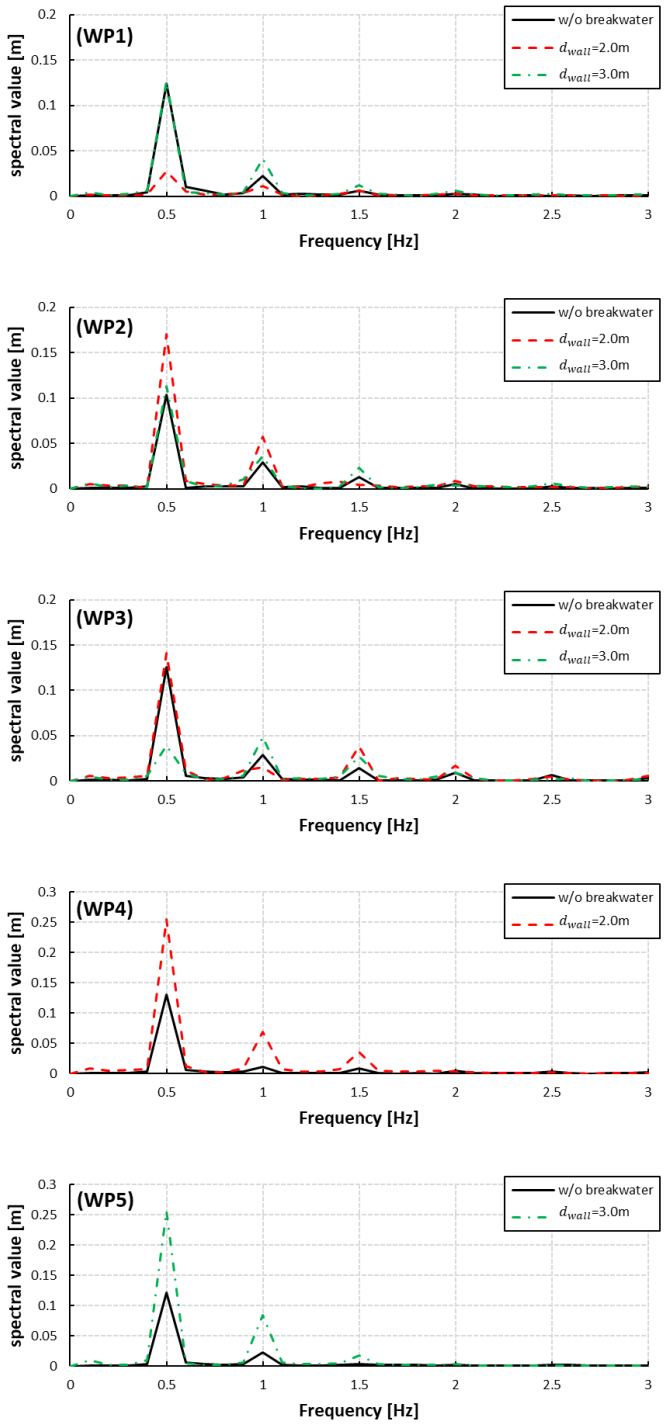

Figure 4.19 Comparison of FFT results for Wave case 4 by wave probe. Black solid line means the result of cases without vertical wall, Red dashed line means the result of cases with vertical wall (d_{wall}=2.0m) and Green dashed dot line represents the result of cases with vertical wall (d_{wall}=3.0m).

In order to further investigate higher harmonic contributions around the WEC buoy, Figure 4.19 shows a FFT analysis of the free surface records. At all wave probes, it was possible to confirm the first, second and third harmonic components. In particular, in WP3 corresponding to the wake region, higher harmonic components than the third harmonic can be observed.

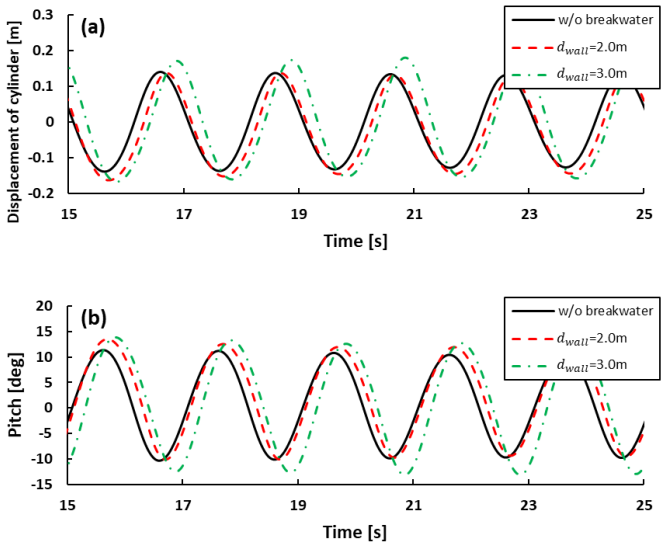

Figure 4.20 Comparison of motion of WEC according to the presence of vertical wall. (a): Displacement of cylinder, (b): pitch. Black solid line means the result of cases without vertical wall, Red dashed line means the result of cases with vertical wall (d_{wall}=2.0m) and Green dashed dot line represents the result of cases with vertical wall (d_{wall}=3.0m).

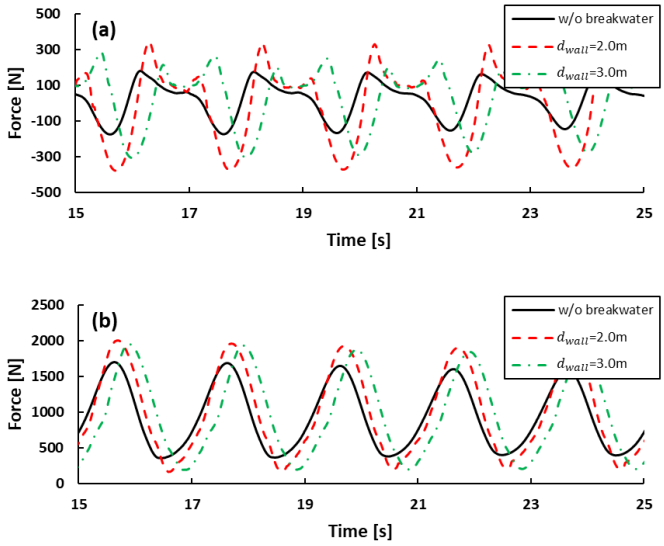

Figure 4.21 Comparison of horizontal and vertical forces. (a): horizontal force, (b): vertical force. Black solid line means the result of cases without vertical wall, Red dashed line means the result of cases with vertical wall (d_{wall}=2.0m) and green dashed dot line represents the result of cases with vertical wall (d_{wall}=3.0m).

Figure 4.20 and Figure 4.21 show the motions and forces on the WEC buoy, respectively. Each plot includes the result of the case without the vertical wall when d_{wall}=2.0m (the distance to the vertical wall is 2.0m) and d_{wall}=3.0m. The positive of displacement of cylinder represents the lifting of the WEC buoy above the still water level. The horizontal force graph shows a relatively larger difference between the present numerical results. It is interesting to note that the horizontal force on the WEC buoy follows a similar trend of the displacement of the cylinder. As a result, the combination of vertical and horizontal forces must have an effect on the displacements of the cylinder, but it can be assumed that the

influence of the vertical forces on the motions of WEC buoy is greater than that of the horizontal forces.

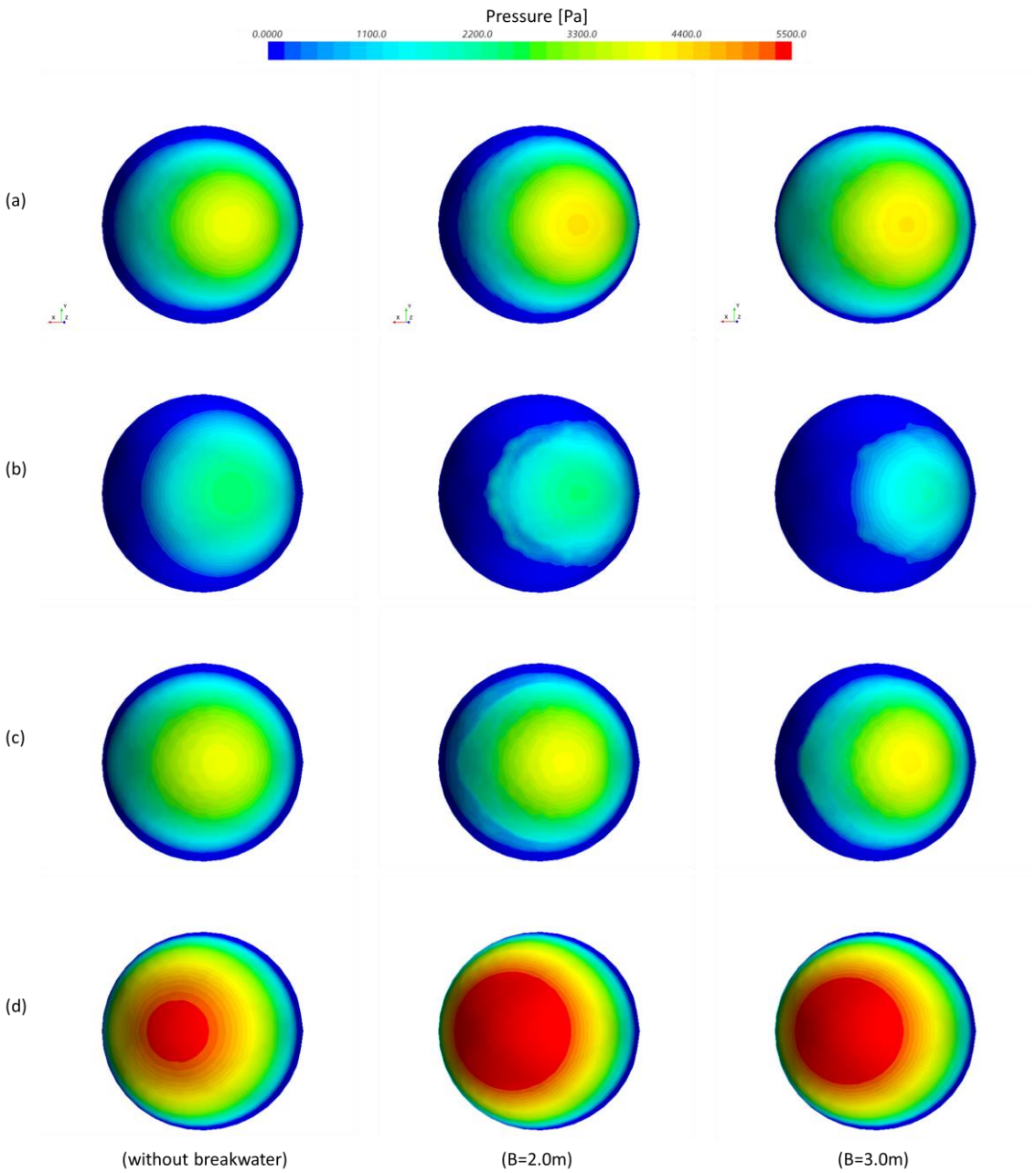

Figure 4.22 Pressure distribution of the WEC buoy for Wave case 4 (T=2.0s and H=0.25m). Case without vertical wall (the first column), case when d_{wall}=2.0m (the second column) and case when d_{wall}=3.0m (the third column). (a): zero-up crossing, (b): maximum lift, (c): zero-down crossing, (d): minimum lift.

Figure 4.22 shows the pressure distributions on the bottom of the WEC buoy. Each scene in Figure 4.22 shows the time instants of (a) zero-up crossing of the displacement of the cylinder, (b) the maximum lift of the WEC buoy, (c) zero-down crossing of the displacement of the cylinder and (d) the minimum lift of the WEC buoy when wave case is 4 (T=2.0s and H=0.25m) and distance to the vertical wall is 2.0m (d_{wall}=2.0m). There are significant differences in the pressure distribution at time instants of (b) and (d). When the WEC buoy

reaches the maximum lift point, the shape of pressure distributions for d_{wall}=2.0m and d_{wall}=3.0m is more complicated than that of the case without the vertical wall. The reason for this is thought to be that the location of the WEC buoy (e.g. displacement of the cylinder) and the waves around the WEC buoy have become more disturbed. Depending on how high the WEC buoy rises, the wetted surface area should change, and the pressure distribution may change accordingly. Similarly, when the WEC buoy is down to its minimum lift point, it can be confirmed that greater pressure is generated because the movement increases in the presence of a vertical wall.

4.5 Concluding Remarks

The chapter presented here outline the comparison of the experimental data (Ransley et al., 2017) with numerical results and the verification of the accuracy of the numerical model. The investigation aimed to comprehend the hydrodynamic performance concerning the distance between the vertical wall and the WEC device. Four distinct distances to the vertical wall were established, and the ensuing results were compared.

To analyse the stationary waves in the presence of the vertical wall, an analytical solution, considering only the incident and reflected waves, was developed. The maximum wave height derived from the analytical solution was compared with that obtained from the numerical calculations through FFT analysis to discern the influence of the vertical wall on the motions of the WEC body.

The result of the comparison with published experimental data demonstrated a good agreement between the numerical model and the published experimental data (Ransley et al., 2017) for two different wave period cases. Building on the numerical model, the motion responses of the pivoted WEC body as function of the distance from the vertical wall were investigated. The numerical model effectively captured the variations in the motion responses by accounting for the impact of the stationary wave emanating from the vertical wall.

The analytical solutions enabled the prediction of stationary waves around the vertical wall and their influence on the WEC device, corroborated by the results of numerical simulations. The motion responses to waves increased by 41% when the wave period was 1.4 seconds compared to no vertical wall, and by 17% when the wave period approached the resonance period of 2.0 seconds. Despite the simplified assumptions of the analytical solution, it was evident that the amplitude of the stationary wave affected the motion of the WEC body within the vertical wall. This insight aids in optimizing the WEC device position with respect to the vertical wall.

Notwithstanding the impact of the stationary waves in front of the vertical wall, waves induced by the buoy's movement exert a substantial influence on the hydrodynamic performance of the WEC. By changing distance between the vertical wall to the buoy, hydrodynamic performance of the integrated vertical wall-WEC system according to wave condition has been achieved.

5 CFD simulation for WEC integrated with a vertical wall and latching control

This chapter aims to devise a method to maximize power extraction from a WEC by leveraging latching control to enhance the motion of the system and capitalizing on the stationary wave effects generated from a vertical wall. Using CFD techniques, the research presents the proposed methodology through comparison with experimental results (Windt et al., 2020a) that include an existing PTO system. The investigation involves CFD simulations to assess how the presence of a vertical wall, variations in the damping coefficient of the PTO, and the implementation of latching control influence the performance of the WEC. By systematically analysing these factors, the study aims to provide insights into how power extraction efficiency can be maximized under different conditions. This research contributes to the understanding of WEC dynamics and lays the groundwork for optimizing the design and operation of wave energy conversion systems.

5.1 Goal and scope

The primary goal of this chapter is to investigate the effect of PTO damping coefficients and the influence of latching control on the Wavestar-like WEC, providing a comprehensive understanding of the performance of the WEC in various wave conditions.

The numerical simulations were performed at 10 different wave conditions as detailed in Table 5.1, featuring varying wave periods ranging from 1.4 to 2.8 seconds. For the case study for this research, wave height was 0.25 meters, and the water depth was maintained at 3.0 meters. The distance between the WEC and the vertical wall is fixed as 3.0 meters. To gain comprehensive insights into the influence of PTO damping coefficients on the performance of the WEC, this study delves into an examination of four distinct damping values ($B_{exp} = 25, 50, 100, 200\ Nms$).

Table 5.1 Wave conditions, the wave condition used for the comparison with experimental data (Windt et al., 2020a) was marked in bold.

Wave case number C	Wave period [s] T	Wave frequency[rad] ω	Wavelength [m] λ	Wave height [m] H
1	**1.4**	**4.49**	**2.19**	**0.10**
2	1.4	4.49	2.19	0.25
3	1.6	3.93	2.50	0.25
4	1.8	3.49	2.81	0.25
5	1.9	3.31	2.97	0.25
6	2.0	3.14	3.12	0.25
7	2.2	2.86	3.43	0.25
8	2.5	2.51	3.90	0.25
9	2.8	2.24	4.37	0.25

5.2 Results

5.2.1 Verification

A verification study similarly to that detailed in Section 4.4.1 is carried out. Although this study focused on a different aspect and did not consider a PTO system. Current study introduces numerical modelling of the PTO system, necessitating the comparison with published experimental data by Windt et al. (2020a) of the present CFD model against experimental results. This experiment by Windt et al. (2020a) was carried out at the COAST Ocean Wave Basin at Plymouth University in November 2013. The COAST Ocean Wave Basin is a 35m by 15m wave and current basin with a water depth of 3m with the adjustable floor. The hydraulic PTO system is actively engaged with the WEC device.

Comparisons were made with experimental and numerical results from other studies which include experiments with a hydraulic Power Take-Off (PTO) (Windt et al., 2020a), numerical studies using the CFD-based OpenFOAM (Windt et al., 2020a), as well as the Boundary Element Method (BEM)-based ANSYS/AQWA software (Ghafari et al., 2021).

The comparisons were carried out under identical wave conditions, specifically with a wave period of 1.4 seconds and a wave height of 0.1 m. Three different cases were considered for comparisons, which correspond to PTO damping values of 50, 100, and 200Nms. Figure 5.1 illustrates the cylinder displacement for the case with PTO damping set to 50 Nms. Here, Experiment and Numerical 1 are the results given in (Windt et al., 2020a) and Numerical 2 are the results given in (Ghafari et al., 2021). Overall, the CFD results show good agreement with experimental measurements, accurately capturing both peak and trough well.

In Figure 5.2, the cylinder displacement is presented for the case with PTO damping set to 100 Nms. It is observed that the amplitude is slightly smaller compared to the case with PTO damping set to 50 Nms. Consequently, the CFD results show a close match to the experimental data, while the numerical simulations based on the Boundary Element Method (BEM) predicts lower values. For the case with PTO damping set to 200 Nms, the displacement shows the smallest amplitude, and the pattern is similar to the case with PTO damping set to 100 Nms.

Quantitative comparisons were made by recording the peaks and troughs over five cycles, calculating the average amplitude for each case. The results of these amplitude values are presented in Table 5.2. Overall, the CFD results consistently show a good correlation with the experimental data.

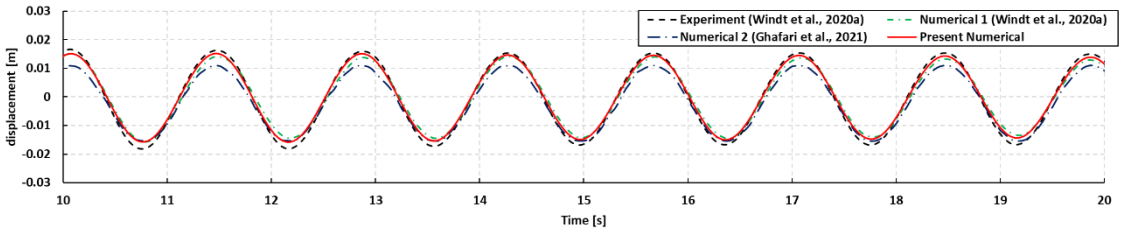

Figure 5.1 Comparison of cylinder displacements ($B_{PTO} = 50Nms$).

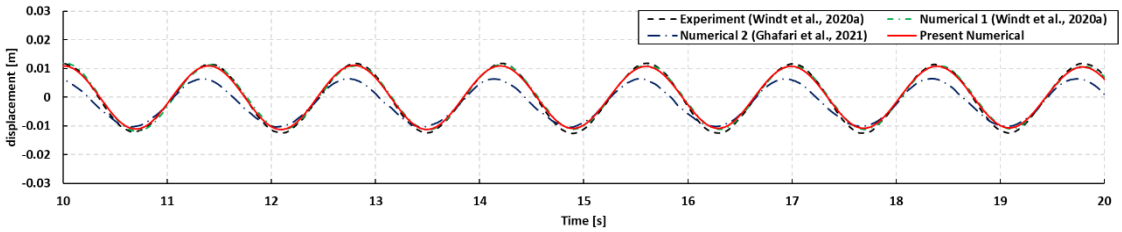

Figure 5.2 Comparison of cylinder displacements ($B_{PTO} = 100Nms$).

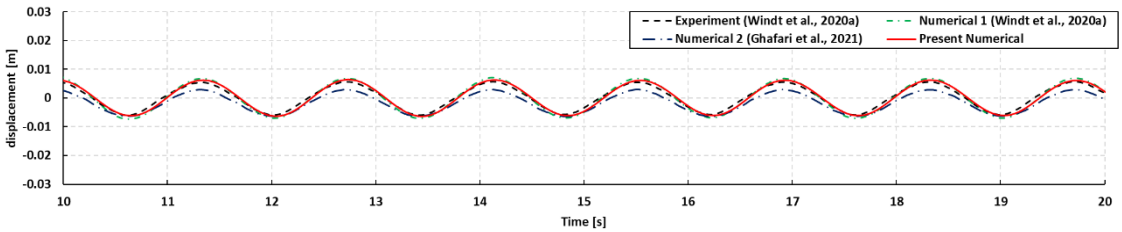

Figure 5.3 Comparison of cylinder displacements ($B_{PTO} = 200Nms$).

Table 5.2 Comparison of amplitude values for cylinder displacement, PTO velocity and PTO force between reference and present simulation.

Wave case	Wave period T [s]	Wave height H [m]	PTO damping B_{PTO} [Nms]	Experiment (Windt et al., 2020a)	Numerical 1 (Windt et al., 2020a)	Numerical 2 (Ghafari et al., 2021)	Present
1	1.4	0.1	50	0.034	0.029	0.026	0.031
			100	0.024	0.023	0.017	0.022
			200	0.011	0.013	0.009	0.012

5.2.1.1 Grid-spacing convergence study

A mesh convergence study was carried out, focusing on the mesh size relative to both wave height and wavelength under selected wave conditions. Notably, our wave conditions range from 1.4 to 2.8 seconds, twice the difference between the shortest and longest wave conditions. This approach was adopted to avoid employing a fixed mesh size, which could result in an excessive number of mesh elements. The determination of mesh size per wavelength and per wave height is crucial for enhancing the precision and efficiency of the computational model. For a mesh convergence study, the longest wave period in this research was selected and investigated. The minimum mesh size for z-direction is defined by the number of cells per wave height (CPH). Three mesh resolutions were investigated, where the

number of CPH was doubled between each mesh configuration, with the number of CPH of 6, 8.5, and 12, respectively. For the number of cells per wavelength (CPL), there are two conditions to determine. Firstly, CPL must always be 100 or higher. Secondly, the number of mesh for the x-direction is determined to be a multiple of 2^n (n is a positive integer) of the number of mesh for the z-direction. Figure 5.4 illustrates the cylinder displacement according to the mesh resolution. For the crest of the displacement, very little difference was observed between the three meshes, however, the result of the coarse mesh shows a slight difference at troughs from the other two meshes, which are in good agreement with each other.

Consequently, the fine mesh, with 12 CPH, is used for all case study simulations. The total number of cells used ranges from 3.3 to 5.0 million cells, depending on the wave period. The determination of this cell count range is managed by the specific conditions of CPL according to wave period.

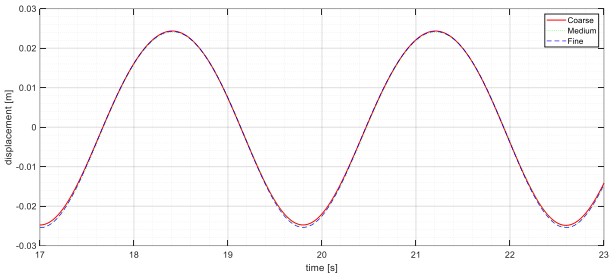

Figure 5.4 Displacement variation for increasing mesh refinement.

5.2.1.2 Time-step convergence study

A time step of T/512 is used in all case study simulations. To find the time step for capturing both the wave generation within the background mesh and the dynamic interaction between the fluid and the body within the overset mesh is important. To ensure the fidelity of the simulations and meaningful interpretation of results, a selection of the time step are imperative. Time step values of T/256, T/362, T/512, and T/724 are investigated, and the results are shown in Table 5.3. The temporal convergence study adopts the finest mesh resolution determined in the mesh convergence study. From this analysis, a time step of T/512 was selected as the optimal choice.

Table 5.3 Comparison of displacement of cylinder according to time-step

Wave case	Wave period T [s]	Wave height H [m]	PTO damping B_{PTO} [Nms]	Experiment (Windt et al., 2020a)	Time-step			
					T/256	T/362	T/512	T/724
9	2.8	0.25	200	0.0546	0.0489	0.0494	0.0496	0.0497

5.2.2 Simulation without the vertical wall

Using the input wave series shown in Table 5.1, the PTO data (cylinder displacement, PTO velocity, and PTO force) and absorbed power obtained by the numerical PTO model have

been compared for different damping coefficients The PTO data in Table 5.4, represents the mean height values, considering five consecutive peaks and troughs, and P_{abs} shows the averaged value during five consecutive wave periods. The table includes four different cases with different damping coefficients ($B_{exp} = 25, 50, 100, 200\ Nms$) obtained from Windt et al. (2020a).

In Figure 5.5, the time traces for PTO data and absorbed power are plotted for wave case 3 (T=1.4s and H=0.25m), which is the shortest wave period in this research. Analysing the displacement data reveals that as the damping coefficients increase, the amplitude of the displacements decreases. A similar trend is observed in the PTO velocity data. Conversely, the PTO force data exhibit an opposite trend to the displacement and PTO velocity data. Lastly, the absorbed power derived by the product of velocity and force, demonstrates a distinct pattern, recording high values when the damping coefficients are set to 50 and 100 Nms. It should be highlighted that maximising the cylinder displacements, the PTO velocity and force values are not directly related to achieving optimal performance in absorbed power. The important factor for better performance is linked to the phase between PTO velocity and force, thus, the selection of the optimum damping coefficient is crucial to produce the higher absorbed power.

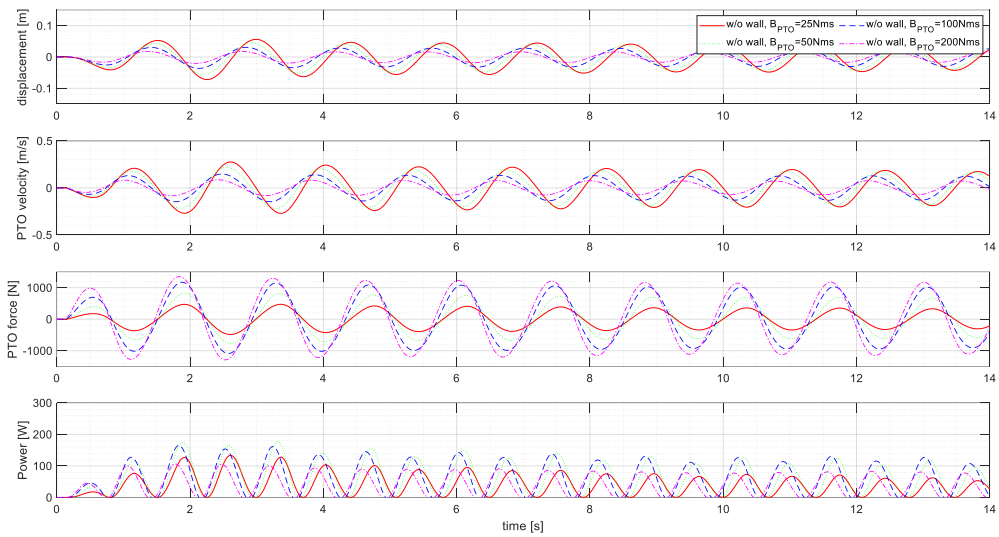

Figure 5.5 Results of numerical simulations without vertical wall for PTO data (displacement, PTO velocity and force) and absorbed power according to damping coefficient, wave case 2 (T=1.4s).

In Figure 5.6, the time traces for PTO data and absorbed power are depicted for wave case 5 (T=1.8s and H=0.25m). In a similar fashion to wave case 3, a comparative analysis of the PTO data and absorbed power is carried out based on the numerical PTO damping coefficients. In general, the cylinder displacements, PTO velocities and forces show similar behaviour to wave case 3, except for absorbed power. Particularly for wave case 5, the WEC device exhibits the most significant mean height value of cylinder displacement, presenting maximum motion across all wave cases. It is noteworthy that the natural period of this device,

excluding the PTO system, approximates 1.9s (Jakobsen et al., 2016). The absorbed power decreases as the numerical PTO damping increases. The peak value is observed when the numerical PTO damping is $25Nms$.

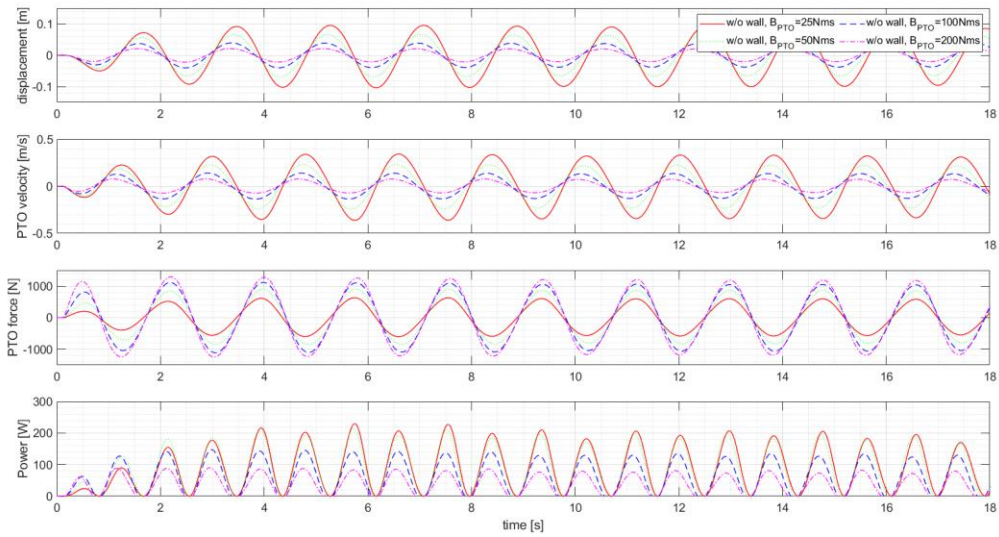

Figure 5.6 Results of numerical simulations without vertical wall for PTO data (displacement, PTO velocity and force) and absorbed power according to damping coefficient, wave case 4 (T=1.8s).

For wave case 10, the PTO data and absorbed power show a similar trend to wave case 3. The plotted time traces show a relatively decreased amplitude of PTO data, with velocity amplitude for wave case 10 being approximately half of that observed in wave case 5. Consequently, low amplitude of the PTO velocity and the wave power result in low absorbed power regardless of the numerical PTO damping coefficients.

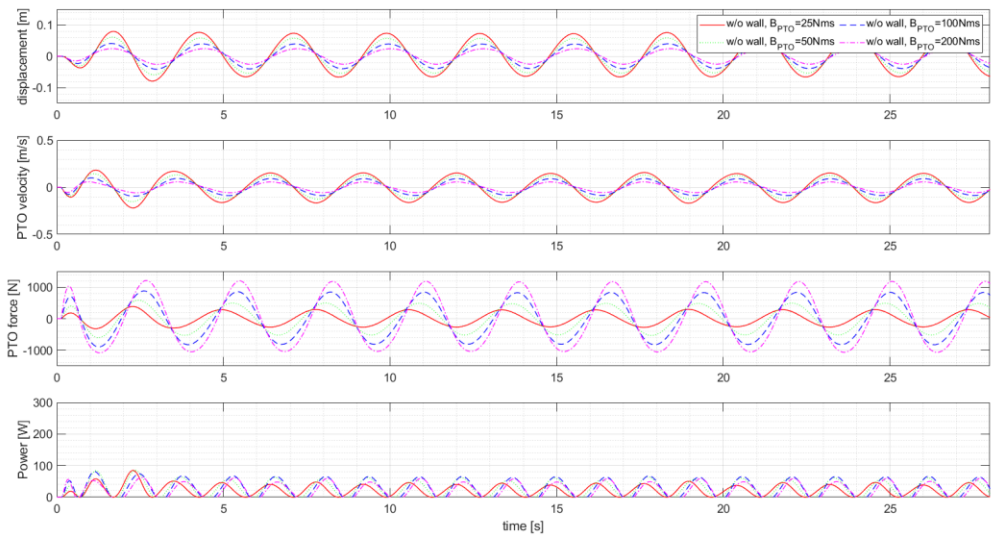

Figure 5.7 Results of numerical simulations without vertical wall for PTO data (displacement, PTO velocity and force)

and absorbed power according to damping coefficient, wave case 9 (T=2.8s).

Table 4 shows the results of the PTO data, absorbed power and CWR according to the wave cases and PTO damping coefficients, including the calculated available wave power based on each wave case.

Table 5.4 Results of PTO data, Power and CWR according to the wave cases and PTO damping coefficients without a vertical wall. The case shown the highest CWR has been highlighted in bold.

Wave case no.	B_{PTO} [Nms]	P_{wave} [W]	Displacement [m]	PTO velocity [m/s]	PTO force [N]	P_{abs} [W]	CWR [−]
2 (T=1.4)	25	83.76	0.088	0.397	694.00	34.11	0.407
	50		0.080	0.361	1310.88	56.49	0.674
	100		0.058	0.259	1964.34	58.20	**0.695**
	200		0.033	0.148	2301.28	37.81	0.451
3 (T=1.6)	25	95.73	0.143	0.563	985.77	68.69	0.718
	50		0.112	0.441	1622.80	84.70	**0.885**
	100		0.070	0.274	2135.92	65.58	0.685
	200		0.037	0.148	2385.87	38.01	0.397
4 (T=1.8)	**25**	107.69	0.188	0.666	1165.22	95.30	**0.885**
	50		0.129	0.453	1687.54	89.19	0.828
	100		0.075	0.263	2107.36	60.52	0.562
	200		0.040	0.142	2371.18	34.69	0.322
5 (T=1.9)	**25**	113.68	0.196	0.657	1149.68	92.41	**0.813**
	50		0.131	0.436	1634.43	82.59	0.726
	100		0.076	0.253	2058.82	56.07	0.493
	200		0.041	0.138	2341.32	32.65	0.287
6 (T=2.0)	**25**	119.66	0.197	0.628	1098.44	84.17	**0.703**
	50		0.132	0.416	1571.16	75.19	0.628
	100		0.078	0.245	2019.42	52.40	0.438
	200		0.042	0.135	2330.36	31.31	0.262
7 (T=2.2)	**25**	131.63	0.182	0.525	918.46	59.18	**0.450**
	50		0.127	0.363	1391.03	57.29	0.435
	100		0.079	0.225	1911.96	44.16	0.336
	200		0.044	0.130	2296.76	28.46	0.216
8 (T=2.5)	25	149.57	0.154	0.389	681.07	32.76	0.219
	50		0.116	0.294	1152.14	37.50	**0.251**
	100		0.078	0.198	1757.14	34.16	0.228
	200		0.047	0.121	2247.65	24.86	0.166
9 (T=2.8)	25	167.52	0.138	0.313	548.19	21.21	0.127
	50		0.111	0.250	1005.73	27.12	0.162
	100		0.079	0.178	1654.32	27.59	**0.165**
	200		0.050	0.114	2232.33	22.02	0.131

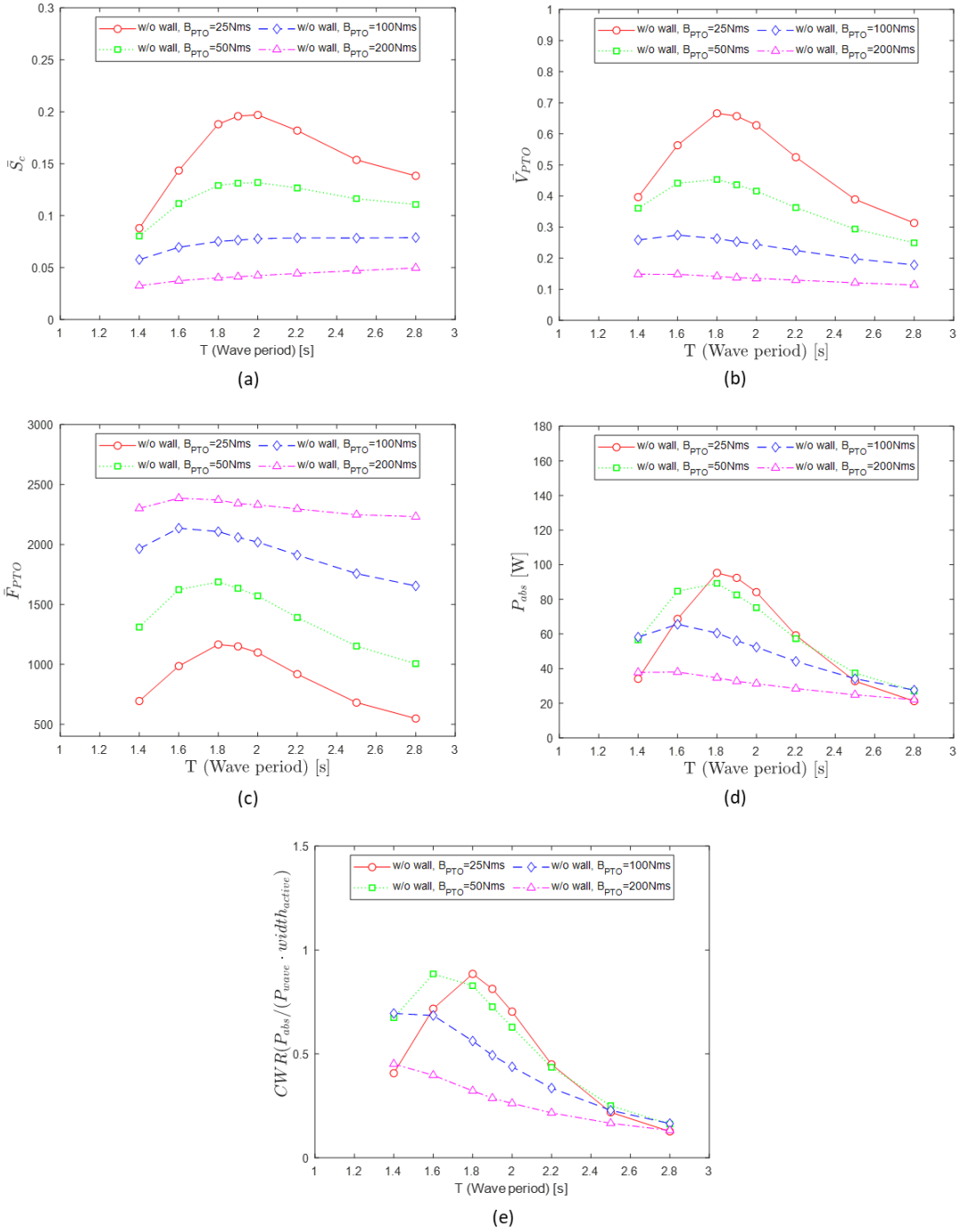

Figure 5.8 Comparison of numerical results for Case study 1: Simulation without a vertical wall according to different wave periods and PTO damping coefficients ((a): mean height of cylinder displacement, (b): mean height of PTO velocity, (c): mean height of PTO force, (d): averaged absorbed power, (e): CWR).

In Figure 5.8, the mean value of the cylinder displacement, PTO velocity, PTO force and absorbed power are illustrated as a function of the wave period across various damping coefficients for the WEC. The mean values are determined using the same analytical approach as employed in Section 5.2.1. The figure includes different line colours and styles representing damping coefficients ranging from 25 to 200 Nms.

It is evident from the graphs that the damping coefficients significantly influence the PTO values and the absorbed power of the WEC. $\bar{S}_c$ is greatest with the lowest damping coefficient, and as the damping coefficient increases, $\bar{S}_c$ decreases. The damping coefficients of 25 Nms and 50 Nms indicate a higher value of $\bar{S}_c$ near the natural period of the WEC, which is more evident with lower damping coefficients. On the other hand, with increasing damping coefficients, the change in $\bar{S}_c$ near the natural period of the WEC becomes insignificant, indicating an overall reduction in $\bar{S}_c$ in each wave condition. This phenomenon aligns with general observations of increased damping.

Figure 5.8 (b) shows the variation in $\bar{V}_{PTO}$ with respect to the wave period. Overall, it mirrors the pattern observed in $\bar{S}_c$. However, a notable difference is that the wave period corresponding to the peak value of $\bar{V}_{PTO}$ decreases as the damping increases.

Figure 5.8 shows the displacement of the WEC as a function of wave period for different damping coefficients. The mean height of values is obtained in the same analysis method as employed in Section 5.2.1. The different lines represent different damping coefficients from 25 to 200 Nms. The graphs show that the damping coefficient has a significant impact on the displacement, PTO velocity, PTO force and absorbed power of the WEC. $\bar{S}_c$ is greatest with the lowest damping coefficient, and as the damping coefficient increases, $\bar{S}_c$ decreases. The damping coefficients of 25 and 50 indicate a higher value of $\bar{S}_c$ near the natural period of the WEC, which is more evident with the smaller damping coefficient. On the other hand, as the damping coefficient increases, the change in the $\bar{S}_c$ is insignificant in the vicinity of the natural period, and it can be seen that the overall response of $\bar{S}_c$ according to the wave case becomes smaller. This is a general phenomenon that occurs as the damping of an object increases.

Figure 5.8 (b) shows the change in $\bar{V}_{PTO}$ as a function of wave period. Overall, it shows a similar pattern to the change in $\bar{S}_c$. The peak value of $\bar{V}_{PTO}$ when $B_{PTO} = 25Nms$ is observed at $T = 1.8s$. As the damping coefficient increases, the overall magnitude of $\bar{V}_{PTO}$ decreases, and the gap between its maximum and minimum value of $\bar{V}_{PTO}$ narrows. Figure 5.8(c), shows the variation of $\bar{F}_{PTO}$ as function of the wave period. As the damping coefficient increases and there is a decrease in the overall magnitude of $\bar{F}_{PTO}$. The overall magnitude is obviously correlated with the B_{PTO} rather than the magnitude of $\bar{S}_c$ and $\bar{V}_{PTO}$. Figure 5.8(d) illustrates the results of P_{abs} in relation to the wave period.

In the case of $\bar{S}_c$, it can be seen that the wave period in which the maximum value of $\bar{V}_{PTO}$ appears decreases as the damping increases, whereas in the case of $\bar{S}_c$, the peak value is mainly shown near the natural period.

5.2.3 Simulation with the vertical wall

In this section, simulation results with and without the precense of a vertical wall are compared, using the same methodology as was in the previous case of simulations without the vertical wall. A comparative analysis between Case 1 and Case 2 are also included.

Figure 5.9 illustrates the displacement, PTO velocity, force, and power results of the WEC for different PTO damping values when a vertical wall is present. As observed in the results, similar to the case without the vertical wall, the amplitude of PTO displacement gradually decreases with an increase in PTO damping. The overall trend of the time traced results closely resembles that of Case 1, with the only difference being the amplitude variation.

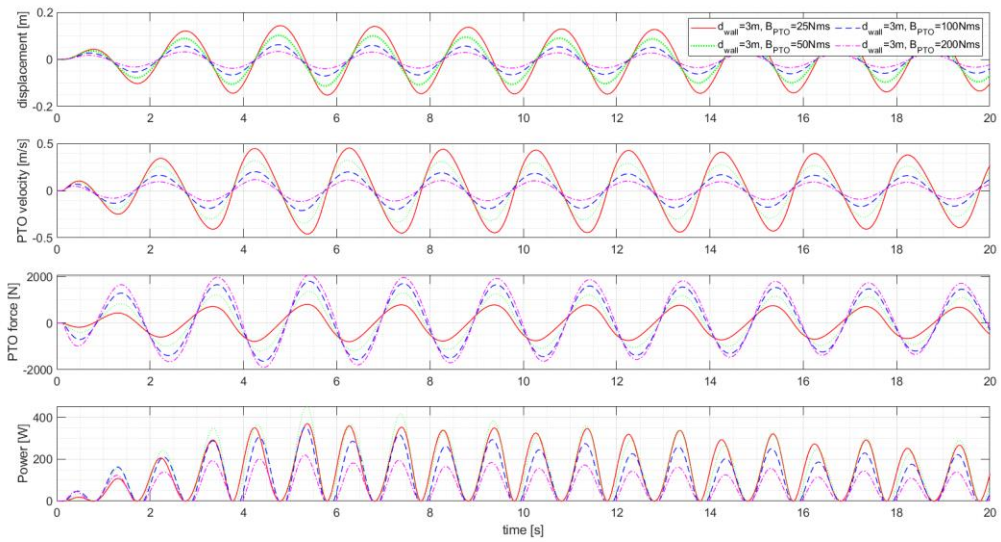

Figure 5.9 Results of numerical simulations with vertical wall for PTO data (displacement, PTO velocity and force) and absorbed power according to damping coefficient, wave case 6 (T=2.0s). d_{wall} denotes the distance between a vertical wall and a buoy.

Figure 5.10 illustrates the performance of the WEC when installed on a vertical wall, while Table 5.5 lists detailed numerical values. The results vary with the wave period and PTO damping, generally showing significant motion responses and absorbed power values when the wave period is between 2 and 2.2 seconds. Despite the occurrence of stationary wave phenomena around the WEC due to the presence of the vertical wall, the predominant influence is demonstrated by the motion induced by the WEC's characteristic of the natural period. In Figure 5.10(e), a sudden change in values is observed when the wave period is 1.8s compared to periods of 1.6s or 2s. This abrupt change is attributed to the positioning of the WEC buoy near the vertical wall. The presence of a vertical wall induces a stationary wave effect around the WEC buoy, leading to the phenomenon of reduced wave height at specific locations. Furthermore, the area around the WEC buoy is expected to exhibit complex wave pattern due to the coexistence of incident and reflected waves, as well as waves generated by the WEC buoy and its corresponding reflected waves. It is highlighted that CWR exceeds 1.0,

which is attributed to the high absorbed power resulting from the stationary wave effects. Additionally, in the absence of a vertical wall, low CWR was predicted for PTO damping values of 100 Nms or 200 Nms. However, with the presence of a vertical wall, it is noteworthy that a significant CWR was recorded even with high PTO damping. However, even with the presence of the vertical wall, low CWR values were recorded for all PTO damping values when the wave period was 2.8s.

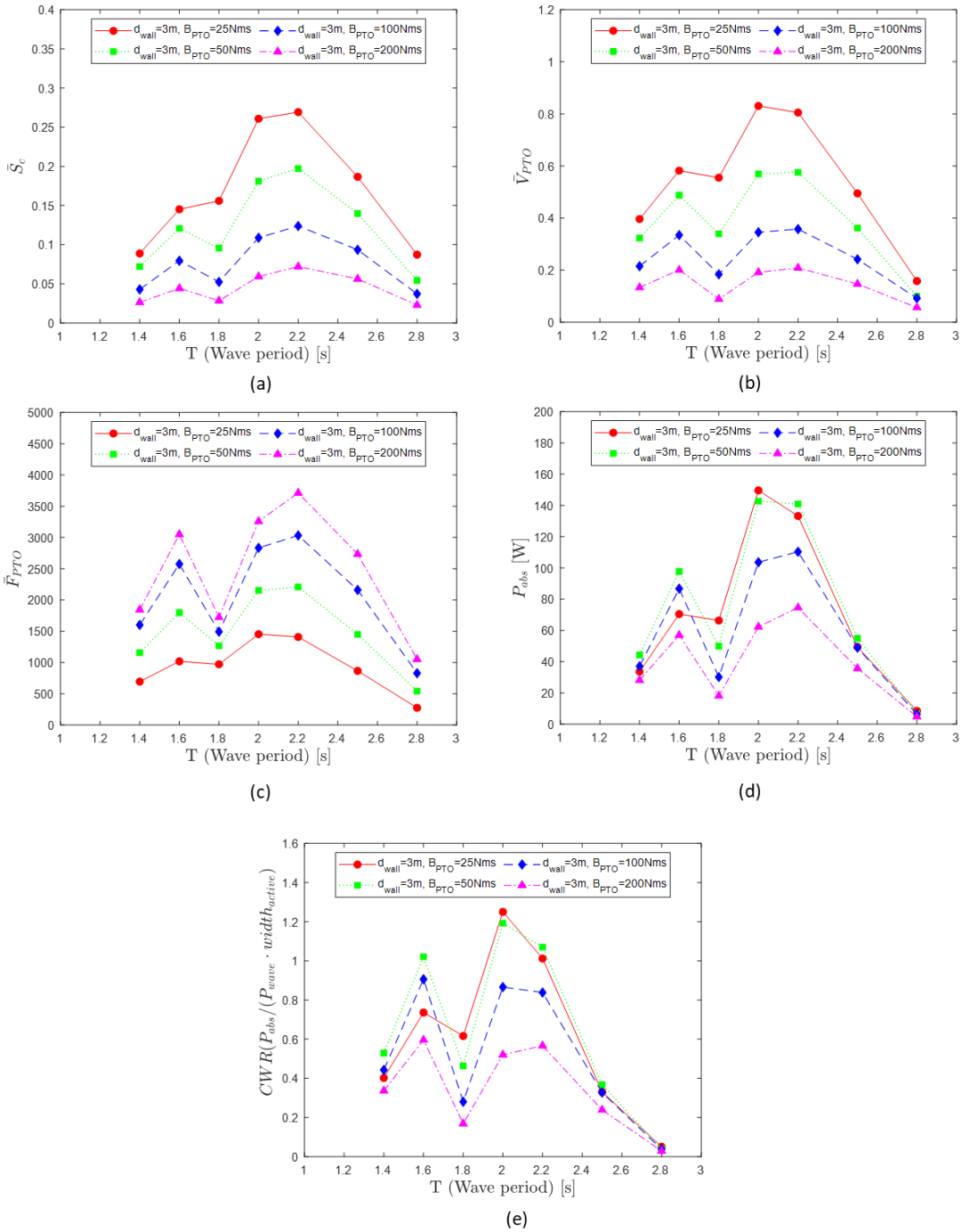

Figure 5.10 Comparison of numerical results for Case study 2: Simulation with vertical wall according to wave period and PTO damping coefficient ((a): mean height of cylinder displacement, (b): mean height of PTO velocity, (c): mean height of PTO force, (d): averaged absorbed power, (e): CWR). d_{wall} denotes the distance between a vertical wall and a buoy.

Table 5.5 Result of PTO data, Power and CWR according to wave case and damping coefficients for the cases with the vertical wall. The case shown the highest CWR has been highlighted in bold.

Wave case no.	B_{exp} [Nms]	P_{wave} [W]	Displacement [m]	PTO velocity [m/s]	PTO force [N]	P_{abs} [W]	CWR [−]
2	25	83.76	0.089	0.396	694.21	33.67	0.402
	50		0.072	0.323	1157.08	44.28	**0.529**
	100		0.043	0.215	1601.06	37.09	0.443
	200		0.026	0.134	1844.57	28.20	0.337
3	25	95.73	0.145	0.582	1018.73	70.48	0.736
	50		0.121	0.488	1798.25	97.75	**1.021**
	100		0.079	0.335	2575.37	86.75	0.906
	200		0.044	0.201	3050.56	57.07	0.596
4	**25**	107.69	0.156	0.555	971.47	66.37	**0.616**
	50		0.096	0.339	1266.48	49.95	0.464
	100		0.052	0.184	1492.66	30.20	0.280
	200		0.029	0.089	1723.35	18.18	0.169
6	**25**	119.66	0.261	0.831	1453.55	149.61	**1.250**
	50		0.181	0.569	2153.87	142.68	1.192
	100		0.109	0.345	2834.00	103.65	0.866
	200		0.059	0.192	3259.05	62.29	0.521
7	25	131.63	0.269	0.805	1408.41	133.22	1.012
	50		0.197	0.575	2207.63	140.90	**1.070**
	100		0.124	0.358	3032.41	110.35	0.838
	200		0.072	0.209	3712.62	74.61	0.567
8	25	149.57	0.187	0.495	866.20	49.44	0.331
	50		0.140	0.362	1450.13	54.97	**0.368**
	100		0.093	0.242	2160.96	48.98	0.327
	200		0.056	0.147	2734.50	35.73	0.239
9	**25**	167.52	0.087	0.158	276.31	8.54	**0.051**
	50		0.054	0.099	543.54	6.68	0.040
	100		0.037	0.092	829.27	6.39	0.038
	200		0.023	0.057	1052.76	4.87	0.029

Figure 5.11 compares the CWR under the same PTO damping values, with a focus on the presence or absence of the vertical wall. A comparison of results for the case where PTO damping is at its minimum value of 25 Nms can be seen in Figure 5.11(a). The most significant difference is observed in the wave period range of 1.8s to 2.2s, which corresponds to the natural period of the WEC buoy. As the PTO damping increases, it can be observed that in the case of no vertical wall, the wave period at which CWR exhibits its peak gradually shifts towards shorter periods. On the other hand, in the presence of the vertical wall, regardless of changes in PTO damping, the peak of CWR mostly occurs when the wave period is around 2s. This indicates that by adjusting the spacing between the vertical wall and the buoy appropriately and utilizing stationary wave near the buoy effectively, this can be an effective way to enhance CWR.

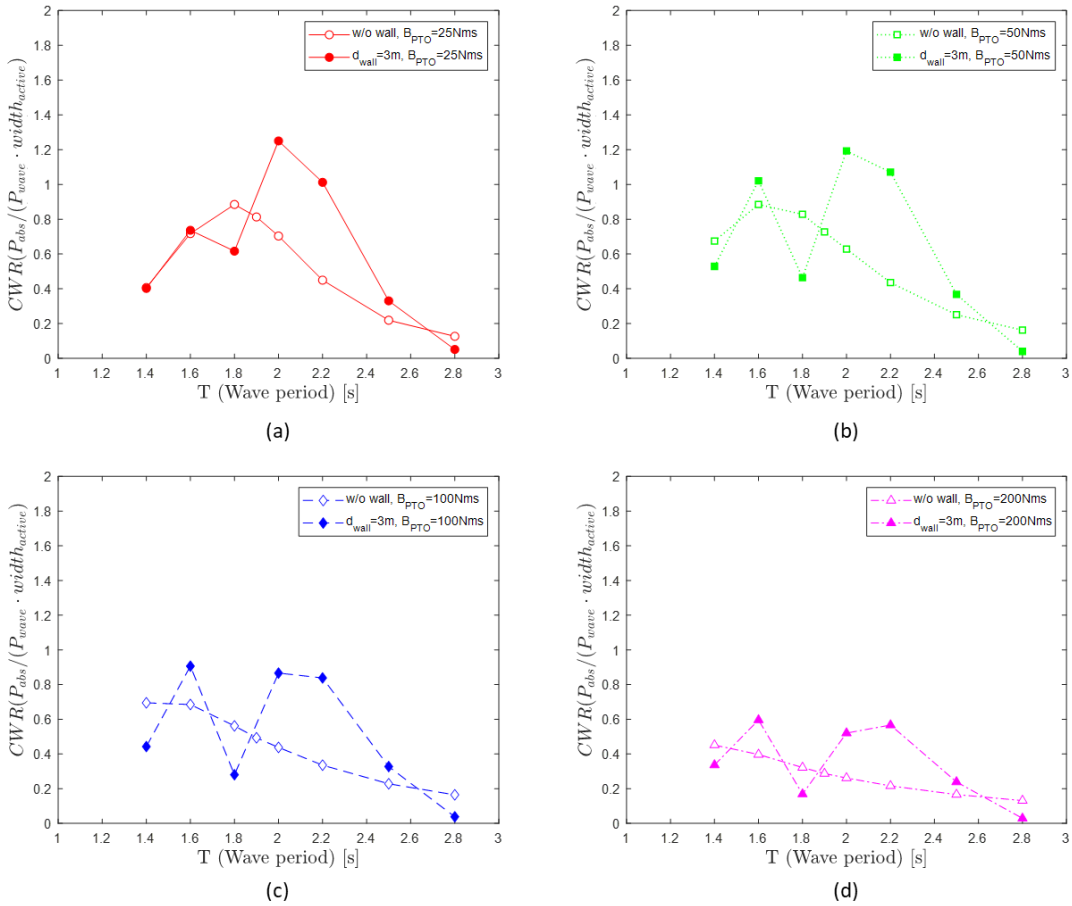

Figure 5.11 Comparison of CWR based on the presence of absence of the vertical wall ((a) : $B_{PTO} = 25\ Nms$, (b) : $B_{PTO} = 50\ Nms$, (c) : $B_{PTO} = 100\ Nms$, (d) : $B_{PTO} = 200\ Nm$). d_{wall} denotes the distance between a vertical wall and a buoy.

5.2.4 Simulation without vertical wall and under latching control

In this section, the results are presented when there is no vertical wall and when latching control is introduced. These results are compared with a corresponding case (Section 5.2.2) where there is no vertical wall and no latching control, establishing a basis for the comparison between the two scenarios.

Figure 5.12 displays the time-dependent results of PTO displacement, velocity, force, and power for wave periods of 2.8s, considering PTO damping values of 25 and 50 Nms. It can be observed that latching control initiates after 8.5s when the buoy's velocity becomes 0 (Note: $t_{transition}$ is set to 3T.). Once latching control begins, the displacement gradually increases and exhibit periodic variations after approximately two cycles. The constant latching duration is determined by Equation (3.22) , and it can be verified from the graph that there is no change in the displacements during this constant latching duration. After the constant latching duration has elapsed, it can be confirmed that the WEC buoy is released. Following this release, it is evident from the graph that there is a steeper change or slope in the displacements compared to the scenario where the latching control was not applied. Not

only in the displacements but also in the velocity and force, similar patterns are observed. Additionally, due to the improvement in PTO velocity and force induced by latching control, it can be confirmed that the peak of power is elevated.

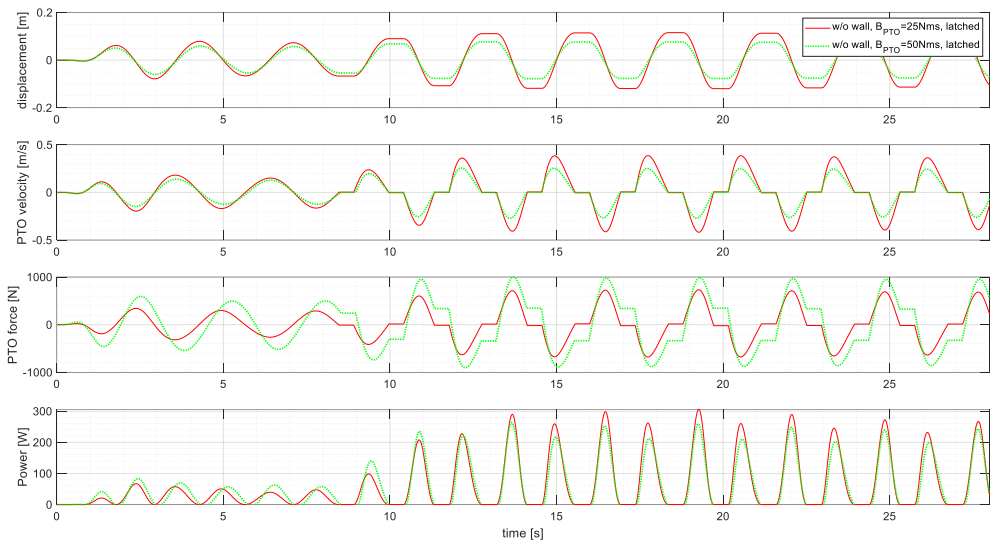

Figure 5.12 Results of numerical simulations without vertical wall under latching control for PTO data (displacement, PTO velocity and force) and absorbed power according to damping coefficient, wave case 9 (T=2.8s).

Figure 5.13 presents the results when latching control is employed without a vertical wall, along with the PTO displacement, velocity, and force, absorbed power, and CWR results in Section 5.2.2. Since Equation (3.20) is valid under the condition where the wave period of the incident wave is greater than the natural period of the object, this study only presents results for wave periods of 2.2, 2.5, and 2.8s. The implementation of latching control leads to an increase not only in the displacements but also in the velocity, force, and absorbed power. Consequently, there is a substantial improvement in CWR. In the case without latching control, CWR recorded values below 0.2 for long wave periods. However, with the introduction of latching control, a notable effect was observed, with CWR exceeding 0.4 across all wave period conditions. The numerical results for the case with latching control, as depicted in Figure 5.13, can be seen in Table 5.2.

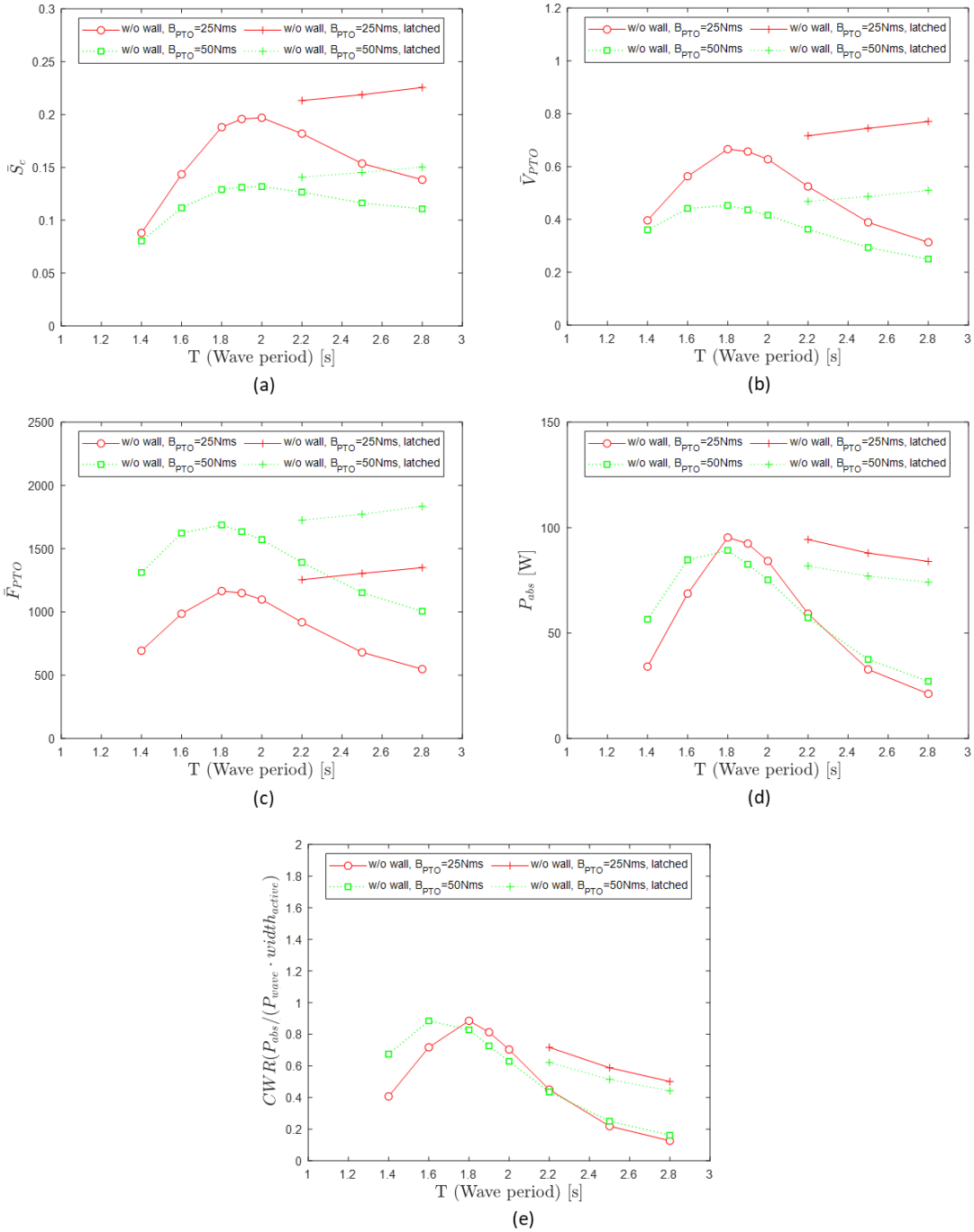

Figure 5.13 Comparison of numerical results for Case study 3: Simulation without vertical wall and latching control according to wave period and PTO damping coefficient ((a): mean height of cylinder displacement, (b): mean height of PTO velocity, (c): mean height of PTO force, (d): averaged absorbed power, (e): CWR).

Table 5.6 Result of PTO data, Power and CWR according to wave case and damping coefficients for the cases without the vertical wall and latching control. The case shown the highest CWR has been highlighted in bold.

Wave case no.	B_{exp} [Nms]	P_{wave} [W]	Displacement [m]	PTO velocity [m/s]	PTO force [N]	P_{abs} [W]	CWR [−]
7	**25**	131.63	0.213	0.717	1255.16	94.37	**0.717**
	50		0.141	0.468	1725.58	81.80	0.621
8	**25**	149.57	0.219	0.745	1304.92	87.93	**0.588**
	50		0.145	0.487	1772.38	76.99	0.515
9	**25**	167.52	0.226	0.771	1350.27	83.95	**0.501**
	50		0.150	0.510	1834.33	74.10	0.442

5.2.5 Simulation with vertical wall and under latching control

The previous section examined the changes in the performance of the WEC upon the introduction of latching control (Section 5.2.4). In this section, not only the effects of latching control but also the synergistic effects when a vertical wall is present alongside latching control in the WEC are investigated.

Figure 5.14 illustrates the results of simulations with both the vertical wall and latching control when wave period is 2.2s. It displays the time-dependent PTO displacement, velocity, force, and absorbed power. There does not appear to be a significant overall difference in PTO displacement, velocity, force, and absorbed power with varying PTO damping values compared to the previous cases.

From around 7s in the simulations, latching control is initiated. Despite the PTO displacements not showing significant changes for $B_{PTO} = 25Nms$, there is a slight increase in the maximum and minimum values of velocity. This impact ultimately leads to higher power, and as a result, an increase in CWR. These results can be seen in Figure 5.15.

Due to the effects of latching control, similar to the result of Section 5.2.4, there is a relatively improved performance in the long-wave period range (T=2.5s and 2.8s), resulting in enhanced absorbed power and CWR. Additionally, even in the case with a vertical wall at T=2.2s yields a CWR exceeding 1, the introduction of latching control further improves the performance. Detailed numerical results can be found in Table 5.7

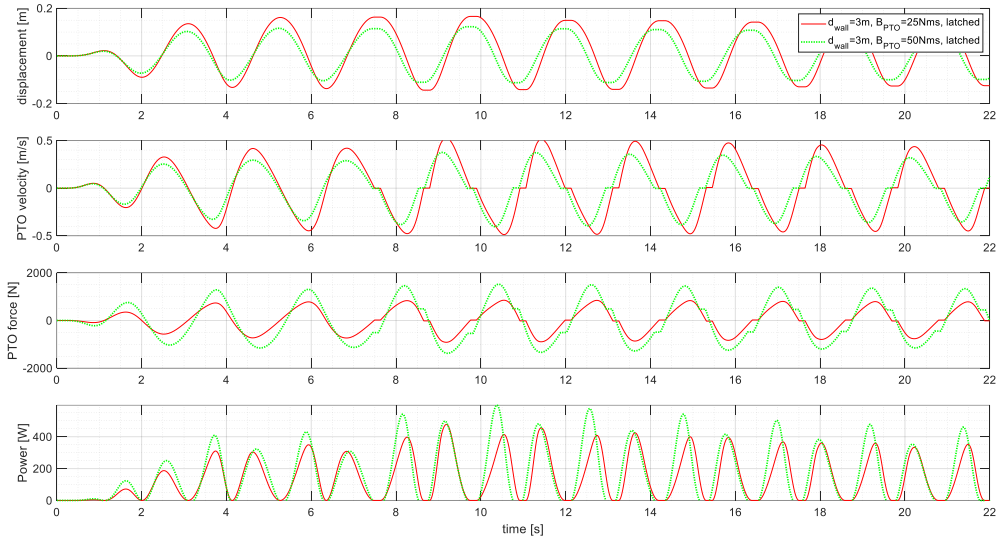

Figure 5.14 Results of numerical simulations with vertical wall under latching control for PTO data (displacement, PTO velocity and force) and absorbed power according to damping coefficient, wave case 7 (T=2.2s). d_{wall} denotes the distance between a vertical wall and a buoy.

To examine the effect of the vertical wall in the presence of latching control, the results of Section 5.2.4 and Section 5.2.5 are compared, as shown in Figure 5.16. With a PTO damping of 25 Nms and a wave period 2.2 seconds, it can be observed that the presence of the vertical wall increases CWR from 0.72 to 1.20. Furthermore, with a PTO damping of 50 Nms, an even larger increase from 0.62 to 1.43 is noted. As the wave period increases, it can be observed that the magnitude of the CWR variation due to presence of the vertical wall gradually decreases. Additionally, without a vertical wall, the change in CWR as function of the wave period is small, while with the vertical wall, the variation in CWR as a function of the wave period is more pronounced.

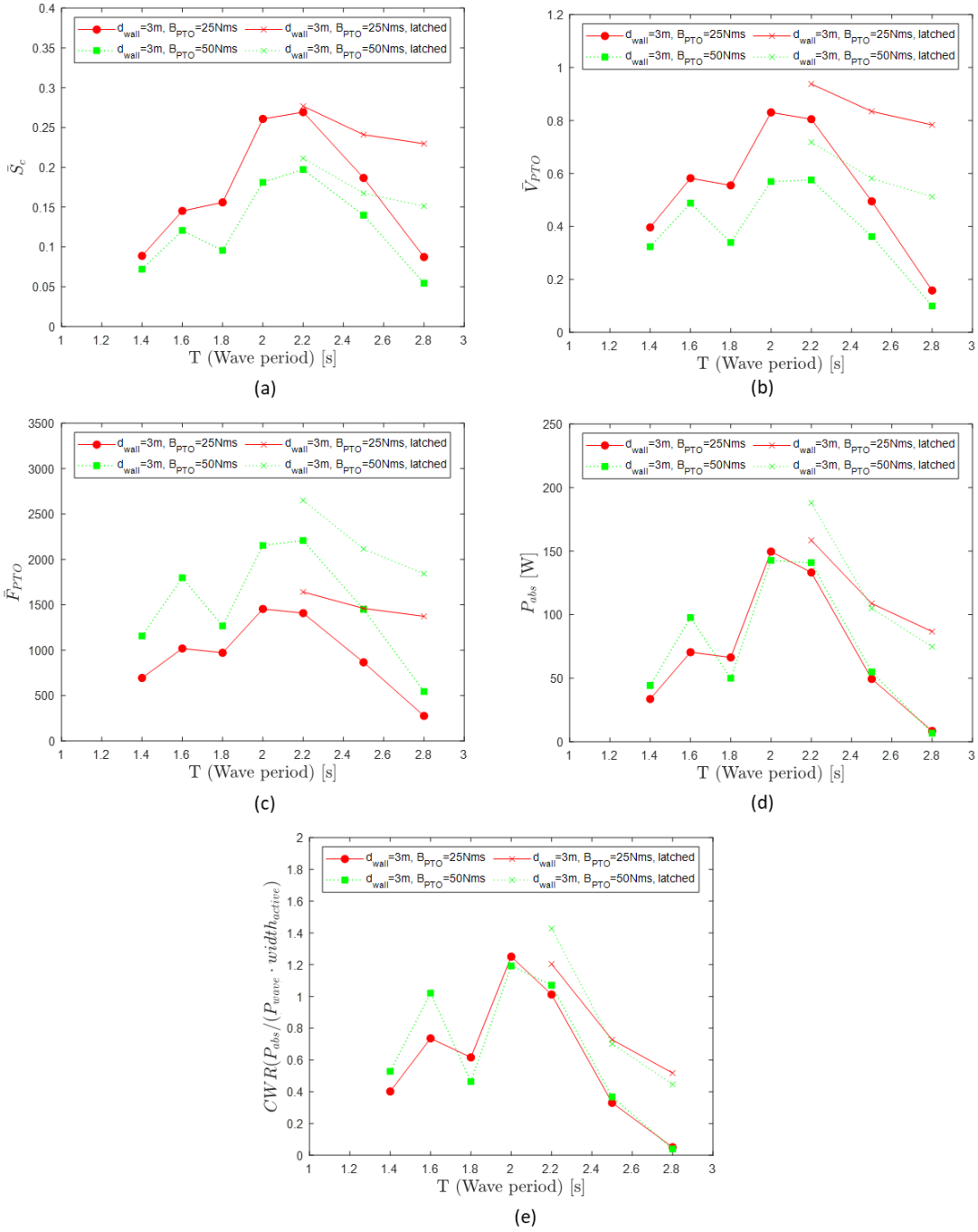

Figure 5.15 Comparison of numerical results for Case study 4: Simulation with vertical wall and under latching control according to wave period and PTO damping coefficient ((a): mean height of cylinder displacement, (b): mean height of PTO velocity, (c): mean height of PTO force, (d): averaged absorbed power, (e): CWR). d_{wall} denotes the distance between a vertical wall and a buoy.

Table 5.7 Result of PTO data, Power and CWR according to wave case and damping coefficients for the cases with the vertical wall and under latching control. The case shown the highest CWR has been highlighted in bold.

Wave case no.	B_{exp} [Nms]	P_{wave} [W]	Displacement [m]	PTO velocity [m/s]	PTO force [N]	P_{abs} [W]	CWR [−]
7	25	131.63	0.277	0.938	1641.01	158.50	1.204
	50		0.211	0.718	2649.95	187.94	**1.428**
8	**25**	149.57	0.241	0.834	1460.56	108.80	**0.727**
	50		0.167	0.581	2115.36	104.98	0.702
9	**25**	167.52	0.230	0.783	1372.66	86.74	**0.518**
	50		0.151	0.512	1841.88	74.80	0.446

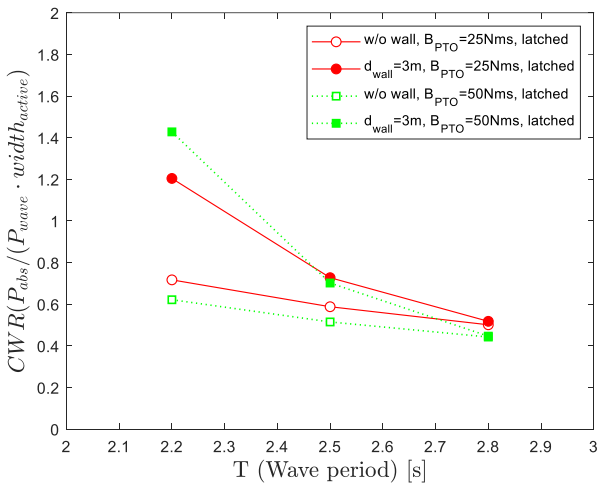

Figure 5.16 Comparison of CWR based on the presence of absence of the vertical wall for $B_{PTO} = 25\ Nms$, and $50\ Nms$. d_{wall} denotes the distance between a vertical wall and a buoy.

5.3 Concluding remarks

The primary objective of this investigation was to thoroughly assess the impact of a vertical wall and latching control through an in-depth case study, and to further expand upon the earlier Chapter 4, which primarily delved into the hydrodynamic performance of the WEC in relation to the distance between the vertical wall and the WEC. In order to evaluate the performance of the WEC, a numerical power take-off (PTO) design was implemented, and this design was subsequently utilized in the numerical simulation through the utilization of the Star-CCM+ software.

Modifications were made to the 1-D linear spring-damping system that was originally proposed by Windt et al. (2020), and the latching control algorithm was adapted to suit the needs of this study. Furthermore, verification study and comparison with other published data (Windt et al., 2020a, Ghafari et al., 2021) were carried out in order to fully establish the validity of the computational domain that was employed in this study.

The findings that were obtained from this study were then compared to the results of experimental measurements as well as other numerical simulations that were conducted as part of different studies. This comparison revealed discrepancies and ultimately served to confirm the overall reliability of the numerical simulations that were carried out in this study.

In order to properly compare the performance of the WEC with and without the presence the vertical wall, two distinct cases were analysed: Section 5.2.2, which involved a simulation without the vertical wall, and Section 5.2.3, which involved a simulation with the vertical wall positioned a distance of 3m away from the buoy. Both cases were examined under a variety of different wave periods and power take-off (PTO) damping values.

The results obtained from this analysis clearly indicated that for wave periods of 2s and 2.2s, the WEC consistently exhibited a high CWR regardless of the specific PTO damping force that was utilized. However, when longer wave periods were considered, specifically those corresponding to 2.5s or more, the presence of the vertical wall did not appear to significantly impact the CWR. As a result, the recorded CWR values were found to be lower in these instances. Following this analysis, the effects of the latching control mechanism were also examined, and it was observed that the motions of the WEC were indeed improved as a direct result of the latching control. The findings showed consistent and significant improvements specifically within the long-wave period range. However, it is important to note that this study placed a specific focus on constant latching control, and as such, latching control was not applied in the region where the wave period was shorter than the natural period of the WEC.

Finally, in this study a comparative analysis was carried out to investigate the effects of the presence of a vertical wall during the latching control process. The results indicated that the best captured wave energy ratio was recorded when the wave period was 2.2s. This improvement was not only evident in the result of simulations with the vertical wall (Section 5.2.3), but also in the instance where the highest CWR was achieved with a wave period of 2.2s. Furthermore, it was found that the enhancement in CWR that was brought about by the presence of the vertical wall was further improved when the latching control mechanism was applied. This finding pointed towards a complementary interaction between the effects of the vertical wall and the latching control. However, as the wave period continued to increase, the overall influence of the presence of the vertical wall became less significant. Ultimately, this study serves as a demonstration of the fact that the utilization of a vertical wall and latching control has the potential to enhance the overall performance of the WEC.

6 Summary and Discussions

The investigation presented in this study focused on two critical aspects of wave energy conversion: the influence of the distance between a vertical wall and a pivoted Wave Energy Converter (WEC) and the impact of a Power Take-Off (PTO) and latching control on the WEC's performance.

In Chapter 2, a literature review was carried out on the previous studies in the field of Wave Energy Converters (WECs), together with the investigation of related existing evaluation for WEC performance and integration of WECs and vertical walls. Furthermore, implementation of different PTO models and latching controls based on different analysis methods was reviewed.

Chapter 3 provides a comprehensive methodology for assessing the performance of a Wave Energy Converter (WEC) using an unsteady Reynolds-Averaged Navier-Stokes (RANS) solver. The description includes a detailed account of each stage in the numerical setup for WEC-vertical wall simulations. The foundational research for conducting simulations without the vertical wall is outlined, followed by a detailed explanation of the techniques applied for simulating WEC with the presence of a vertical wall. Specifically, the wave forcing scheme is elaborated upon. Additionally, the methodology for implementing the Power Take-Off (PTO) system is described, and an in-depth explanation of the algorithm used for introducing latching control is provided. This chapter serves as a crucial resource for understanding the key components and steps involved in the numerical modelling and simulation of WEC systems in varying configurations.

In Chapter 4, a numerical model for the pivoted WEC device successfully compared with experimental data, demonstrating good agreement between the numerical model, and published experimental data. The motion response of the WEC body as function of the distance from a vertical wall was effectively captured, highlighting the significance of the stationary wave generated by the vertical wall. The analytical solution provided insights into predicting stationary waves, correlating well the with numerical simulations. Through an analysis of case studies evaluating the hydrodynamic performance at varying distance from the vertical wall, it becomes apparent that the presence of the vertical wall significantly affects the motion of WEC.

Chapter 5 delved into a detailed case study, expanding on the previous investigation to explore the impact of a Power Take-Off (PTO) and latching control. The successful implementation of the designed numerical PTO system is confirmed through a comparison of the result of present numerical simulation with other published data including experimental measurements and CFD results. The performance of the WEC was enhanced in the presence of a vertical wall, particularly for a specific wave period aligned with the natural period of the WEC. However, there was no substantial improvement observed for wave periods outside the range of the natural period of the WEC. The integration of a vertical wall and the application

of latching control showed significant improvements in the WEC's performance, particularly in longer wave periods. The interaction between the vertical wall and latching control demonstrated potential enhancements in wave energy capture.

The novelty of this work lies in its dual focus on the impact of vertical wall distance and advanced control mechanisms (PTO and latching control) on the performance of pivoted WECs. This study provides a numerical methodology that simulates WEC behaviour in varying configurations, filling a hap in existing research. The findings highlight the potential for significant performance enhancements in WEC systems through integration with the vertical wall and PTO and latching control techniques.

6.1 Recommendations for future research

In the purpose of advancing the field of Wave energy converters (WECs), this thesis acknowledges several critical areas, demanding additional investigations and improvements.

Firstly, even though the numerical data in this thesis compared with the other experimental measurements, conducting experiments for validation in a physical tank give accuracy to the numerical model, enhancing the findings from interaction between the vertical wall and WEC.

In experimental tests, mechanical friction losses are inevitable due to factors such as bearings installed on hinges and internal friction within the PTO. However, incorporating all these aspects into a CFD model poses a significant challenge currently. Further research in this area is deemed necessary, and such studies can provide valuable insights, especially concerning scale-up issues of the PTO for prototype.

Investigating control strategies under various wave conditions, considering different wave periods and amplitudes could expand the WEC’s adaptability. This thesis provides the foundation for the constant latching control so this will help the future research to improve the other latching control strategies.

This study focuses on the effects of introducing latching control to a WEC installed on a vertical wall. As a result, there is a gap in research regarding the optimal latching control in the specific environment. Additional studies are needed to investigate harnessing the synergy between stationary wave effects and latching control for maximising WEC efficiency on the vertical wall.

Additionally, this study is conducted under the assumption of regular waves, omitting research on irregular wave conditions that more closely mimic real-world scenarios. Conducting research on WEC-vertical wall interactions in irregular wave conditions using the numerical methods employed in this study would contribute significantly to the understanding of practical applications.

Addressing these research gaps can enhance the comprehensiveness and practical applicability of studies on WECs, providing valuable insights into the complexities associated with real-world applications and improving the efficiency of wave energy conversion systems.

Reference

AHAMED, R., MCKEE, K. & HOWARD, I. 2020. Advancements of wave energy converters based on power take off (PTO) systems: A review. *Ocean Engineering,* 204**,** 107248.

AVALOS, G. O. G. & ESTEFEN, S. F. 2021. Viscous effect for heaving cylindrical point absorbers controlled by a latching control system and a novel approach to viscous force. *Journal of ocean engineering and marine energy.,* 7**,** 363-378.

BABARIT, A. 2017. 2 - Wave Energy Conversion Historical Perspective. *In:* BABARIT, A. (ed.) *Wave Energy Conversion.* Elsevier.

BABARIT, A. & CLÉMENT, A. H. 2006. Optimal latching control of a wave energy device in regular and irregular waves. *Applied Ocean Research,* 28**,** 77-91.

BABARIT, A., DUCLOS, G. & CLÉMENT, A. H. 2004. Comparison of latching control strategies for a heaving wave energy device in random sea. *Applied Ocean Research,* 26**,** 227-238.

BABARIT, A., GUGLIELMI, M. & CLÉMENT, A. H. 2009. Declutching control of a wave energy converter. *Ocean Engineering,* 36**,** 1015-1024.

BJARTE-LARSSON, T. & FALNES, J. 2006. Laboratory experiment on heaving body with hydraulic power take-off and latching control. *Ocean Engineering,* 33**,** 847-877.

BUDAL, K. & FALNES, J. 1980. Interacting point absorbers with controlled motion. *POWER FROM SEA WAVES.* EDINBURGH: ACADEMIC PRESS.

CELIK, I. B., GHIA, U., ROACHE, P. J., FREITAS, C. J., COLEMAN, H. & RAAD, P. E. 2008. Procedure for Estimation and Reporting of Uncertainty Due to Discretization in CFD Applications. *Journal of Fluids Engineering,* 130**,** 0780011-0780014.

CHEN, Q., ZANG, J., BIRCHALL, J., NING, D., ZHAO, X. & GAO, J. 2020. On the hydrodynamic performance of a vertical pile-restrained WEC-type floating breakwater. *Renewable Energy,* 146**,** 414-425.

CHENG, Y., XI, C., DAI, S., JI, C., COCARD, M., YUAN, Z. & INCECIK, A. 2021. Performance characteristics and parametric analysis of a novel multi-purpose platform combining a moonpool-type floating breakwater and an array of wave energy converters. *Applied Energy,* 292**,** 116888.

CHENG, Y., XI, C., DAI, S., JI, C., COLLU, M., LI, M., YUAN, Z. & INCECIK, A. 2022. Wave energy extraction and hydroelastic response reduction of modular floating breakwaters as array wave energy converters integrated into a very large floating structure. *Applied Energy,* 306**,** 117953.

CLÉMENT, A., MCCULLEN, P., FALCÃO, A., FIORENTINO, A., GARDNER, F., HAMMARLUND, K., LEMONIS, G., LEWIS, T., NIELSEN, K., PETRONCINI, S., PONTES, M. T., SCHILD, P., SJÖSTRÖM, B.-O., SØRENSEN, H. C. & THORPE, T.

2002. Wave energy in Europe: current status and perspectives. *Renewable & sustainable energy reviews,* 6**,** 405-431.

COE, R. & NEARY, V. 2014. Review of Methods for Modelling Wave Energy Converter Survival in Extreme Sea States. *Proceedings of the 2nd Marine Energy Technology Symposium*.

COIRO, D. P., TROISE, G., CALISE, G. & BIZZARRINI, N. 2016. Wave energy conversion through a point pivoted absorber: Numerical and experimental tests on a scaled model. *Renewable Energy,* 87**,** 317-325.

DAVIDSON, J., WINDT, C., GIORGI, G., GENEST, R. & RINGWOOD, J. V. 2019. Evaluation of Energy Maximising Control Systems for Wave Energy Converters Using OpenFOAM. *OpenFOAM®*. Springer International Publishing.

DAY, A. H., BABARIT, A., FONTAINE, A., HE, Y.-P., KRASKOWSKI, M., MURAI, M., PENESIS, I., SALVATORE, F. & SHIN, H.-K. 2015. Hydrodynamic modelling of marine renewable energy devices: A state of the art review. *Ocean Engineering,* 108**,** 46-69.

DREW, B., PLUMMER, A. R. & SAHINKAYA, M. N. 2009. A review of wave energy converter technology. *Proceedings of the Institution of Mechanical Engineers, Part A: Journal of Power and Energy,* 223**,** 887-902.

DURAND, M., BABARIT, A., PETTINOTTI, B., QUILLARD, O., TOULARASTEL, J. L. & CLÉMENT, A. 2007. *Experimental Validation of the Performances of the SEAREV Wave Energy Converter with Real-Time Latching Control*.

EMEC. *EMEC* [Online]. [Accessed 12-09 2022].

FALCÃO, A. F. & HENRIQUES, J. C. 2016. Oscillating-water-column wave energy converters and air turbines: A review. *Renewable energy,* 85**,** 1391-1424.

FALCÃO, A. F. D. O. 2008. Phase control through load control of oscillating-body wave energy converters with hydraulic PTO system. *Ocean engineering,* 35**,** 358-366.

FALCÃO, A. F. D. O. 2010. Wave energy utilization: A review of the technologies. *Renewable & sustainable energy reviews,* 14**,** 899-918.

FALCÃO, A. F. O., SARMENTO, A. J. N. A., GATO, L. M. C. & BRITO-MELO, A. 2020. The Pico OWC wave power plant: Its lifetime from conception to closure 1986–2018. *Applied Ocean Research,* 98**,** 102104.

FALNES, J. Optimum Control of Oscillation of Wave-Energy Converters. The Eleventh International Offshore and Polar Engineering Conference, 2001. ISOPE-I-01-085.

FALNES, J. & KURNIAWAN, A. 2020. *Ocean waves and oscillating systems: linear interactions including wave-energy extraction,* Cambridge university press.

FENTON, J. D. 1985. A Fifth-Order Stokes Theory for Steady Waves. *Journal of waterway, port, coastal, and ocean engineering,* 111**,** 216-234.

FERZIGER, J. H., PERIĆ, M. & STREET, R. L. 2002. *Computational methods for fluid dynamics,* Springer.

GHAFARI, H. R., GHASSEMI, H. & HE, G. 2021. Numerical study of the Wavestar wave energy converter with multi-point-absorber around DeepCwind semisubmersible floating platform. *Ocean Engineering,* 232**,** 109177.

GIORGI, G. & RINGWOOD, J. V. 2016. Implementation of latching control in a numerical wave tank with regular waves. *Journal of Ocean Engineering and Marine Energy,* 2**,** 211-226.

GUO, B., WANG, R., NING, D., CHEN, L. & SULISZ, W. 2020. Hydrodynamic performance of a novel WEC-breakwater integrated system consisting of triple dual-freedom pontoons. *Energy,* 209**,** 118463.

HANSEN, R., KRAMER, M. & VIDAL, E. 2013. Discrete Displacement Hydraulic Power Take-Off System for the Wavestar Wave Energy Converter. *Energies,* 6**,** 4001-4044.

HENRIQUES, J., GATO, L., FALCAO, A. D. O., ROBLES, E. & FAŸ, F.-X. 2016. Latching control of a floating oscillating-water-column wave energy converter. *Renewable Energy,* 90**,** 229-241.

HIRT, C. W. & NICHOLS, B. D. 1981. Volume of fluid (VOF) method for the dynamics of free boundaries. *Journal of Computational Physics,* 39**,** 201-225.

HOSKIN, R. & NICHOLS, N. K. Optimal Strategies for Phase Control of Wave Energy Devices. 1987.

ITTC 2011. ITTC - Recommended Procedures and Guidelines : Practical Guidelines for Ship CFD Applications.

IVERSEN, L. C. 1982. Numerical method for computing the power absorbed by a phase-controlled point absorber. *Applied Ocean Research,* 4**,** 173-180.

JAKOBSEN, M. M. 2015. *Wave-Structure Interactions on Point Absorbers - an experimental study.* Ph.d.

JAKOBSEN, M. M., BEATTY, S., IGLESIAS, G. & KRAMER, M. M. 2016. Characterization of loads on a hemispherical point absorber wave energy converter. *International Journal of Marine Energy,* 13**,** 1-15.

JIN, S. & GREAVES, D. 2021. Wave energy in the UK: Status review and future perspectives. *Renewable and Sustainable Energy Reviews,* 143**,** 110932.

JUSOH, M. A., IBRAHIM, M. Z., DAUD, M. Z., ALBANI, A. & MOHD YUSOP, Z. 2019. Hydraulic Power Take-Off Concepts for Wave Energy Conversion System: A Review. *Energies,* 12**,** 4510.

KARA, F. 2021. Hydrodynamic performances of wave energy converter arrays in front of a vertical wall. *Ocean Engineering,* 235**,** 109459.

KAVLI, H. P., OGUZ, E. & TEZDOGAN, T. 2017. A comparative study on the design of an environmentally friendly RoPax ferry using CFD. *Ocean Engineering,* 137**,** 22-37.

KIM, D., SONG, S. & TEZDOGAN, T. 2021. Free running CFD simulations to investigate ship manoeuvrability in waves. *Ocean Engineering,* 236**,** 109567.

KIM, D. & TEZDOGAN, T. 2022. CFD-based hydrodynamic analyses of ship course keeping control and turning performance in irregular waves. *Ocean Engineering,* 248**,** 110808.

KIM, J., O'SULLIVAN, J. & READ, A. Ringing Analysis of a Vertical Cylinder by Euler Overlay Method. Volume 4: Offshore Geotechnics; Ronald W. Yeung Honoring Symposium on Offshore and Ship Hydrodynamics, 2012-07-01 2012. American Society of Mechanical Engineers.

KOFOED, J. P., FRIGAARD, P., FRIIS-MADSEN, E. & SØRENSEN, H. C. 2006. Prototype testing of the wave energy converter wave dragon. *Renewable energy,* 31**,** 181-189.

KONISPOLIATIS, D. N. & MAVRAKOS, S. A. 2020. Wave Power Absorption by Arrays of Wave Energy Converters in Front of a Vertical Breakwater: A Theoretical Study. *Energies,* 13**,** 1985.

KONISPOLIATIS, D. N. & MAVRAKOS, S. A. 2021. Hydrodynamic Efficiency of a Wave Energy Converter in Front of an Orthogonal Breakwater. *Journal of Marine Science and Engineering,* 9**,** 94.

KORDE, U. A. Control system applications in wave energy conversion. OCEANS 2000 MTS/IEEE Conference and Exhibition. Conference Proceedings (Cat. No. 00CH37158), 2000. IEEE, 1817-1824.

KRAMER, M., MARQUIS, L. & FRIGAARD, P. Performance evaluation of the wavestar prototype. 9th ewtec 2011: Proceedings of the 9th European Wave and Tidal Conference, Southampton, UK, 5th-9th September 2011, 2011. University of Southampton.

KRISHNENDU, P. & RAMAKRISHNAN, B. 2020. Performance analysis of dual sphere wave energy converter integrated with a chambered breakwater system. *Applied Ocean Research,* 101**,** 102279.

KRISHNENDU, P. & RAMAKRISHNAN, B. 2021. Integration of a heaving-type wave energy converter with a chambered breakwater system. *Marine Systems & Ocean Technology,* 16**,** 1-13.

LE MÉHAUTÉ, B. 2013. *An introduction to hydrodynamics and water waves*, Springer Science & Business Media.

MAVRAKOS, S. A., KATSAOUNIS, G. M., NIELSEN, K. & LEMONIS, G. Numerical performance investigation of an array of heaving wave power converters in front of a vertical breakwater. Proceedings of the International Offshore and Polar Engineering Conference, 2004. 238-245.

MCIVER, P. & EVANS, D. V. 1988. An approximate theory for the performance of a number of wave-energy devices set into a reflecting wall. *Applied Ocean Research,* 10**,** 58-65.

MUSTAPA, M. A., YAAKOB, O. B., AHMED, Y. M., RHEEM, C.-K., KOH, K. K. & ADNAN, F. A. 2017. Wave energy device and breakwater integration: A review. *Renewable and Sustainable Energy Reviews,* 77**,** 43-58.

NING, D.-Z., ZHAO, X.-L., ZHAO, M., HANN, M. & KANG, H.-G. 2017. Analytical investigation of hydrodynamic performance of a dual pontoon WEC-type breakwater. *Applied Ocean Research,* 65**,** 102-111.

NING, D., ZHAO, X., CHEN, L. & ZHAO, M. 2018. Hydrodynamic Performance of an Array of Wave Energy Converters Integrated with a Pontoon-Type Breakwater. *Energies,* 11**,** 685.

NING, D., ZHAO, X., GÖTEMAN, M. & KANG, H. 2016. Hydrodynamic performance of a pile-restrained WEC-type floating breakwater: An experimental study. *Renewable Energy,* 95**,** 531-541.

PAPARELLA, F., MONK, K., WINANDS, V., LOPES, M. F. P., CONLEY, D. & V. RINGWOOD, J. 2015. Up-Wave and Autoregressive Methods for Short-Term Wave Forecasting for an Oscillating Water Column. *IEEE Transactions on Sustainable Energy,* 6**,** 171-178.

PECHER, A. 2012. *Performance Evaluation of Wave Energy Converters.* Aalborg University.

PECHER, A. & KOFOED, J. P. 2017. *Handbook of ocean wave energy / [internet resource]*, Cham, Switzerland : Springer Open.

PENALBA, M., DAVIDSON, J., WINDT, C. & RINGWOOD, J. V. 2018. A high-fidelity wave-to-wire simulation platform for wave energy converters: Coupled numerical wave tank and power take-off models. *Applied Energy,* 226**,** 655-669.

PENALBA, M., GIORGI, G. & RINGWOOD, J. V. 2017. Mathematical modelling of wave energy converters: A review of nonlinear approaches. *Renewable and Sustainable Energy Reviews,* 78**,** 1188-1207.

PENALBA, M. & RINGWOOD, J. V. The Impact of a High-Fidelity Wave-to-Wire Model in Control Parameter Optimisation and Power Production Assessment. ASME 2018 37th International Conference on Ocean, Offshore and Arctic Engineering, 2018. V010T09A039.

PERIC, R. 2019. *Minimizing undesired wave reflection at the domain boundaries in flow simulations with forcing zones.* Technischen Universität Hamburg.

PERIĆ, R. & ABDEL-MAKSOUD, M. 2016. Reliable damping of free-surface waves in numerical simulations. *Ship Technology Research,* 63**,** 1-13.

PERIĆ, R., VUKČEVIĆ, V., ABDEL-MAKSOUD, M. & JASAK, H. 2022. Optimizing wave generation and wave damping in 3D-flow simulations with implicit relaxation zones. *Coastal Engineering,* 171**,** 104035.

PRADO, M. & POLINDER, H. 2013. Case study of the Archimedes Wave Swing (AWS) direct drive wave energy pilot plant.

RANSLEY, E. J., GREAVES, D. M., RABY, A., SIMMONDS, D., JAKOBSEN, M. M. & KRAMER, M. 2017. RANS-VOF modelling of the Wavestar point absorber. *Renewable Energy,* 109**,** 49-65.

REABROY, R., ZHENG, X., ZHANG, L., ZANG, J., YUAN, Z., LIU, M., SUN, K. & TIAPLE, Y. 2019. Hydrodynamic response and power efficiency analysis of heaving wave energy converter integrated with breakwater. *Energy Conversion and Management,* 195**,** 1174-1186.

RICHARDSON, L. F. 1911. IX. The approximate arithmetical solution by finite differences of physical problems involving differential equations, with an application to the stresses in a masonry dam. *Philosophical Transactions of the Royal Society of London. Series A, Containing Papers of a Mathematical or Physical Character,* 210**,** 307-357.

RINGWOOD, J. & BUTLER, S. 2004. Optimisation of a wave energy converter. *IFAC Proceedings Volumes,* 37**,** 155-160.

RODI, W. 1991. Experience with two-layer models combining the k-epsilon model with a one-equation model near the wall. *29th Aerospace Sciences Meeting.* American Institute of Aeronautics and Astronautics.

RUELLAN, M., BENAHMED, H., MULTON, B., JOSSET, C., BABARIT, A. & CLEMENT, A. 2010. Design Methodology for a SEAREV Wave Energy Converter. *TEC,* 25**,** 760-767.

SALTER, S. H., TAYLOR, J. R. M. & CALDWELL, N. J. 2002. Power conversion mechanisms for wave energy. *Proceedings of the Institution of Mechanical Engineers, Part M: Journal of Engineering for the Maritime Environment,* 216**,** 1-27.

SCHAY, J., BHATTACHARJEE, J. & GUEDES SOARES, C. Numerical Modelling of a Heaving Point Absorber in Front of a Vertical Wall. Volume 8: Ocean Renewable Energy, 2013-06-09 2013. American Society of Mechanical Engineers.

SHENG, W. 2020. Wave Energy Converters. *In:* CUI, W., FU, S. & HU, Z. (eds.) *Encyclopedia of Ocean Engineering.* Singapore: Springer Singapore.

SIEMENS 2020. Simcenter STAR-CCM+ Documentation.

TAY, Z. Y. 2022a. Effect of resonance and wave reflection in semi-enclosed moonpool on performance enhancement of point absorber arrays. *Ocean Engineering,* 243**,** 110182.

TAY, Z. Y. 2022b. Energy generation enhancement of arrays of point absorber wave energy converters via Moonpool's resonance effect. *Renewable Energy,* 188**,** 830-848.

TEILLANT, B., GILLOTEAUX, J. C. & RINGWOOD, J. V. 2010. Optimal Damping Profile for a Heaving Buoy Wave Energy Converter. *IFAC Proceedings Volumes,* 43**,** 360-365.

TERRERO GONZÁLEZ, A., DUNNING, P., HOWARD, I., MCKEE, K. & WIERCIGROCH, M. 2021. Is wave energy untapped potential? *International Journal of Mechanical Sciences,* 205**,** 106544.

TERZIEV, M., TEZDOGAN, T. & INCECIK, A. 2019. A geosim analysis of ship resistance decomposition and scale effects with the aid of CFD. *Applied Ocean Research,* 92**,** 101930.

TERZIEV, M., TEZDOGAN, T. & INCECIK, A. 2020. Application of eddy-viscosity turbulence models to problems in ship hydrodynamics. *Ships and Offshore Structures,* 15**,** 511-534.

TEZDOGAN, T., INCECIK, A. & TURAN, O. 2016. Full-scale unsteady RANS simulations of vertical ship motions in shallow water. *Ocean Engineering,* 123**,** 131-145.

TOM, N., RUEHL, K. & FERRI, F. Numerical Model Development and Validation for the WECCCOMP Control Competition. Volume 10: Ocean Renewable Energy, 2018-06-17 2018. American Society of Mechanical Engineers.

TOM, N. M., MADHI, F. & YEUNG, R. W. 2019. Power-to-load balancing for heaving asymmetric wave-energy converters with nonideal power take-off. *Renewable Energy,* 131**,** 1208-1225.

WANG, Y., WANG, D. & DONG, S. 2022. Theoretical study on arranging heaving wave energy converters in front of jarlan-type breakwater. *Ocean Engineering,* 248**,** 110850.

WEC-SIM. *WEC-Sim (Wave Energy Converter SIMulator) documentation* [Online]. Available: https://wec-sim.github.io/WEC-Sim/dev/index.html [Accessed 05 March 2024].

WINDT, C., DAVIDSON, J., RANSLEY, E. J., GREAVES, D., JAKOBSEN, M., KRAMER, M. & RINGWOOD, J. V. 2020a. Validation of a CFD-based numerical wave tank model for the power production assessment of the wavestar ocean wave energy converter. *Renewable Energy,* 146**,** 2499-2516.

WINDT, C., DAVIDSON, J. & RINGWOOD, J. V. 2018. High-fidelity numerical modelling of ocean wave energy systems: A review of computational fluid dynamics-based numerical wave tanks. *Renewable and Sustainable Energy Reviews,* 93**,** 610-630.

WINDT, C., FAEDO, N., GARCÍA-VIOLINI, D., PEÑA-SANCHEZ, Y., DAVIDSON, J., FERRI, F. & RINGWOOD, J. V. 2020b. Validation of a CFD-Based Numerical Wave Tank Model of the 1/20th Scale Wavestar Wave Energy Converter. *Fluids,* 5**,** 112.

YEMM, R., PIZER, D., RETZLER, C. & HENDERSON, R. 2012. Pelamis: experience from concept to connection. *Proc. R. Soc. A,* 370**,** 365-380.

ZHANG, H., DING, X., ZHOU, B., ZHANG, L. & YUAN, Z. 2019. Hydrodynamic Performance Study of Wave Energy–Type Floating Breakwaters. *Journal of Marine Science and Application,* 18**,** 64-71.

ZHAO, X., ZHANG, Y., LI, M. & JOHANNING, L. 2020. Hydrodynamic performance of a Comb-Type Breakwater-WEC system: An analytical study. *Renewable Energy,* 159**,** 33-49.

ZHAO, X., ZHANG, Y., LI, M. & JOHANNING, L. 2021. Experimental and analytical investigation on hydrodynamic performance of the comb-type breakwater-wave energy converter system with a flange. *Renewable Energy,* 172**,** 392-407.

ZHAO, X. L., NING, D. Z. & LIANG, D. F. 2019a. Experimental investigation on hydrodynamic performance of a breakwater-integrated WEC system. *Ocean Engineering,* 171**,** 25-32.

ZHAO, X. L., NING, D. Z., ZOU, Q. P., QIAO, D. S. & CAI, S. Q. 2019b. Hybrid floating breakwater-WEC system: A review. *Ocean Engineering,* 186**,** 106126.

ZURKINDEN, A. S., FERRI, F., BEATTY, S., KOFOED, J. P. & KRAMER, M. M. 2014. Non-linear numerical modeling and experimental testing of a point absorber wave energy converter. *Ocean Engineering,* 78**,** 11-21.